NLO QCD and Two Weak Bosons at the LHC

Tom Melia

New College

University of Oxford

A thesis submitted for the degree of

Doctor of Philosophy

Trinity 2012

Abstract

We present original calculations of standard model processes involving two weak bosons at NLO in QCD, and study related phenomenology with reference to Higgs boson and new physics searches at the LHC. We employ a new theoretical technique, D-dimensional generalised unitarity, to obtain the multi-particle, one-loop scattering amplitudes for the processes $pp \to W^+W^- + 1j$, $pp \to W^+W^- + 2j$, $pp \to W^+W^+ + 2j$, and $gg \to W^+W^-g$. We consider the LHC phenomenology of: the W^+W^-+n jets background to Higgs searches, for $n = 0, 1, 2$; the effects of anomalous tri-linear gauge couplings in WW and WZ production; the background $W^+W^+ + 2j$ to new physics searches involving like-sign leptons; and a method of spin determination of new states in a scenario where conventional methods fail.

Acknowledgements

I am extremely fortunate to have had the guidance from my supervisor Giulia Zanderighi, and I thank her for patiently helping me to understand and work on projects relevant to the LHC over a very exciting four years for this experiment.

I owe thanks to my collaborators Kirill Melnikov, Paolo Nason, Markus Schulze and Raoul Rontsch for the many explanations and discussions we have had on the topics in this thesis. I also thank the members of the physics and mathematics departments at Oxford, who make it such an enjoyable place to study and are too many to mention, but in particular Frank Close, Graham Ross, Alan Barr, John March-Russell, Mat Bullimore, and Richard Davison, who have helped to shape the course and contributed a lot to the enjoyment of my DPhil.

This research was supported by a UK Science and Technology Facilities Council (STFC) studentship.

Contents

Chapter 1

Introduction

In the weeks before the submission of this thesis, the ATLAS and CMS detector collaborations at the CERN Large Hadron Collider (LHC) announced the discovery of a new 125-126 GeV resonance [1, 2] which is, at the time of writing, consistent with being the Higgs boson of the standard model. This discovery is a perfect example of what is required for performing physics at the LHC – an incredibly detailed understanding of the collider and detectors, but also an ability to make reliable theoretical predictions for what we expect to observe, based on our current understanding of particle physics. The main subject of this thesis concerns the application of a new technique – D-dimensional generalised unitarity [3] – to obtain accurate theoretical descriptions of standard model processes involving two weak bosons at next-to-leading order (NLO) in quantum chromodynamic (QCD) perturbation theory. The original phenomenological predictions for LHC physics made in this thesis are presented by splitting them roughly into two flagship areas of the LHC programme: Higgs boson physics, and searches for physics beyond the standard model (BSM).

Weak boson pair production is a very interesting process to study at the LHC. If the 125-126 GeV resonance is to be identified with the Higgs boson responsible for electroweak symmetry breaking in the standard model, measurements of its couplings to pairs of weak bosons $H \to \gamma\gamma$, WW, ZZ and $Z\gamma$ must conform with the definite predictions made by this theory. The non-resonant backgrounds to these decay modes must be well understood to be able to make these observations. What is more, when electroweak bosons are pair produced, the non-abelian nature of the weak force predicts a coupling for three gauge boson vertex which is fixed in the standard model by the gauge symmetry. The high centre of mass energy and large luminosity at the LHC mean many more pairs of weak bosons will be produced than in any previous experiment, and very precise measurements of this coupling will be possible. Deviations from the standard model value would indicate the presence of new physics. Weak boson pair production is also a background to many BSM signatures at the LHC.

A huge challenge at the LHC is to understand both experimentally and theoretically the proliferation of QCD interactions which take place. The non-abelian nature of QCD makes theoretical calculations difficult, but at the LHC the asymptotic freedom of the theory and factorisation of long- and short-distance physics means that predictions can be made using perturbation theory. However, predictions which only take into account leading order terms in the perturbation series often suffer from large theoretical uncertainties associated with the large dependence of the result on the scale at which the running coupling constant is evaluated, and on the scale at which the factorisation between long- and short-distance physics takes place. A more theoretically reliable prediction is obtained in going to NLO in QCD. Successful analyses at the Tevatron experiment have highlighted the importance of taking into account these corrections, particularly when data driven techniques are not easily applied, such as background normalisation away from resonant regions of interest (see e.g. [4]).

The layout of this thesis is in two parts: Part I, which contains Chapters 2 and 3, presents the technical aspects of the NLO QCD calculations in this thesis; Part II, which contains Chapters 4 and 5, focuses on LHC phenomenology.

Chapter 2 is a summary of D-dimensional generalised unitarity, which is a new technique proposed in Ref. [3] for obtaining one-loop scattering amplitudes. The use of traditional Feynman diagram based methods to evaluate one-loop QCD scattering amplitudes with N external particles becomes intractable as N gets large because the number of Feynman diagrams grows factorially with N, and the complexity of individual one-loop Feynman diagram contributions also increases sharply. At the LHC, however, large multiplicity QCD processes are accessible and are important for the physics programme, and this has led to a corresponding theoretical drive over recent years to develop new techniques for overcoming these problems. Prior to 2009, no $2 \to 4$ hadronic process[1] (i.e. $N = 6$) was known to NLO in QCD. In this thesis, two of the calculations we present, $pp \to W^+W^- + 2j$ and $pp \to W^+W^+ + 2j$, were among the first $2 \to 4$ process calculations to appear at NLO in QCD, proving the power of the technique of D-dimensional generalised unitarity.

Chapter 3 presents the general set-up of an NLO QCD calculation. This provides a prescription of how to convert LO and NLO matrix elements, calculated perturbatively using the QCD Lagrangian, into a prediction for collisions between protons, in which the quarks and gluons have a non-perturbative description. We give an overview of the Catani-Seymour dipole formalism [5] employed in this thesis for dealing with the cancellation of infrared (IR) divergences between the one-loop and the real emission NLO contributions in a numerical implementation. The original work of the calculation of the process $pp \to W^+W^- + 1j$ using the D-dimensional generalised unitarity technique is used as an example in this Chapter, as it displays features which are common to all of the other processes considered in this thesis.

Chapter 4 focuses on phenomenology surrounding Higgs boson physics at the LHC for the decay mode $H \to W^+W^-$. The layout of this Chapter reflects the way in which the experimental detector collaborations divide the search for the Higgs boson into bins of different jet multiplicity. We first consider backgrounds to Higgs boson

[1]That is in which all of the external particles can attach to the loop.

searches in the zero-jet ($0j$) and one-jet ($1j$) bins, and investigate contributions which are formally of next-to-next-to-leading order (NNLO) in QCD which occur through the mechanism of gluon-gluon fusion at one-loop: $gg \to W^+W^-$ and $gg \to W^+W^-g$. Despite being of a higher order in the perturbation series, the $0j$ gg contribution to the cross section when Higgs search cuts are applied was found in Refs. [6, 7] to be larger than the NLO corrections – of order 30% of the total cross section – as a result of the large gluon flux at the LHC. We detail an original calculation of the gg contribution to the $1j$ bin and present results for the LHC, as well as revisiting the $0j$ bin results with up-to-date experimental cuts that are being employed by ATLAS and CMS in Higgs boson searches. Turning next to the two-jet ($2j$) bin for Higgs searches, we present the phenomenology of the NLO calculation of $pp \to W^+W^- + 2j$, which is the dominant background to Higgs production in association with two jets. Two jets are observed in the detector when the Higgs is produced via weak boson fusion, and so the $2j$ bin is particularly interesting for studies of this production mechanism.

Chapter 5 presents phenomenological results which are relevant to searches for BSM physics. We consider first an indirect search for new physics, which involves precise measurements of the coupling constant of the three weak boson vertex – this is fixed in the standard model by gauge symmetry. We demonstrate a new implementation of W^+W^- and WZ production in the `POWHEG BOX` with a study of anomalous tri-linear weak gauge boson couplings at the LHC. The remainder of the Chapter focuses on direct searches for BSM physics. We present the phenomenology of $pp \to W^+W^+ + 2j$ at the LHC, which is a standard model background to BSM processes leading to a striking detector signature of like-sign leptons, jets, and missing energy. Finally, we consider a more general aspect of BSM phenomenology which is concerned with determining the nature of any new particles which are directly produced at the LHC. Many scenarios call for novel techniques to pin down masses and spins of new states in order to shed light on as to which theory describes them.

We will present a method of spin determination in a BSM scenario where conventional methods can not be used.

Chapter 6 concludes this thesis. We find that the method of D-dimensional generalised unitarity can be developed and employed to provide an improved theoretical description – the first at NLO in QCD – of the processes $pp \to W^+W^- + 2j$ and $pp \to W^+W^+ + 2j$. The first calculation of a gluon-induced contribution to a background for Higgs boson searches, $gg \to W^+W^-g$, is also performed using this method. The contribution is found to be sizable at the LHC but slightly smaller than the $0j$ gluon induced contribution, $gg \to W^+W^-$, and we conclude that both are highly sensitive to the experimental cuts used. We find two new variables with mass independent properties and which have the potential to be used for spin determination of new particles produced at the LHC in a scenario where conventional methods fail.

This thesis is based on the research first published in Refs. [8, 9, 10, 11, 12], most of which are co-authored papers.

Chapter 2

Generalised D-dimensional Unitarity and NLO QCD Calculations

Chapter Overview

At the 2005 Les Houches conference, an experimenter's wishlist was drawn up, which consisted of experimentally important processes at the LHC for which it would be highly desirable to have a theoretical description of at NLO [13]. At the time, it was unclear whether the existing Feynman diagrams based methods were adequate for calculating the higher multiplicity processes which were prioritised – all were $2 \to 3$ and $2 \to 4$ hadronic QCD processes, which involve the evaluation of a large number of complicated Feynman diagrams, in particular one-loop diagrams with tensor integrals of a relatively high rank.

The urgency for new methods suitable to handle NLO QCD calculations with many external particles which are needed for the LHC physics programme has led to an extraordinary amount of progress in this field in the past few years. In this Chapter we outline a new technique, D-dimensional generalised unitarity, which was proposed in Ref. [3] and is based on ideas of generalised unitarity presented by Britto-Cachazo-Feng (BCF) in Ref. [14] and the results of a paper by Ossola-Pittau-Papadopoulos (OPP) [15] which detailed a new way to reduce a tensor integral to scalar integrals. It marks a development of on-shell technology in the calculation of scattering amplitudes to the point at which it can be applied to a completely general standard model process involving many particles. The technique of D-dimensional generalised unitarity will be used in this thesis to calculate complicated one-loop amplitudes involving high-multiplicity final states, specifically those which contribute to the processes $pp \to W^+W^- + 2j$, $pp \to W^+W^+ + 2j$, and $gg \to W^+W^-g$. These three processes were all on the 2005 Les Houches list[1].

Before presenting a summary of this technique, it is worth highlighting that almost all of the processes on the 2005 Les Houches wishlist, along with processes added in 2007 [18] and 2009 [19], have at the time of writing this thesis been calculated at NLO in QCD [20]. This is testament to just how remarkable the developments in NLO technology have been over recent years. In particular, refinements of Feynman diagram based methods along with other new techniques based on unitarity, OPP reduction, and on-shell methods have brought the field to the point where automation of NLO QCD corrections looks to be within reach [21, 22, 23, 24].

This Chapter is laid out in two parts. Firstly, Sec. 2.1 describes the OPP reduction procedure of Ref. [15] to reduce tensor integrals to a basis of scalar integrals, with the extension proposed in Ref. [3] which uses a D-dimensional parameterisation of the integrand so as to enable the rational part of the tensor integral to be determined. Secondly, Sec. 2.2 summaries the considerations of Ref. [3] which enable the reduction procedure to be applied numerically to completely general full one-loop amplitudes in the standard model. We summarise the content of this Chapter in Sec. 2.3.

[1]More accurately, the third process is an NNLO contribution to the process $pp \to W^+W^- + 1j$ which was wanted at NLO in the 2005 wishlist, and was first calculated to NLO accuracy in [16, 17].

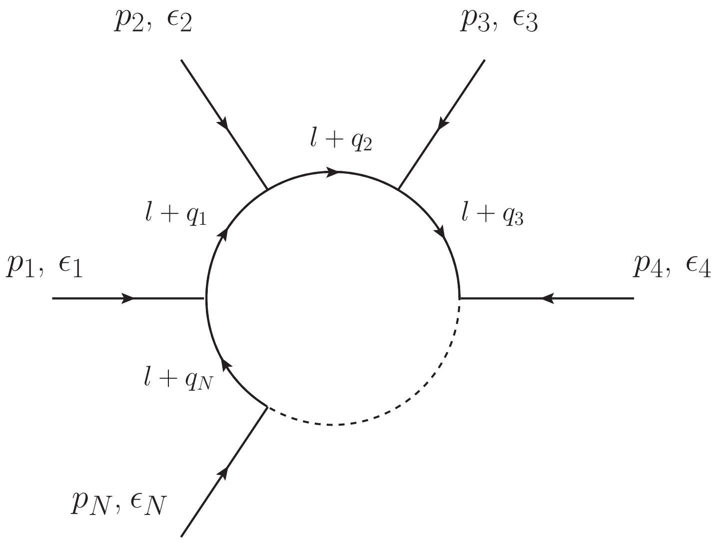

Figure 2.1: A generic N-point tensor integral.

2.1 Generalised D-dimensional Unitarity Part I: Tensor Integrals to Basis Integrals

2.1.1 OPP Reduction

$$I_N^D = \int \frac{\mathrm{d}^D l}{i\pi^{D/2}} \frac{\mathrm{Num}(l)}{d_1\, d_2 \dots d_N} \tag{2.1}$$

The above expression defines an N-point tensor integral in D dimensions. This can be thought of as arising from the contribution of an N-particle, one-loop Feynman diagram, schematically drawn in Fig. 2.1. Here, l is the loop momentum, and $\mathrm{Num}(l)$ is a numerator which is in general a function of l and the momentum and polarisation vectors of external particles, p_i and ϵ_i, where i runs from 1 to N. The factors d_i in the denominator are inverse scalar propagators, $d_i = d_i(l) = (l+q_i)^2 - m_i^2$, where $q_i = (\sum_{j=1}^{i} p_i) - q_0$, with q_0 an arbitrary four-vector representing the choice of loop momentum, and m_i is the mass of the internal particle i. For the case when $\mathrm{Num}(l) = 1$, Eq. (2.1) defines an N-point scalar integral. We will denote a D-dimensional,

n-point scalar integral with the product of inverse propagators $d_{i_1} d_{i_2} \dots d_{i_n}$ in the denominator by $\mathcal{I}^D_{n;\, i_1 i_2 \dots i_n}$.

When the rank r of the tensor integral in Eq. (2.1) is less than or equal to N – and this is always the case for tensor integrals appearing in standard model one-loop calculations – then the numerator can always be brought to the form [15]

$$
\begin{aligned}
\mathrm{Num}(l) = \Bigg\{ & \sum_{[i_1|i_5]} \bar{e}_{i_1 i_2 i_3 i_4 i_5}(l) \prod_{i \neq i_1 i_2 i_3 i_4 i_5} d_i \\
& + \sum_{[i_1|i_4]} \bar{d}_{i_1 i_2 i_3 i_4}(l) \prod_{i \neq i_1 i_2 i_3 i_4} d_i \\
& + \sum_{[i_1|i_3]} \bar{c}_{i_1 i_2 i_3}(l) \prod_{i \neq i_1 i_2 i_3} d_i \\
& + \sum_{[i_1|i_2]} \bar{b}_{i_1 i_2}(l) \prod_{i \neq i_1 i_2} d_i \\
& + \sum_{[i_1|i_1]} \bar{a}_{i_1}(l) \prod_{i \neq i_1} d_i \Bigg\} ,
\end{aligned} \tag{2.2}
$$

with $[i_1|i_n] = 1 \leq i_1 < i_2 < \dots < i_n \leq N$, and where the coefficients $\bar{e}_{i_1 i_2 i_3 i_4 i_5}(l)$, $\bar{d}_{i_1 i_2 i_3 i_4}(l)$, etc. are functions of p_i and ϵ_i as well as l. We shall explicitly give the form of the l dependence below, but for now in order to demonstrate the origin of Eq. (2.2), we decompose the coefficients into a part dependent on l and a part independent of l, for example[2]: $\bar{d}_{i_1 i_2 i_3 i_4}(l) = d_{i_1 i_2 i_3 i_4} + \tilde{d}_{i_1 i_2 i_3 i_4}(l)$. The remarkable thing is that a parameterisation can be chosen so that the integration over the loop momentum in

[2]We use a $\bar{d}$ coefficient as an example here because as we will see, the $\bar{e}$ coefficients can be chosen to be independent of l.

Eq. (2.1) is trivial, e.g.:

$$\begin{aligned}
\int \frac{\mathrm{d}^D l}{i\pi^{D/2}} \frac{\bar{d}_{i_1 i_2 i_3 i_4}(l)}{d_{i_1} d_{i_2} d_{i_3} d_{i_4}} &= \int \frac{\mathrm{d}^D l}{i\pi^{D/2}} \frac{d_{i_1 i_2 i_3 i_4} + \tilde{d}_{i_1 i_2 i_3 i_4}(l)}{d_{i_1} d_{i_2} d_{i_3} d_{i_4}} \\
&= d_{i_1 i_2 i_3 i_4} \int \frac{\mathrm{d}^D l}{i\pi^{D/2}} \frac{1}{d_{i_1} d_{i_2} d_{i_3} d_{i_4}} + \mathrm{Rational}_{D\to 4} \\
&= d_{i_1 i_2 i_3 i_4}\, \mathcal{I}^D_{4;\, i_1 i_2 i_3 i_4} + \mathrm{Rational}_{D\to 4} \,,
\end{aligned} \tag{2.3}$$

where almost all of the terms with l dependence have integrated to zero, leaving behind the l independent term multiplying a 4-point scalar integral. The only l dependent terms which do not integrate to zero are those which only depend on the $D-4$ extra-dimensional part of l, denoted $\mathrm{Rational}_{D\to 4}$ in Eq. (2.3). As we will see below, these integrals are simple to perform in the limit $D \to 4$ – they give rise to rational functions of p_i and/or ϵ_i (i.e. these functions do not have branch cuts, unlike the logarithms and dilogarithms which are obtained from integrating scalar integrals like $\mathcal{I}_{4;\, i_1 i_2 i_3 i_4}$ above).

This gives an explanation of Eq. (2.2) – it is is the statement that any tensor integral can be expressed in terms of a basis of scalar integrals. For $D = 4 - 2\epsilon$, in general

$$I_N^{4-2\epsilon} = d_j\, \mathcal{I}^{4-2\epsilon}_{4;\, j} + c_j\, \mathcal{I}^{4-2\epsilon}_{3;\, j} + b_j\, \mathcal{I}^{4-2\epsilon}_{2;\, j} + a_j\, \mathcal{I}^{4-2\epsilon}_{1;\, j} + \mathcal{R} + \mathcal{O}(\epsilon) \,, \tag{2.4}$$

where the index j represents the sum over all possible subscript indices as in Eq. (2.2). Here $\mathcal{R}$ is known as the rational part of the tensor integral. The reduction of a general tensor integral to this basis follows from using Lorentz invariance to express it in terms of form factors and, because space-time is four dimensional, re-expressing 5- or higher-point scalar integrals as linear combinations of four point scalar integrals, up to terms of order ϵ. Traditional reduction techniques, such as Passarino-Veltman reduction, follow exactly this method in order to obtain the coefficients d_j, c_j, *etc.* [25]. Eq. (2.2) above is valid in full $D > 4$ dimensions and this requires the five-point scalar integrals to be in the basis (6-point and higher scalar integrals in $D > 4$ dimensions can be expressed in terms of 5-point scalar integrals – this is because the extra-dimensional part of l only enters calculations as l^2_{D-4}, and so is direction independent in the $D-4$ extra-dimensional space).

Ref. [15] outlined a different method to obtain the coefficients of the scalar integrals, which involves reducing the integrand of a tensor integral. It makes use of the van Neerven - Vermaseren basis which, as it is defined in many of the references and reviews on this subjects, we shall not reproduce here (see for example Ref. [26]). This basis has a *physical space* and a *transverse space* which can be worked out for each of the R-point integrals resulting from the substitution of Eq. (2.2) into Eq. (2.1). Each of these integrals has R momenta $k_1 \dots k_R$ flowing into the loop, which are either equal to or are linear combinations of the external momenta p_i. The vector space spanned by these inflow momenta is the physical space, which has dimension $D_P = \min(D, R-1)$, accounting for momentum conservation. The (non-orthogonal) van Neerven - Vermaseren basis in this physical space is dual to the (non-orthogonal) basis $\{k_1 \dots k_{D_P}\}$, and is spanned by vectors denoted $v_1 \dots v_{D_P}$, with the property $v_i \cdot k_j = \delta_{ij}$ for $j \leq D_P$. The transverse space has dimensionality $D_T = D - D_P$ and the van Neerven - Vermaseren basis in this space is spanned by vectors $n_{D_P+1} \dots n_4$ (in the case of $D_P = 4$ for the integrals involving the $\bar{e}$ coefficients, there is no transverse space) which satisfy the properties $n_i \cdot n_j = \delta_{ij}$, $n_i \cdot v_j = 0$ and $n_i \cdot k_j = 0$. The projection of l onto a direction n_i in the transverse space is given by $(l \cdot n_i)$. In $D > 4$ dimensions, l also has a projection onto the $D-4$ dimensional space, which we denote $(l \cdot n_\epsilon)$ in what follows[3].

OPP reduction demonstrates that the explicit dependence on l for the coefficients $\bar{e}, \bar{d}, \dots, \bar{a}$ in Eq. (2.2) can be parameterised as (suppressing the subscript indices)

[3]In the original OPP paper, the reduction proceeds in four dimensions. The inclusion of the projection of l into the $D-4$ dimensional space was presented in Ref. [3].

[3, 15]:

5-point coefficients

$$\bar{e}(l) = e^{(0)} \,, \tag{2.5}$$

4-point coefficients

$$\bar{d}(l) = d^{(0)} + d^{(1)}(l \cdot n_4) + d^{(2)}(l \cdot n_\epsilon)^2 + d^{(3)}(l \cdot n_\epsilon)^2(l \cdot n_4) + d^{(4)}(l \cdot n_\epsilon)^4 \,, \tag{2.6}$$

3-point coefficients

$$\begin{aligned} \bar{c}(l) = c^{(0)} &+ c^{(1)}(l \cdot n_3) + c^{(2)}(l \cdot n_4) + c^{(3)}(\,(l \cdot n_3)^2 - (l \cdot n_4)^2\,) \\ &+ c^{(4)}(l \cdot n_3)(l \cdot n_4) + c^{(5)}(l \cdot n_3)^3 + c^{(6)}(l \cdot n_4)^3 \\ &+ c^{(7)}(l \cdot n_\epsilon)^2 + c^{(8)}(l \cdot n_\epsilon)^2(l \cdot n_3) + c^{(9)}(l \cdot n_\epsilon)^2(l \cdot n_4) \,, \end{aligned} \tag{2.7}$$

2-point coefficients

$$\begin{aligned} \bar{b}(l) = b^{(0)} &+ b^{(1)}(l \cdot n_2) + b^{(2)}(l \cdot n_3) + b^{(3)}(l \cdot n_4) + b^{(4)}(\,(l \cdot n_2)^2 - (l \cdot n_4)^2\,) \\ &+ b^{(5)}(\,(l \cdot n_3)^2 - (l \cdot n_4)^2\,) + b^{(6)}(l \cdot n_2)(l \cdot n_3) \\ &+ b^{(7)}(l \cdot n_3)(l \cdot n_4) + b^{(8)}(l \cdot n_2)(l \cdot n_4) + b^{(9)}(l \cdot n_\epsilon)^2 \,, \end{aligned} \tag{2.8}$$

and 1-point coefficients

$$\bar{a}(l) \;=\; a^{(0)} + a^{(1)}(l \cdot n_1) + a^{(2)}(l \cdot n_2) + a^{(3)}(l \cdot n_3) + a^{(4)}(l \cdot n_4) \,. \tag{2.9}$$

The l dependence of the coefficients is entirely on l's projection onto the transverse space and the ϵ-dimension space. The important thing is that *all* of the terms with a projection of l onto the transverse space vanish under integration of the loop momentum, which is what makes performing the integral trivial, as in Eq. (2.3)[4]. The terms which only involve l's projection on the ϵ-dimensional space do not vanish and can be written in terms of scalar integrals in higher dimensions

$$\begin{aligned}\int \frac{\mathrm{d}^D l}{i\pi^{D/2}} \frac{(l\cdot n_\epsilon)^2}{d_{i_1}d_{i_2}d_{i_3}d_{i_4}} &= -\frac{(D-4)}{2}\mathcal{I}^{D+2}_{4;\,i_1i_2i_3i_4},\\ \int \frac{\mathrm{d}^D l}{i\pi^{D/2}} \frac{(l\cdot n_\epsilon)^4}{d_{i_1}d_{i_2}d_{i_3}d_{i_4}} &= \frac{(D-2)(D-4)}{4}\mathcal{I}^{D+4}_{4;\,i_1i_2i_3i_4},\\ \int \frac{\mathrm{d}^D l}{i\pi^{D/2}} \frac{(l\cdot n_\epsilon)^2}{d_{i_1}d_{i_2}d_{i_3}} &= -\frac{(D-4)}{2}\mathcal{I}^{D+2}_{3;\,i_1i_2i_3},\\ \int \frac{\mathrm{d}^D l}{i\pi^{D/2}} \frac{(l\cdot n_\epsilon)^2}{d_{i_1}d_{i_2}} &= -\frac{(D-4)}{2}\mathcal{I}^{D+2}_{2;\,i_1i_2}.\end{aligned} \tag{2.10}$$

These integrals are the origin of the Rational$_{D\to 4}$ term in Eq. (2.3), and of $\mathcal{R}$ in Eq. (2.4) – when $D = 4 - 2\epsilon$, the factors $(D-4)$ in Eq. (2.10) hit ultraviolet (UV) divergences in the integrals, which contribute at order ϵ^{-1}, and so a finite part remains in the limit $\epsilon \to 0$. The rational part of the amplitude is a remnant of UV regularisation – as we have seen, they are only picked up from the ϵ-dimensional part of l only. This is a key feature of D-dimensional generalised unitarity: allowing for the parameterisation of the coefficients in Eqs. (2.5)-(2.9) to include projections of l onto the extra dimensional space. Methods based on techniques related to the one described in this Chapter, but which proceed only in four dimensions, have to obtain the rational part via a different means.

To summarise the results of this section: any one-loop, N-point tensor integral (defined in Eq. (2.1)) with rank $r \le N$ can be fully reduced to a basis of scalar

[4]This can be seen using Lorentz invariance, since all tensor integrals are proportional to tensors involving the metric tensor $g^{\mu\nu}$ and inflow momenta k_i^μ. Then, because $n_i \cdot n_j = 0$ and $n_i \cdot k_j = 0$, it follows that all of the terms in Eqs. (2.5)-(2.9) involving the transverse projection vanish trivially under integration.

integrals

$$
\begin{aligned}
I_N^D &= \sum_{[i_1|i_5]} e^{(0)}_{i_1i_2i_3i_4i_5}\mathcal{I}^D_{5;\,i_1i_2i_3i_4i_5} \\
&+ \sum_{[i_1|i_4]}\left(d^{(0)}_{i_1i_2i_3i_4}\mathcal{I}^D_{4;\,i_1i_2i_3i_4} - \frac{(D-4)}{2}d^{(2)}_{i_1i_2i_3i_4}\mathcal{I}^{D+2}_{4;\,i_1i_2i_3i_4} + \frac{(D-2)(D-4)}{4}d^{(4)}_{i_1i_2i_3i_4}\mathcal{I}^{D+4}_{4;\,i_1i_2i_3i_4}\right) \\
&+ \sum_{[i_1|i_3]}\left(c^{(0)}_{i_1i_2i_3}\mathcal{I}^D_{3;\,i_1i_2i_3} - \frac{(D-4)}{2}c^{(9)}_{i_1i_2i_3}\mathcal{I}^{D+2}_{3;\,i_1i_2i_3}\right) \\
&+ \sum_{[i_1|i_2]}\left(b^{(0)}_{i_1i_2}\mathcal{I}^D_{2;\,i_1i_2} - \frac{(D-4)}{2}b^{(9)}_{i_1i_2}\mathcal{I}^{(D+2)}_{2;\,i_1i_2}\right) + \sum_{[i_1|i_1]} a^{(0)}_{i_1}\mathcal{I}^D_{1;\,i_1}\,, \qquad (2.11)
\end{aligned}
$$

where the coefficients in front of the scalar integrals are part of the parameterisation of the integrand as in Eq. (2.1) and Eqs. (2.5)-(2.9). Finally, the parameterisation of the integrand and the basis of master integrals we have chosen to use makes it clear that the coefficients $e^{(0)}$, $d^{(0,2,4)}$, *etc.* are all independent of the dimensionality D - this is essential for when we use a numerical technique to obtain them below. We have shown that tensor integrals can be written in terms of a basis of scalar integrals, and now we turn to an algebraic method of calculating the coefficients for a general tensor integral.

2.1.2 Obtaining the reduction coefficients efficiently

Knowing that the basis in Eq. (2.4) exists and having a parameterisation of the integrand through Eq. (2.2) and Eqs. (2.5)-(2.9) is very powerful when trying to extract values of the reduction coefficients $\bar{e}$, $\bar{d}$, etc. In this section we describe an algebraic procedure which determines the coefficients efficiently, based on the knowledge that we can evaluate Eq. (2.2) for different values of l and match for coefficients.

The procedure makes use of the fact that for certain values of l, many of the terms on the RHS of Eq. (2.2) vanish – these are values of l which set a number of inverse propagators, d_i, to zero. This is very suggestive of a connection to on-shell methods for calculating amplitudes, and this link will be made below – here, we are still simply considering a single tensor integral. It should also be kept in mind that what is outlined below is very well suited to a numerical implementation, which we will discuss later in this Chapter.

We start by choosing $l = l^*$ is so that five of the denominators are zero, for example $d_1(l^*) = d_2(l^*) = d_3(l^*) = d_4(l^*) = d_5(l^*) = 0$. Such a value of l^* can always be found – to do so, however, the loop momentum needs to be in a dimension greater than four. It is also necessary when using this technique to use complex momenta for the loop momentum – solving the equations that put sets of denominators equal to zero in general requires this to be the case. A use of complex momenta has led to the discovery of wonderful structure in amplitudes (e.g. BCFW [27]), and we see its use in this technique for one-loop calculations too.

With the above value $l = l^*$, and after dividing through by all non-zero propagators, Eq. (2.2) becomes

$$\mathrm{Num}(l^*)/\left(\prod_{i \neq 12345} d_i\right) = \bar{e}_{12345}(l^*) \tag{2.12}$$

so that the coefficient $\bar{e}_{12345}(l^*) = e^{(0)}_{12345}$ is determined. Choosing other values of l which put different sets of five propagators to zero allows for a determination of all coefficients $\bar{e}^{(0)}_{i_1 \ldots i_5}$.

Once all of the 5-point coefficients have been found, the procedure turns to determining the four-point coefficients $\bar{d}_{i_1 i_2 i_3 i_4}(l)$. A value of l can then be chosen which puts a set of four denominators equal to zero, say $l = l^*$ so that[5] $d_1(l^*) = d_2(l^*) = d_3(l^*) = d_4(l^*) = 0$. In this step of the procedure, there are 5-point coefficient terms which are non-zero – for the example we have chosen they are those which involve

[5] For the sake of clarity, the $d_i(l^*)$s in this sentence represent denominators, not reduction coefficients.

$\bar{e}_{1234i}$, where $5 \leq i \leq N$ – but this presents no difficulty because they have already been determined in the previous step and we can simply subtract them from Eq. (2.2). The RHS of Eq. (2.2) is slightly more complicated than in the previous step, as we have (after dividing through by all of the non-zero propagators)

$$\left(\text{RHS of Eq. (2.2)} - \sum_{i \neq 1234} \frac{e_{1234i}}{d_i}\right) = \bar{d}_{1234}(l^*) =$$
$$d^{(0)}_{1234} + d^{(1)}_{1234}(l^* \cdot n_4) + d^{(2)}_{1234}(l^* \cdot n_\epsilon)^2 + d^{(3)}_{1234}(l^* \cdot n_\epsilon)^2(l^* \cdot n_4) + d^{(4)}_{1234}(l^* \cdot n_\epsilon)^4 \,. \tag{2.13}$$

However, there is freedom in choosing l^*, and five different values are needed to determine the five coefficients in Eq. (2.13) above. Again, this requires l to have dimension greater than four and to take complex values. In fact, infinitely many solutions l^* can be found – this is useful numerically – and what is more, l^* can be first chosen with $(l^* \cdot n_\epsilon) = 0$ to determine the first two coefficients in Eq. (2.13) , and then with $(l^* \cdot n_\epsilon) \neq 0$ to determine the other three.

These steps are repeated in turn to find the $\bar{c}$, $\bar{b}$ and finally the $\bar{a}$ coefficients by setting sets of three, two and then one denominators equal to zero. The details can be found in [3, 26], in particular the analytic forms of l^* which solve the denominator conditions. As the work in this thesis involves collaboration with some of the authors of [26], a computer code implementing the procedure was already available, and so a more detailed presentation of the above is left out of this thesis.

2.1.3 Taking the $\epsilon \to 0$ limit

There are a certain number of simplifications which occur when the physical limit $\epsilon \to 0$ relevant for LHC predictions is taken. In four dimensions, the five-point scalar integral can be re-expressed as a linear combination of four-point scalar integrals

$$\lim_{D \to 4-2\epsilon} \left(\sum_{[i_1|i_5]} e^{(0)}_{i_1 \ldots i_5} \mathcal{I}^D_{5;\, i_1 \ldots i_5} + \sum_{[i_1|i_4]} d^{(0)}_{i_1 \ldots i_4} \mathcal{I}^D_{4;\, i_1 \ldots i_4} \right) = \sum_{[i_1|i_4]} \tilde{d}^{(0)}_{i_1 \ldots i_4} \mathcal{I}^{4-2\epsilon}_{4;\, i_1 \ldots i_4} + \mathcal{O}(\epsilon) \,, \tag{2.14}$$

producing what was given in Eq. (2.4). However, there can be large cancellations which occur between the five-point coefficients $e^{(0)}_{i_1\dots i_5}$ and the four-point coefficients $d^{(0)}_{i_1\dots i_4}$ which in a numerical implementation can lead to instabilities. It is more preferable not to use $\mathcal{I}^D_{5;\,i_1\dots i_5}$ as a basis integral, but rather to use the same integral but with a $(l.n_\epsilon)^2$ in the numerator [28]. This is possible because for the five-point integral, $(l.n_\epsilon)^2$ takes a constant value (for given external momenta), and the benefit comes because the limit of this new master integral,

$$\lim_{D\to 4}\int \frac{\mathrm{d}^D l}{i\pi^{D/2}}\frac{(l.n_\epsilon)^2}{d_{i_1}d_{i_2}d_{i_3}d_{i_4}d_{i_5}} = 0\,, \tag{2.15}$$

means that no large cancellations take place. The $e^{(0)}_{i_1\dots i_5}$ coefficient is only used as a subtraction term in the procedure described above. This choice of master integral basis also has the advantage that any four dimensional relations between integrals remain manifest.

Finally, we give values for the integrals which embody the rational terms of the amplitude in the $\epsilon \to 0$ limit as well. The six-dimensional four-point integral vanishes and, as described above, the $(D-4)$ factors hitting the UV poles of the remaining integrals leave finite results:

$$\lim{}_{D\to 4}\quad \frac{(D-4)(D-2)}{4}\mathcal{I}^{D+4}_{4;\,i_1i_2i_3i_4} = -\frac{1}{3} \tag{2.16}$$

$$\lim{}_{D\to 4}\quad \frac{(D-4)}{2}\mathcal{I}^{D+2}_{4;\,i_1i_2i_3i_4} = 0 \tag{2.17}$$

$$\lim{}_{D\to 4}\quad \frac{(D-4)}{2}\mathcal{I}^{D+2}_{3;\,i_1i_2i_3} = \frac{1}{2} \tag{2.18}$$

$$\lim{}_{D\to 4}\quad \frac{(D-4)}{2}\mathcal{I}^{D+2}_{2;\,i_1i_2} = -\frac{m^2_{i_2}+m^2_{i_2}}{2} + \frac{1}{6}(q_{i_1}-q_{i_2})^2\,. \tag{2.19}$$

These give rise to the rational part, $\mathcal{R}$ in Eq. (2.4).

2.2 Generalised D-dimensional Unitarity Part II: Full 1-loop amplitudes

The above method can be applied to evaluate general one-loop, N-point Feynman diagrams in the standard model, as these are precisely N-point tensor integrals of rank $r \leq N$. We are interested in calculating full scattering amplitudes in this theory in order to make predictions for experiments such as the LHC, and since amplitudes are just a sum over Feynman diagrams, the method described above can of course yield results for amplitudes too if it is applied to each of the Feynman diagrams in turn. In this section, we will first address some disadvantages in proceeding in this fashion. The main problem is that the number of Feynman diagrams to describe an N-particle scattering amplitude grows factorially with N, and applying the above technique to a very large number of diagrams is very computationally intensive. What is more, the nature of gauge theories is such that large cancellations tend to occur between different Feynman diagrams. If the amplitudes are to be calculated numerically (and as we will discuss below, they necessarily are for higher multiplicity processes), then these large gauge cancellations can give rise to numerical instabilities. We shall see that this problem is ameliorated by working with full one-loop amplitudes, rather than individual Feynman diagrams.

The latter part of this section will lay out how this method can then be applied in practice to the calculation of multi-particle, one-loop amplitudes for LHC processes. Although the above procedure can be carried out analytically for simple calculations (see e.g. [26]), this becomes very difficult for $2 \to 3$ and $2 \to 4$ processes such as the ones presented in this thesis[6]. It becomes necessary to resort to evaluating these amplitudes numerically. In terms of making phenomenological predictions for LHC physics, the amplitudes have to be numerically integrated over phase space

[6]See however Ref. [29] which details an analytic calculation of $pp \to H + 2j$.

and convoluted with parton density functions anyway, so from this point of view, the only difference between an analytical and a numerical description of a one-loop amplitude is the implication for the speed at which it can be evaluated for given input momenta, along with issues of numerical stability (analytic computations tend to be more stable). The procedure laid out in the previous section is very well suited to a numerical implementation – we conclude this Chapter by describing the further considerations that need to be made to do this, which completes the description of the D-dimensional unitarity technique used for the calculations in this thesis.

2.2.1 Cyclic Ordering

A feature of the above method is that denominators appearing in the definition of the integral Eq. (2.1) have the ordering of the external particles around the loop embedded into their definition. For a single tensor integral, this is of no consequence, but if we want to compute sums of tensor integrals (i.e. sums of one-loop Feynman diagrams) at the same time using this method then we can run into problems, because the ordering of external particles is in general different and the different contributions cannot all be collected over the common denominator in Eq. (2.1). Since this is the starting point for the reduction procedure from which everything else follows, we are led to considering sets of tensor integrals which have the same cyclic ordering of particles – such a set can then still be written in the form of Eq. (2.1), where now $\mathrm{Num}(l)$ (which also appears in Eq. (2.2)) receives contributions from all of the tensor integrals in the set.

We shall first discuss a natural way in non-abelien gauge theories such as QCD in which to organise the contributions from the Feynman diagrams in a given amplitude into cyclically ordered sets, at both tree and loop level. This is the technique of colour ordering [30], and the ordered sets form sub-amplitudes which are gauge invariant – they are known as primitive amplitudes. An important consequence of dealing with colour ordered (or cyclic) amplitudes is that when carrying out the procedure for finding the reduction coefficients of a one-loop colour ordered amplitude, the Num(l) on the LHS of Eq. (2.2) becomes a product of tree-level colour ordered amplitudes for each value of l^*. We will discuss this in greater detail below, and then proceed to describe a prescription for dealing with colourless particles in an amplitude, as such particles cannot be colour ordered.

Our eventual aim will be to remove ourselves from the language of Feynman diagrams, dealing purely in terms of amplitudes everywhere in the calculation. However, it is useful to have in mind the representation of an amplitude as a sum over Feynman diagrams, and we will make much use of this picture below.

Colour ordering

The Feynman rules for the interactions of quarks and gluons involve both $SU(3)$ group-theoretic colour factors and kinematic factors. The colour factor for the quark-gluon vertex comes is $(T^a)_i^{\bar{j}}$, where a is the gluon colour index, and i and $\bar{j}$ are quark and antiquark colour indices, and the colour factor for the three gluon vertex is f^{abc} - the structure function of $SU(3)$. The four gluon vertex has a colour factor which is $f^{abe}f^{cde}$. A Feynman diagram is a product of a colour structure and a kinematic function obtained from the Feynman rules. When considering an amplitude, the kinematic functions from each of the contributing Feynman diagrams may be grouped according to the particular colour structure they multiply. This is known as a colour decomposition of the amplitude, and it provides a very useful way of organising a calculation. There is a freedom in choosing the basis colour structures to use, and identities such as

$$f^{abc} = -\tfrac{i}{\sqrt{2}}\mathrm{Tr}(T^aT^bT^c - T^bT^aT^c) \tag{2.20}$$

$$\text{and} \qquad (T^a)_{i_1}^{\bar{j}_1}(T^a)_{i_2}^{\bar{j}_2} = \delta_{i_1}^{\bar{j}_2}\delta_{i_2}^{\bar{j}_1} - \tfrac{1}{N_c}\delta_{i_1}^{\bar{j}_1}\delta_{i_2}^{\bar{j}_2} \tag{2.21}$$

can be applied to recast colour structures in terms of the chosen basis and reduce more complicated ones. These identities make clear that the kinematic function associated with a given Feynman diagram may contribute to the coefficient of more than one particular basis colour structure.

In Ref. [31], a colour decomposition to a particular set of independent colour structures was found for which the kinematic coefficients are what are known as *primitive amplitudes* – purely kinematic functions which receive contributions only from diagrams which have a fixed cyclic ordering of external legs[7], and which are gauge invariant. We reproduce the general formula of Ref. [31] in App. A for amplitudes relevant to the work in this thesis which involve a quark-antiquark pair and gluons. We will also explicitly give the colour decompositions for the specific processes considered in this thesis as we come to them below. The significance of performing this colour decomposition is that:

- The one-loop primitive amplitudes are cyclically ordered, so that the OPP reduction method can be applied to evaluate them.

- Primitive amplitudes are gauge invariant both at tree and one-loop level[8], so that the expected simplifications of formula (or numerically, large cancellations between diagrams) take place at this base level of the calculation where they do not have such a large impact.

These are two features which we will retain with our prescription for dealing with colourless particles described below.

Primitive amplitudes can be directly obtained by summing over all possible Feynman diagrams with the correct cyclic ordering of external particles and using a modified set of *colour ordered* Feynman rules (App. A, [32, 33]). These are the standard

[7]The kinematic coefficients of a generic colour decomposition do not necessarily have these features. In this decomposition, the primitive amplitudes are also all independent, so there is no redundancy (as there can be in some colour decompositions).

[8]The independence of the colour structures ensures this, if the full amplitude is gauge invariant.

rules for quark and gluon interactions but which have been modified by stripping away the colour factors (negative signs relate vertices with different cyclic ordering of the particles, and factors of $\sqrt{2}$ account for the removed structure constants). Recursion relations based on these colour ordered rules can also be used to obtain the primitive amplitudes, without giving any reference to Feynman diagrams.

Unitarity cuts

We now consider a generic N-particle, one-loop, cyclically ordered primitive amplitude:

$$\mathcal{A}_{(D)}(\{p_i\},\{\epsilon_i\}) = \int \frac{\mathrm{d}^D l}{i\pi^{D/2}} \frac{\mathcal{N}(\{p_i\},\{\epsilon_i\};l)}{d_1 d_2 \ldots d_N} \,. \tag{2.22}$$

The procedure of Section 2.1.2 can be followed to find the parameterisation of the integrand numerator $\mathcal{N}(\{p_i\},\{\epsilon_i\};l)$ in terms of the OPP reduction coefficients. However, in selecting the various values of $l = l^*$ which put sets of 5, 4, ... 1 of the denominators appearing in Eq. (2.22) to zero, the amplitude factorises into a product of 5, 4, ..., 1 tree-level amplitudes[9]. So for example, finding the coefficient $\bar{d}_{1234}$, as in Section 2.1.2 (see Eq. (2.13)), we would find

$$\begin{aligned}\bar{d}_{1234} &= \mathrm{Res}\left[\frac{\mathcal{N}(\{p_i\},\{\epsilon_i\};l)}{d_1 d_2 \ldots d_N} - \sum_{i\neq 1,2,3,4} \frac{\bar{e}_{1234i}}{d_1 d_2 d_3 d_4 d_i}\right] \\ &= \sum \mathcal{A}^{\text{tree}}_{(D)}(-l_4, p_5, \ldots, p_N, p_1, l_1) \times \mathcal{A}^{\text{tree}}_{(D)}(-l_1, p_2, l_2) \times \mathcal{A}^{\text{tree}}_{(D)}(-l_2, p_3, l_3) \times \mathcal{A}^{\text{tree}}_{(D)}(-l_3, p_4, l_4)\end{aligned} \tag{2.23}$$

which is a product of tree level primitive D-dimensional amplitudes $\mathcal{A}^{\text{tree}}_{(D)}$, and where the $\sum$ and $\times$ represent a sum over all the internal states (particle type, helicity, colour *etc.*). This factorisation is shown schematically in Fig. 2.2. In this way, all of the reduction coefficients which specify the full one-loop amplitude can be obtained by

[9]That is, the residue of the integrand is given by a product of tree-level amplitudes.

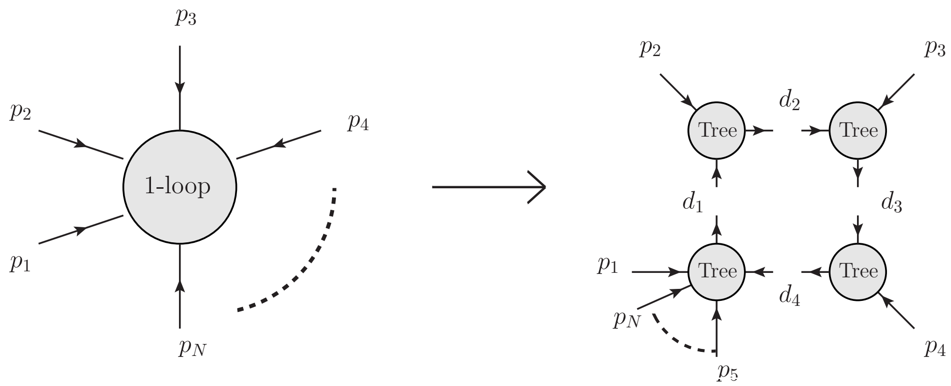

Figure 2.2: Schematic diagram to illustrate the factorisation of the integrand into tree level amplitudes when finding the reduction coefficient $\bar{d}_{1234}$.

evaluating products of simple tree-level amplitudes. We will refer to the evaluation of the one-loop amplitude at these values of $l = l^*$ where it factorises into 5, 4, . . ., 1 tree-level amplitudes as unitarity 5-, 4-, . . ., 1-cuts of the amplitude. This is reminiscent of on-shell techniques for 'sewing' together tree-level amplitudes and using dispersion relations to obtain the loop amplitude [34, 35], although no dispersion integral has to be performed here – this is an advantage gained in being able to match for coefficients at the level of the integrand.

Colourless particles

If colourless particles, such as weak bosons, are present in an amplitude, then a colour decomposition does not fix the ordering of all of the external particles. To proceed with using the D-dimensional generalised unitarity technique, we impose a further artificial ordering on the colourless particles in the one-loop amplitude, and we separately consider each possible such ordering so as to pick up all possible contributions to the full amplitude. However, in order to retain the feature that when a unitarity cut is made, a product of full tree-level amplitudes is evaluated, this artificial ordering is relaxed at this stage of the procedure. That is, the tree-level amplitudes entering e.g. the RHS of Eq. (2.23) include all possible orderings of the colourless particles relative to the coloured (ordered) ones.

This prescription leads to an over-counting of contributions, so we have to be able to identify and throw away the overlapping contributions from the different artificial orderings of the one-loop amplitude. Such identification is usually easy to automate, and we defer a detailed discussion of this issue until we come to the specific examples in this thesis.

2.2.2 Numerical Implementation

In order to implement the above technique in a numerical program, the number of dimensions D in which the virtual particles propagate has to be an integer, so that the momentum and polarisation vectors are numerically well defined. While this presents no particular obstacle in carrying out the above procedure, we would like to eventually obtain one-loop amplitudes in the physical limit $D = 4$ in order to make LHC predictions. This section summaries how this limit is achieved in the framework of D-dimensional generalised unitarity.

Following Ref. [3], the dimensional dependence of a one-loop amplitude is extended by defining the polarisation vectors of the internal loop particles in D_s dimensions, distinct from the D dimensions that their momentum vector is specified in[10]. The D_s dependence of the amplitude only appears in the numerator of Eq. (2.22) i.e.

$$\mathcal{A}_{(D,D_s)}(\{p_i\},\{\epsilon_i\}) = \int \frac{\mathrm{d}^D l}{i\pi^{D/2}} \frac{\mathcal{N}^{(D_s)}(\{p_i\},\{\epsilon_i\};l)}{d_1 d_2 \ldots d_N} \,. \tag{2.24}$$

With the external particles kept in four dimensions, the numerator depends linearly[11] on D_s as it arises from a loop of contracted Lorentz indices (i.e. a loop constructed of

[10]For consistency $D_s \geq D$ is required [36].

[11]With the exception of amplitudes involving fermion loops, which are discussed at the end of this Section.

Dirac Γ matrices and metric tensors arising from the propagators of particles in the loop), and there can only be one such loop in a one-loop amplitude. The numerator can be written as

$$\mathcal{N}^{(D_s)}(l) = \mathcal{N}_0(l) + (D_s - 4)\mathcal{N}_1(l)\,, \tag{2.25}$$

where $\mathcal{N}_0$ and $\mathcal{N}_1$ are free from explicit D_s dependence[12]. $\mathcal{N}^{(D_s)}$ appearing in Eq. (2.24) and (2.25) is just what can be obtained using the unitarity procedure and this can be done numerically by choosing integer values for D and D_s so that the momentum and polarisation vectors are well defined (see e.g. Ref. [26] for definitions of higher dimensional polarisation vectors – fermionic ones require an even value of D_s). By evaluating Eq. (2.25) twice, for $D_s = D_1, D_2$ (both integer), we can invert it to obtain: $\mathcal{N}_0$ and $\mathcal{N}_1$

$$\begin{aligned} \mathcal{N}_0(l) &= \frac{(D_2-4)\mathcal{N}^{(D_1)}(l) - (D_1-4)\mathcal{N}^{(D_2)}(l)}{D_2 - D_1}\,, \\ \mathcal{N}_1(l) &= \frac{\mathcal{N}^{(D_1)}(l) - \mathcal{N}^{(D_2)}(l)}{D_2 - D_1}\,. \end{aligned} \tag{2.26}$$

Once these are known, we know the amplitude $\mathcal{A}_{(D,D_s)}$ in any D_s dimension through Eq. (2.25), and so we can extrapolate to e.g. $D_s \to 4$ (this defines the four dimensional helicity scheme, FDH)

$$\mathcal{A}^{\mathrm{FDH}} = \left(\frac{D_2-4}{D_2-D_1}\right)\mathcal{A}_{(D,D_s=D_1)} - \left(\frac{D_1-4}{D_2-D_1}\right)\mathcal{A}_{(D,D_s=D_2)}\,. \tag{2.27}$$

We emphasise that the amplitudes $\mathcal{A}_{(D,D_s=D_1)}$ and $\mathcal{A}_{(D,D_s=D_2)}$ in Eq. (2.27) can be evaluated numerically by choosing integer dimensions D and D_s and by using the unitarity procedure outlined in this Chapter. It is a novel feature of the technique

[12] In the sense that, although they do contain polarisation matrices in D_s dimensions, the values of $\mathcal{N}_{0,1}$ are unchanged by the choice of D_s and can be used to obtain $\mathcal{N}^{(D_s)}$ for any value of D_s through Eq. (2.25).

being presented here that physical one-loop amplitudes are obtained by working with tree-level amplitudes in higher spatial dimensions which are evaluated with complex momenta. The physical one-loop amplitude is obtained through the knowledge of the D_s dependence of the amplitude, as has been used in Eq. (2.27) to give the amplitude in the FDH scheme, and through the fact that the reduction coefficients are independent of D – that the scalar integrals they multiply can be evaluated analytically in a physical limit i.e. for $D \to 4 - 2\epsilon$ at the end of the calculation. In this thesis, we always choose $D = 5$ (as this is the simplest), $D_1 = 6$, and $D_2 = 8$ (both even so that fermion polarisation vectors are well defined) in Eq. (2.27).

Finally, if the amplitude involves only closed fermion loops, it only needs evaluating at a single D_s, because the D_s dependence only appears through the normalisation of the trace of Dirac gamma matrices, that is

$$\mathcal{N}_f^{(D_s)}(l) = t_{D_s} \mathcal{N}_{0,f}(l)\,, \tag{2.28}$$

where $\mathrm{Tr}(\Gamma^\mu \Gamma^\nu) = t_{D_s} 4 g^{\mu\nu}_{D_s}$, with $t_{D_s} = 2^{(D_s-4)/2}$.

2.3 Chapter Summary

We have presented the new technique of D-dimensional generalised unitarity, which is a novel and efficient method of obtaining one-loop scattering amplitudes in the standard model. By working with full amplitudes rather than individual Feynman diagrams, and by matching for coefficients rather than explicitly reducing tensor integrals, the problems encountered in using traditional approaches to many-particle, one-loop calculations are avoided. We will proceed to apply this technique in this thesis to perform new one-loop calculations: to the process $gg \to W^+W^-g$ and the process $pp \to W^+W^- + 2j$, both presented in Chapter 4, and to the process $pp \to W^+W^- + 2j$, presented in Chapter 5. Before this, however, we will discuss how the one-loop amplitude fits into the general set-up of a full NLO QCD calculation. The one-loop amplitudes contributing to $pp \to W^+W^- + 1j$, which is used as an example process in the next Chapter, are also obtained using D-dimensional generalised unitarity.

Chapter 3

An NLO QCD Calculation: $pp \to W^+W^- + 1j$

Chapter Overview

To give an overview of the procedure followed for the NLO calculations in this thesis, in this Chapter we will describe in detail the computation of the QCD corrections to the process $pp \to W^+W^- + 1j$. This will serve to introduce the main components of such a calculation, how the short-distance (perturbative) leading order, virtual, and real emission matrix elements are obtained, how they all fit together, how to deal with the IR divergences of the virtual and real contributions, and the checks which can be performed to ensure the correct result is obtained.

The NLO QCD corrections to this process have previously been calculated and published in Refs. [16, 17, 37], and a detailed comparison between results has also been carried out, with full agreement found [18]. The independent calculation presented here is the first which is carried out using the technique of D-dimensional generalised unitarity, so it is a good illustration of the techniques presented in the previous Chapter. Another main motivation for revisiting this process is the lack of a public code available for the NLO description – in order to perform the research into an NNLO contribution to this process (which is work presented in the following Chapter), the NLO QCD corrections must first be known, and available. The calculation described here has been made available in the form of a public code, and can be downloaded from the website [38]. For the purposes of this Chapter, it is an ideal process to study, because being a $2 \to 3$ particle calculation, it is somewhat simpler than the $2 \to 4$ processes studied later in this thesis, while at the same time exhibiting almost all of the important features of these more difficult calculations. Any additional technicalities encountered in the subsequent calculations will be dealt with when they are met, but for the most part, reference can be made to this calculation, with straightforward extensions of the ideas presented here.

This Chapter is laid out in the following way. In section Sec. 3.1, we present the general set-up of an NLO calculation, and in Sec. 3.2 we detail the calculation of the hard scattering matrix elements to the process $pp \to W^+W^- + 1j$. Sec. 3.3 provides an overview of the Catani-Seymour dipole formalism used in this thesis, and we discuss the checks made on this calculation in Sec. 3.4. Finally we present some results of the NLO QCD calculation of this process in Sec. 3.5 and summarise this Chapter in Sec. 3.6

3.1 A general NLO prescription

We will being by describing a general NLO QCD calculation, following the organisation and notation of the seminal Catani-Seymour paper (CS from now on, Ref. [5]). The cross section for a process at the LHC, which involves two initial state protons of momentum p and $\bar{p}$, is given by

$$\sigma(p,\bar{p}) = \sum_{a,b} \int_0^1 dx_1 \; f_a(x_1,\mu_F^2) \int_0^1 dx_2 \; f_b(x_2,\mu_F^2) \left[\sigma_{ab}^{LO}(x_1 p, x_2 \bar{p}) + \sigma_{ab}^{NLO}(x_1 p, x_2 \bar{p}; \mu_F^2)\right] \tag{3.1}$$

where $f_a(x_1,\mu_F^2)$ and $f_b(x_2,\mu_F^2)$ are the parton densities of the incoming protons for partons a and b, evaluated at momentum fraction of the proton $x_{1/2}$, and at a factorisation scale μ_F, and where

$$\sigma_{ab}^{LO}(p,\bar{p}) = \int_m d\sigma_{ab}^{B}(p,\bar{p}), \tag{3.2}$$

$$\sigma_{ab}^{NLO}(p,\bar{p};\mu_F^2) = \int_m d\sigma_{ab}^{V}(p,\bar{p}) + \int_{m+1} d\sigma_{ab}^{R}(p,\bar{p}) + \int_m d\sigma_{ab}^{C}(p,\bar{p};\mu_F^2). \tag{3.3}$$

Here, the hard scattering 'Born' (or LO) contribution $d\sigma_{ab}^{B}(p,\bar{p})$ is given by

$$d\sigma_{ab}^{B}(p,\bar{p}) = \frac{1}{\mathcal{N}_n} d\Phi_m \left|\mathcal{M}_{ab}^{m}(p,\bar{p};p_1,p_2,\ldots,p_m)\right|^2, \tag{3.4}$$

where $\mathcal{M}_{ab}^{m}$ is the tree-level matrix element with incoming partons a and b of momentum p and $\bar{p}$, and with m final state external particles of momentum $p_1 \ldots p_m$, and where $d\Phi_m$ is m particle phase space. All symmetry, averaging and flux factors are accounted for by the overall factor of $\mathcal{N}_n$. This cross section has to be defined in such a way so that it has a safe infrared limit – in this case this requires making cuts on the jet in the final state to prevent it from going too soft or collinear with respect to the initial partons (these are cuts that would be made experimentally anyway, e.g. jet transverse momentum $p_{t,j} > 30\,\mathrm{GeV}$ and jet rapidity $|\eta_j| < 3$). If there were two jets in the final state, the conditions for this contribution would include the requirement that both jets are separately resolved in the final state, again so as to avoid any infrared divergences at this order of the calculation. Similarly we have

$$d\sigma_{ab}^{V}(p,\bar{p}) = \frac{1}{\mathcal{N}_m} d\Phi_m \ 2\ \mathrm{Re}\left[\mathcal{M}_{ab}^{m\ *}(p,\bar{p};p_1,\ldots,p_m)\cdot\mathcal{M}_{ab}^{m\ \text{1-loop}}(p,\bar{p};p_1,\ldots,p_m)\right], \quad (3.5)$$

$$d\sigma_{ab}^{R}(p,\bar{p}) = \frac{1}{\mathcal{N}_{m+1}} d\Phi_{m+1}\ |\mathcal{M}_{ab}^{m+1}(p,\bar{p};p_1,\ldots,p_{m+1})|^2\,, \quad (3.6)$$

where the $\mathcal{M}_m^{1-loop}$ appearing in Eq. (3.5) is the renormalised one-loop matrix element, $\mathcal{M}_{ab}^{m+1}$ is a tree-level matrix element with one additional parton in the final state, and $\mathcal{N}_m$ and $\mathcal{N}_{m+1}$ take into account averaging factors.

The same phase space restrictions apply to the final state partons in the virtual contribution, $d\sigma^V$, as in the LO contribution (i.e. for our process $pp \to W^+W^- + 1j$ these are the cuts on the jet). The real contribution $d\sigma^R$, however, involves an extra QCD parton in the final state, which now can go collinear or soft with respect to the other partons. IR singularities can and do develop, but for infrared safe observables (the cross sections and differential cross sections which we consider in this thesis are all infrared safe observables) these singularities will all cancel with the IR singularities of the virtual cross section and those coming from the contribution $d\sigma_{ab}^C$, which is called the collinear counter term and is described below. This cancellation is discussed in more detail in Sec. 3.3, where the formalism to deal with these singularities in a numerical calculation is introduced.

The role of the collinear counter term is to cancel the singularities arising from the real contribution in some areas of phase space where final state particles become collinear with initial state partons – these are singularities which are not cancelled by the IR singularities of the virtual contribution. Instead, they must be absorbed into the definition of the parton distributions functions (PDFs), in much the same way as UV singularities are absorbed into couplings of the Lagrangian. The collinear counter term is the remnant of doing this (i.e. the parton distribution functions are already 'renormalised' in this way, the collinear counter term being the negative of the singularities which have been absorbed). It is given by the following expression

$$\begin{aligned} d\sigma^C_{ab}(p,\bar{p};\mu_F^2) &= -\frac{\alpha_S}{2\pi}\frac{1}{\Gamma(1-\epsilon)}\sum_{cd}\int_0^1 dz\int_0^1 d\bar{z}\ \ d\sigma^B_{cd}(zp,\bar{z}\bar{p}) \\ &\cdot \left\{\delta_{bd}\delta(1-\bar{z})\left[-\frac{1}{\epsilon}\left(\frac{4\pi\mu^2}{\mu_F^2}\right)^\epsilon P^{ac}(z)+K^{ac}_{\text{F.S.}}(z)\right]\right. \\ &+ \left.\delta_{ac}\delta(1-z)\left[-\frac{1}{\epsilon}\left(\frac{4\pi\mu^2}{\mu_F^2}\right)^\epsilon P^{bd}(\bar{z})+K^{bd}_{\text{F.S.}}(\bar{z})\right]\right\}\ . \end{aligned} \tag{3.7}$$

The $P^{ab}(z)$ appearing in this equation are the Altarelli-Parisi splitting functions [39], α_s is the strong coupling constant, and the IR singularities have been regularised using dimensional regularisation and appear as poles in $1/\epsilon$ – the scale μ originates from this procedure. The scale at which the PDFs have been renormalised is the factorisation scale, μ_F, and the $K^{ab}_{\text{F.S.}}(z)$ appearing in Eq. (3.7) are functions which define the factorisation scheme. Below we work in the $\overline{\text{MS}}$ scheme, in which case $K^{ac}_{\text{F.S.}}(z) = K^{bd}_{\text{F.S.}}(\bar{z}) = 0$.

3.2 Matrix elements for $pp \to W^+W^- + 1j$

Focusing now on the specific process $pp \to W^+W^- + 1j$, we shall describe the calculation of the matrix elements required for the LO, virtual and real contributions to the cross section. This beings with a discussion of the recursion relations used to obtain all of the tree level amplitudes needed in the calculation.

3.2.1 Berends-Giele recursion relations

Basic objects which are needed to calculate the LO and real contributions are clearly tree-level scattering amplitudes, as these contributions are tree-level processes. But as we have seen above, the method of D-dimensional unitarity allows one to reconstruct one-loop amplitudes from products of tree-level amplitudes as well. This section describes the method in which these fundamental building blocks are obtained throughout this thesis.

The use of on-shell recursion relations such as BCFW to calculate tree-level amplitudes can lead to some striking and beautiful expressions, revealing symmetries that are completely obscured by summing over Feynman diagrams. Such expressions can be very compact, which is an advantage if they are to be implemented in a computer program where they will be evaluated hundreds of thousands of times. However, for the calculations in this thesis we will use Berends-Giele off-shell recursion relations [40] which *are* very closely related to a Feynman diagram expansion – they can easily be visualised as such. The advantages of using these recursion relations will be made clear in this section.

In their original form, Berends-Giele recursion relations address colour ordered amplitudes, and this is the form in which we shall use them. In Ref. [40], the authors define an off-shell gluon current to be a cyclically ordered n-gluon amplitude, where one of the gluons has its polarization vector removed and is taken off-shell. The recursion relation follows by noticing that this off-shell gluon splits into either two or three off-shell gluons, each of which can be described by a smaller off-shell gluon current. Because the amplitude is colour ordered, this in turn limits the ordering of the gluons within each branching. The recursion proceeds by summing over all possible splittings of the current into smaller currents (Fig. 3.1(a)), with the initial condition that one off-shell gluon is given by its polarization vector, ϵ^μ. Each time a three (four) vertex splitting occurs, an insertion of a the three(four)-point gluon vertex and multiplication by gluon propagators is required. Explicitly (using the notation of the review [26]), an off shell gluon current $G^\mu(g_1, g_2, \ldots, g_n)$ involving n

gluons $g_1 \dots g_n$ of momenta $k_1 \dots k_n$ satisfies the recursion

$$
\begin{aligned}
G^\mu(g_1, g_2, \dots, g_n) = &\sum_{m=1}^{n-1} V_3^{\mu\nu\rho}(-k_{1:n}, k_{1:m}, k_{m+1:n}) S^G_{\nu\nu'}(k_{1:m}) S^G_{\rho\rho'}(k_{m+1:n}) \\
&\quad \times G^{\nu'}(g_1, g_2, \dots, g_m) G^{\rho'}(g_{m+1}, \dots, g_n) \\
+ &\sum_{m=1}^{n-1} \sum_{k=m+1}^{n-1} V_4^{\mu\nu\rho\sigma}(-k_{1:n}, k_{1:m}, k_{m+1:k}, k_{k+1:n}) S^G_{\nu\nu'}(k_{1:m}) S^G_{\rho\rho'}(k_{m+1:k}) S^G_{\sigma\sigma'}(k_{k:n}) \\
&\quad \times G^{\nu'}(g_1, g_2, \dots, g_m) G^{\rho'}(g_{m+1}, \dots, g_k) G^{\sigma'}(g_{k+1}, \dots, g_n)\,,
\end{aligned}
\tag{3.8}
$$

where $V_3^{\mu\nu\rho}(k, k', k'')$ is the three gluon vertex, $V_4^{\mu\nu\rho\sigma}(k, k', k'', k''')$ is the four gluon vertex, $k_{i:j} = \sum_{m=i}^{j} k_m$, and $S^G_{\nu\nu'}(k_{1:m})$ is the gluon propagator (where it should be understood that if the splitting is into a single gluon current $G^{\nu'}(g_i) = \epsilon_i^{\nu'}$, this propagator factor is not included: $S^G_{\nu\nu'}(k_{i:i}) = g_{\nu\nu'}$).

Similar currents can also be defined for off-shell quark currents. Here, the colour ordered Feynman rules make a distinction between gluons emitted from the left hand side of a quark line and the right hand side of the quark line. The corresponding vertices are the negative of each other. An off-shell quark current is defined as a colour ordered amplitude with one quark line with n_1 gluons emitted from the left hand side of it and n_2 gluons from the right hand side, and where the quark has its polarization vector removed and is taken off-shell. The recursion relation follows in a very similar way, by noticing that moving away from the off-shell quark, there can be possible branching into a gluon (left hand side) and a quark, or into a gluon (right hand side) and a quark (Fig. 3.1 (b)). Each of these gluons and quarks defines another smaller off-shell gluon or quark current, and the quark-gluon vertex and propagator factors must be inserted in the same way as in the gluon recursion. The initial condition is that with no gluons, the current is equal to the polarization vector $\bar{u}$.

The description of currents with more than one quark line proceeds via a relatively

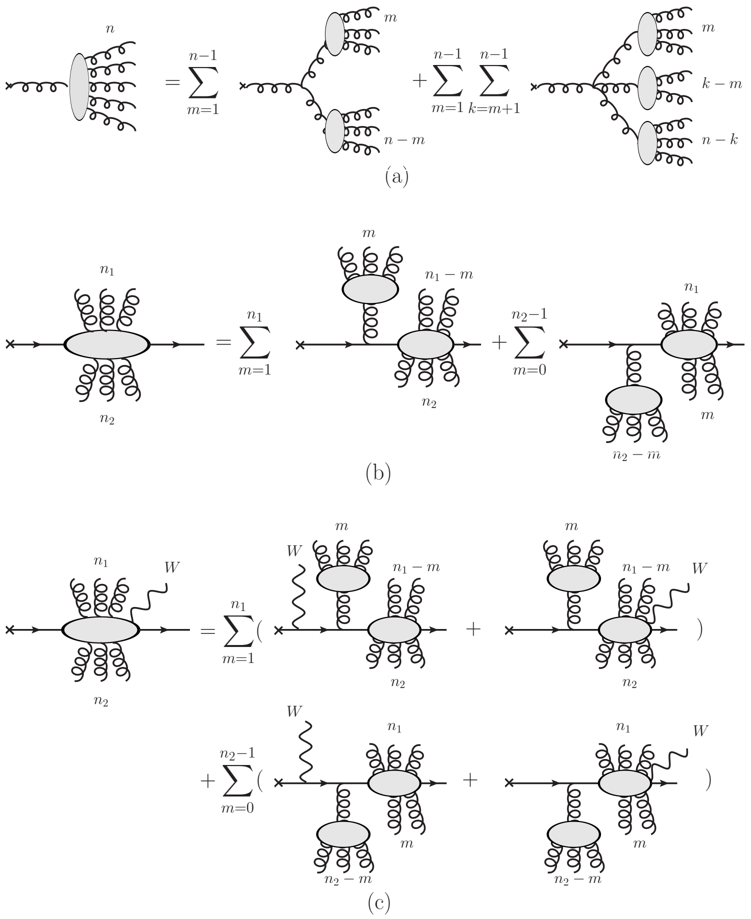

Figure 3.1: Berends-Giele recursion relations for (a) a gluon current, (b) a quark current, and (c) a quark current with a W boson attached.

straightforward generalisation of the above methods, and we will not detail this here. Currents with two quark lines are in fact needed in some part of the calculation of most of the QCD processes considered in this thesis. For a detailed description the reader is referred to Ref. [9, 11, 26].

Finally, the inclusion of colourless particles into these recursion relations is necessary to describe standard model processes with weak bosons at the LHC. This is also done in a straightforward way – colourless particles do not have any fixed ordering within the amplitude, and this requires that at each step of the recursion, every possible insertion of all colourless particles must be considered. A pictorial example of this is given in Fig. 3.1(c) which shows how an off-shell quark current which has a W

attached to it is built up. The amount of bookkeeping becomes slightly cumbersome for more complicated off-shell currents, such as those involving two quark lines and/or two colourless particles, but there are no new concepts involved.

The advantage of using Berends-Giele recursion relations is that they can immediately deal with any standard model amplitude – the inclusion of colourless weak bosons is straightforward, and massive particles in the recursion present no problems. These relations can be easily generalised to be applicable in D-dimensions and D_s spin dimensions, and they can be used with complex momenta, which means they are ideally suited for use with the D-dimensional unitarity technique. A gain can be made in a computer program by caching results for off-shell currents – this can speed up the implementation, especially when the number of particles becomes very large (see in particular [41], where amplitudes of up to 20 gluons are calculated with these recursion relations).

These simple but powerful recursion relations are at the heart of all of the NLO QCD unitarity calculations discussed in this thesis, as they are used every time there is a tree level amplitude to evaluate.

3.2.2 Helicity amplitudes

Because we are working numerically, the amplitudes we consider must be helicity amplitudes, where all of the external particles have a fixed helicity. Sums over all possible helicity assignments must be performed at the appropriate places in the calculation. For instance, a sum over the internal particles' helicities when a unitarity cut is made must be explicitly done by computing all the necessary helicity amplitudes. Similarly, all possible helicity assignments of external particles must be summed over to produce the full (unpolarised) result.

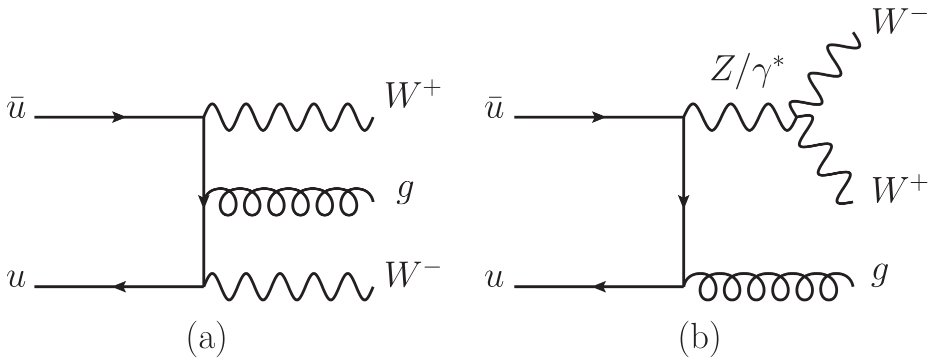

Figure 3.2: Two leading order Feynman diagrams for the amplitude $0 \to \bar{u}uW^+W^-g$ where (a) contributes to $A_0^{(WW)}([\bar{u}, W, W, u], g)$ and (b) to $A_0^{(Z/\gamma)}([\bar{u}, Z/\gamma, u], g)$.

3.2.3 Hard scattering contributions

We now turn to descriptions of each of the hard scattering contributions for the process $pp \to W^+W^- + 1j$.

Leading order

Fig. 3.2 shows two example Feynman diagrams which contribute to the leading order amplitude $0 \to \bar{u}uW^+W^-g$[1]. A quark line must be present for the weak bosons to couple to, from which it follows that the third parton has to be a gluon. If the Ws attach directly to the quark line (Fig. 3.2 (a)), then the order in which they appear is fixed by the electric charge of the quark line, and the quark has to be left handed (this restricts the helicity of the quark and antiquark, if they are massless). All possible insertions of the W bosons on the quark line relative to the gluon have to be considered – this is done automatically when using Berends-Giele recursion relations. The W bosons can also attach via an intermediate Z or γ (Fig. 3.2 (b)), which couple to both left and right handed quarks.

Although we refer to the process as WW production, these particles are not actually seen in the detector, rather it is their decay productions which are observed.

[1]We use a convention where all particles are outgoing in amplitudes.

Throughout this thesis, the W bosons are assumed to decay leptonically $W^+ \to \nu_l l^+$ and $W^- \to l^- \bar{\nu}_l$, where $l = e$ or μ. Rather than adding this decay at the end of the calculation, we directly compute amplitudes for $pp \to$ leptons + QCD jets [2], with fully differential distributions of lepton momenta, and taking into account all spin correlations and off-shell weak boson contributions [3]. This is done by setting the polarisation vectors of the weak bosons to be the matrix element for the full decay process. For example, the W^+ bosons have polarisation vectors

$$\epsilon_-^\mu(p_\nu, p_{l^+}) = \bar{u}(p_\nu)\gamma^\mu \frac{1}{2}(1-\gamma_5)v(p_{l^+})P_W(s_{\nu l^+}) \tag{3.9}$$

where $P_V(s_{\nu l^+}) = 1/((p_\nu + p_{l^+})^2 - M_V^2 + i\Gamma_V M_V)$ is a Breit-Wigner shaped propagator factor and can be defined for both $V = W, Z$. The polarization vector for the Z or $\gamma \to$ leptons is the matrix element including double resonant decay (Fig. 3.3 (a)) and also the single resonant diagrams (Fig. 3.3 (b)-(e)). For all of these decay matrix elements, the presence of a W boson restricts the leptons to having only one possible helicity assignment.

The colour ordered tree-level amplitude $A_0(\bar{q}_1, q_2, g_3)$ (see App. A) is defined by the following equation

$$\mathcal{A}^{\text{tree}}(\bar{q}_1, q_2, g_3; \nu_\mu, \mu^+, e^-, \bar{\nu}_e) = g_s \left(\frac{g_W}{\sqrt{2}}\right)^4 (T^{a_3})_{i_2}^{\bar{i}_1} A_0(\bar{q}_1, q_2, g_3)\,, \tag{3.10}$$

where g_s is the strong coupling constant, g_W is the weak coupling constant, and $(T^{a_3})_{i_2}^{\bar{i}_1}$ is the $SU(3)$ matrix of the fundamental representation, with gluon colour index a_3 and quark and antiquark colour indices i_2 and $\bar{i}_1$. The colour ordered amplitude

[2] We do *not* consider production of the like-flavour leptons final state from $pp \to ZZ$, which has a very different resonant structure. This can be calculated separately – the interference terms were shown in Ref. [10] to be negligible (for the $0j$ case).

[3] This is what is always meant in this thesis by WW+jets production. Amplitudes appearing without explicit leptonic arguments should be treated as shorthand versions of the full amplitude being calculated e.g. the argument $(\bar{q}_1, q_2, g_3)$ really means $(\bar{q}_1, q_2, g_3; \nu_\mu, \mu^+, e^-, \bar{\nu}_e)$.

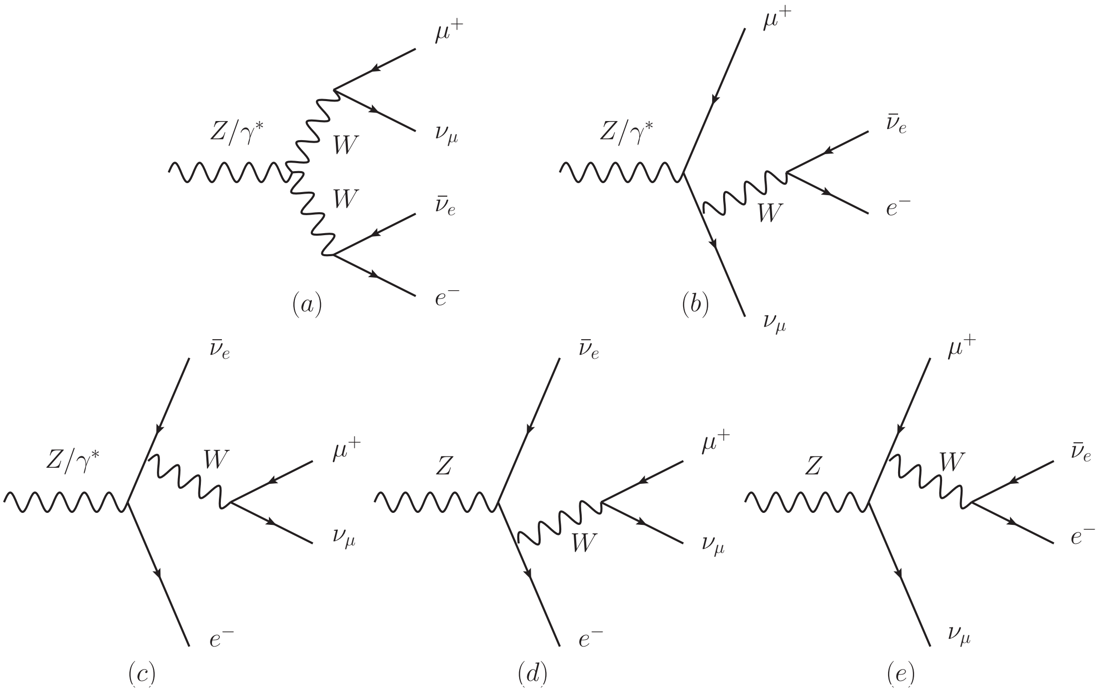

Figure 3.3: Double resonant diagram (a) and single resonant diagrams (b)-(e) which contribute to the Z or photon polarization vector.

has a further decomposition given by

$$\begin{aligned} A_0(\bar{q}_1, q_2, g_3) = A_0^{(WW)}([\bar{q}_1, W, W, q_2], g_3) \quad &+ \quad C_Z^{(q_2,h_2)} A_0^{(Z)}([\bar{q}_1, Z, q_2], g_3) \\ &+ \quad C_\gamma^{(q_2,h_2)} A_0^{(\gamma)}([\bar{q}_1, \gamma, q_2], g_3) \end{aligned} \tag{3.11}$$

where the different contributions from either Ws attaching directly or via an intermediate Z or γ are separated, as shown in Fig. 3.2. The factors $C_{Z/\gamma}^{(q_2,h_2)}$ give the coupling of the Z/γ to the quark line, and they are

$$\begin{aligned} C_\gamma^{(q,h)} &= Q^{(q)} \sin^2\theta_W \, , \\ C_Z^{(q,h)} &= T_3^{(h,q)} - Q^{(q)} \sin^2\theta_W \, , \end{aligned} \tag{3.12}$$

where $Q^{(q)}$ is the electromagnetic charge of the quark q, h is the helicity of the quark, $T_3^{(-,u)} = +1/2$, $T_3^{(-,d)} = -1/2$ and $T_3^{(+,q)} = 0$, and θ_W is the weak mixing angle.

The inclusion of single resonant diagrams requires the Z and the γ contributions to be treated on an unequal footing in Eq. (3.11), since the off-shell polarization vectors of the Z and the γ are not simply related as they would be (by a factor of the Z propagator over the γ propagator) when only double resonant contributions were included. Breit-Wigner shaped propagators are used whenever there is an intermediate vector boson appearing in the amplitude. The scheme used is not unique – the inclusion of a width involves contributions of all order in the perturbation series. However, at the given order in the perturbation series, this scheme is consistent, and it does give the resonant effects required. The calculation was carried out both including and excluding the single resonant diagrams, and with and without a narrow width approximation applied in the phase space sampling. The impact that changing the scheme has on the physics results of this calculation is negligible.

Finally, in proton-proton collisions there are different flavours of quarks which contribute, and there are also gluons which are present in the initial state. For the quark-gluon initiated contribution, all the amplitudes can be obtained from the above ones using crossing symmetry. Quark flavour impacts on the form of the couplings in Eq. (3.12) through the charges Q and T_3, and the electromagnetic charge also affects the ordering of the W bosons in the amplitude A_0^{WW}. A discussion of top and bottom quark contributions to the amplitude is given below.

Real emission

The real emission diagrams involve those with an extra gluon (Fig. 3.4 (a)) and those with two quark lines (Fig. 3.4 (b)-(d)). As can be seen by applying crossing symmetry to these diagrams, new channels for this process open up – the gluon-gluon, quark-quark, and antiquark-antiquark initial state all become possible. The colour structure becomes more involved, but there can be no interference between those amplitudes involving two quark and two gluons and those involving four quarks – we shall proceed

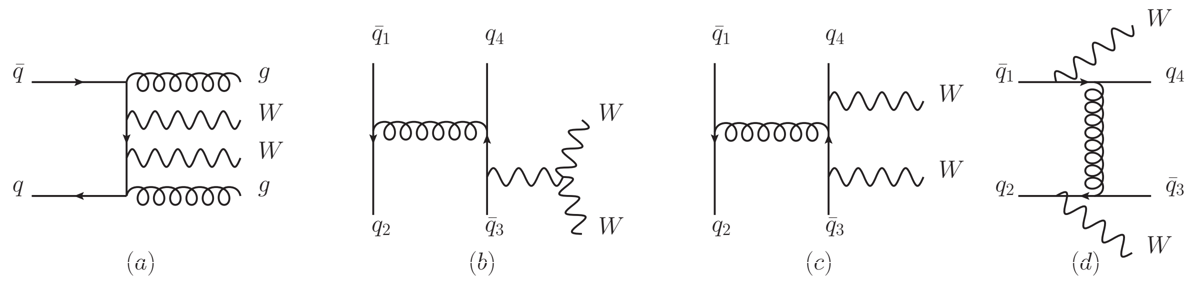

Figure 3.4: Example Feynman diagrams contributing to real emission.

by treating these cases in turn.

The amplitudes for the two-quark two-gluon process can be written as

$$\begin{aligned}\mathcal{A}^{\text{real}}(\bar{q}_1, q_2, g_3, g_4; \nu_\mu, \mu^+, e^-, \bar{\nu}_e) = g_s \left(\frac{g_W}{\sqrt{2}}\right)^4 \times \Big(&(T^{a_3}T^{a_4})_{i_2}^{\bar{i}_1} A_0(\bar{q}_1, q_2, g_3, g_4) \\ &+ (T^{a_4}T^{a_3})_{i_2}^{\bar{i}_1} A_0(\bar{q}_1, q_2, g_4, g_3)\Big)\end{aligned} \tag{3.13}$$

and the colour ordered tree-level amplitudes $A_0(\bar{q}_1, q_2, g_3, g_4)$ and $A_0(\bar{q}_1, q_2, g_4, g_3)$ have exactly the same flavour and helicity decomposition as for the leading order contribution, given by Eq. (3.11), save for an extra gluon in the argument of all amplitudes.

The amplitudes for the four quark process have a more complicated flavour and colour structure. Firstly, there are two possible assignments of quark line, given two external quarks and two external antiquarks – Fig. 3.4 (b) and (c) defines what we call s-channel diagrams, and Fig. 3.4 (d) t-channel diagrams, where quark lines are expressed as $[\bar{q}_1 q_2][\bar{q}_3 q_4]$ and $[\bar{q}_1 q_4][\bar{q}_3 q_2]$ respectively. Which diagrams are present for a given amplitude depends on the flavour assignment of the external quarks. For the s-channel diagrams the colour decomposition reads [8]

$$\begin{aligned}&\mathcal{A}^{\text{real}}(\bar{q}_1, q_2, \bar{q}_3, q_4; \nu_\mu, \mu^+, e^-, \bar{\nu}_e) = \\ &\quad g_s^2 \left(\frac{g_W}{\sqrt{2}}\right)^4 \left(\delta_{\bar{i}_1 i_4}\delta_{\bar{i}_3 i_2} - \frac{1}{N_c}\delta_{\bar{i}_1 i_2}\delta_{\bar{i}_3 i_4}\right) B_0(\bar{q}_1, q_2, \bar{q}_3, q_4)\end{aligned} \tag{3.14}$$

The colour ordered amplitude $B_0(\bar{q}_1, q_2, \bar{q}_3, q_4)$ receives possible contributions (depending on the flavour structure) from two different types of diagrams: *i*) when both Ws are radiated off one quark line, either via an intermediate Z/γ, or directly, as in Fig. 3.4 (*b*) and (*c*) respectively, or *ii*) when each quark line directly emits a W boson, as in Fig. 3.4 (*d*). For type *i*) a similar decomposition holds as has already been written down for the leading order amplitude in Eq. (3.11), that is:

$$\begin{aligned} B_0(\bar{q}_1, q_2, \bar{q}_3, q_4) = &\, B_0^{(WW)}([\bar{q}_1, W, W, q_2], [\bar{q}_3, q_4]) + B_0^{(WW)}([\bar{q}_1, q_2], [\bar{q}_3, W, W, q_4]) \\ &+ C_Z^{(q_2,h_2)} B_0^{(Z)}([\bar{q}_1, Z, q_2], [\bar{q}_3, q_4]) + C_\gamma^{(q_2,h_2)} B_0^{(\gamma)}([\bar{q}_1, \gamma, q_2], [\bar{q}_3, q_4]) \\ &+ C_Z^{(q_4,h_4)} B_0^{(Z)}([\bar{q}_1, q_2], [\bar{q}_3, Z, q_4]) + C_\gamma^{(q_4,h_4)} B_0^{(\gamma)}([\bar{q}_1, q_2], [\bar{q}_3, \gamma, q_4]) \end{aligned} \tag{3.15}$$

where $C_{Z/\gamma}^{(q,h)}$ have already been defined in Eq. (3.12). For type *ii*) contributions, the decomposition is given simply by

$$B_0(\bar{q}_1, q_2, \bar{q}_3, q_4) = B_0^{(WW)}([\bar{q}_1, W, q_2], [\bar{q}_3, W, q_4]) \tag{3.16}$$

where both quarks have to be left-handed, so that only one helicity amplitude is non-zero.

The t-channel diagrams can be obtained from the s-channel diagrams by the swap $q_2 \leftrightarrow q_4$, which includes exchanging colour indices as well.

Virtual

For the one-loop amplitudes, the colour decomposition can be carried out in terms of left primitive amplitudes (defined in App. A, Ref. [31]) – when following the direction of the quark line, it turns to the left when entering the loop, see Fig. 3.5. For this

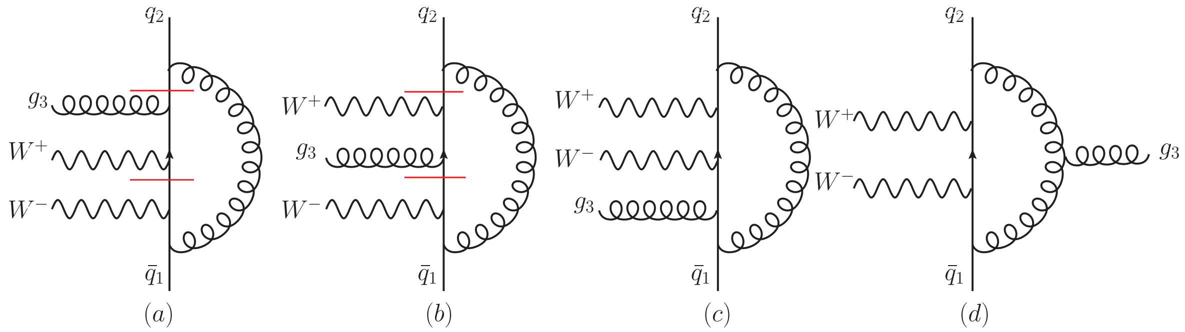

Figure 3.5: Parent Feynman diagrams for the virtual amplitude. The red lines on the first two parent diagrams show a 2-cut which double counts the same contribution – in both cases the Berends-Giele recursion relations return a full tree-level amplitude involving g_3 and W^+ which takes into account both orderings of these particles. One of these 2-cuts must be thrown away.

process the decomposition is given as

$$\begin{aligned}
&\mathcal{A}^{1L}(\bar{q}_1, q_2, g_3; \nu_\mu, \mu^+, e^-, \bar{\nu}_e) = \\
&g_s^3 \left(\frac{g_W}{\sqrt{2}}\right)^4 \times \left[(T^{x_1} T^{a_3} T^{x_1})_{i_2}^{\bar{i}_1} A_1(\bar{q}_1, g_3, q_2) + (T^{x_1} T^{x_2})_{i_2}^{\bar{i}_1} (F^{a_3})_{x_1 x_2} A_1(\bar{q}_1, q_2, g_3) \right],
\end{aligned} \tag{3.17}$$

where $(F^a)_{bc} \equiv i f^{bac}$, and there are two left primitive amplitudes $A_1(\bar{q}_1, g_3, q_2)$ and $A_1(\bar{q}_1, q_2, g_3)$. Feynman diagrams which are illustrative of the cyclic order of these amplitudes and which contain the maximum of propagators are shown in Fig. 3.5 (a) and (d) respectively[4]. Amplitudes which involve a closed fermion loop with Ws attached directly to the fermion loop are neglected – they give a contribution which is four orders of magnitude smaller than the main contributions [18].

The strategy is to consider all possible cuts of each primitive amplitude using the D-dimensional generalised unitarity procedure described in the previous Chapter. The fact that the W bosons are not colour ordered motivates the introduction of *parent diagrams*, which are illustrative diagrams with a maximal number of propagators, one for each possible cyclic ordering of the external particles *including* the

[4]For the purposes of this discussion the W bosons shown in Fig. 3.5 are not important as they do not carry colour charge – diagrams (a), (b) and (c) all have the same colour factor.

W bosons, for a given primitive amplitude. The parent diagrams for $A_1(\bar{q}_1, g_3, q_2)$ are shown in Fig. 3.5 (a)-(c), and the parent diagram for $A_1(\bar{q}_1, q_2, g_3)$ is shown in Fig. 3.5 (d). The strategy for obtaining a full primitive amplitude[5] can then be visualised by adding the contributions from the application of all possible 5-cuts, 4-cuts, etc. to each of the parent diagrams shown in Fig. 3.5. Berends-Giele recursion relations are used to evaluate the resulting products of tree level amplitudes.

This procedure, however, can lead to an over counting of contributions from certain cuts. This happens because, with our prescription for dealing with colourless particles, the Berends-Giele recursion relations return *full* tree-level amplitudes with all possible orderings of the W bosons relative the gluons. An example 2-cut on the parent diagram (b) which is taken into account by a cut on the first parent diagram (a) is shown in Fig. 3.5. For both parent diagrams, a tree-level amplitude involving g_3 and W^+ is evaluated. However, the Berends-Giele recursion relations return both orderings g_3W^+ and W^+g_3 along the quark line. The contribution to this particular 2-cut of the full primitive amplitude coming from parent diagram (b) has already been included by the 2-cut on parent diagram (a), and it should not be counted twice.

A way of identifying all such duplicate contributions is to number in a cyclic order the propagators appearing in the parent diagrams, starting from, for instance, the first propagator moving clockwise away from the antiquark – the 2-cut shown in Fig. 3.5 is then across propagators '2' and '4'. A duplicate contribution can only arise between cuts on different parent diagrams if they involve cutting the same numbered propagators, and only then if the flavour of each of the cut quark propagators in the first parent diagram match the corresponding flavour of those in the second parent diagram. This is because, in this case, each tree-level amplitude in the product of tree-level amplitudes arising from the cut on the first parent diagram can only differ from the corresponding tree-level amplitude coming from the cut on the second parent

[5] That is, the primitive amplitude in terms of the coloured particles, but which includes *all* possible insertions of the colourless particles.

diagram by an ordering of the W bosons along the quark line – the Berends-Giele recursion relations will return the same result for these amplitudes. An automated check on the numbered propagators which are cut, along with their flavour, is easy to implement, and in this fashion the duplicate contributions between parent diagrams can be thrown away.

3.2.4 Top and bottom quarks

There are issues involved with the treatment of the third generation of quarks, as both the bottom and the top quark are massive enough to need careful consideration. Bottom quarks in the initial state are suppressed by the PDFs – there is very little bottom quark content in the proton (the top quark content is non-existent). On the other hand, contributions when bottom quarks in the proton split into a W boson and a top quark can be enhanced because of the top resonance present in this amplitude. Similarly, contributions which involve two $b/\bar{b}$ quarks in the final state receive an enhancement from top quark resonances. However, all of these processes should be seen as contributions to off-shell top (single or pair) production – they lead to a different experimental signature as the b quarks can be tagged in the detector, and this can be considered a different physical process. We will not consider processes with external b quarks in the following. We choose to neglect all contributions from the third generation of quarks, including the case when a gluon splits $g^* \to b\bar{b}$ in both the real and the virtual contributions. The effect of leaving this contribution out is expected to be minimal, as the b quark contribution to the QCD beta function is small.

3.3 Overview of the subtraction formalism

The singular behaviour of all one-loop QCD amplitudes is universal (App. B, [42]), as is the singular behaviour of all tree level amplitudes when partons become soft or collinear [5]. This section addresses the interplay between real and virtual contributions which results in the cancellation of IR divergences for suitably defined observables. A crucial point to make is that the integration over the matrix elements of Eqs. (3.5) and (3.6) is done numerically and separately – the virtual contribution over m particle phase space, and the real over $m+1$ particle phase space (see Eq. (3.3)). The two contributions are separately divergent and their sum is finite only after the integration over phase space is performed. This cancellation of divergences clearly can not be achieved if the two contributions are separately integrated numerically, and this is the problem which the subtraction scheme addresses.

The form of the IR singularities arising from the virtual part of the NLO calculation is analytic. They arise from configurations which involve the loop momentum taking certain values, corresponding to internal particles going soft or collinear with respect to external particles, and the integration of the loop momentum is done analytically, here using dimensional regularisation to evaluate the scalar integrals in Eq. (2.11). As discussed at the beginning of the Chapter, no singularities are allowed to come from configurations of the external particles in particular regions of phase space – the definition of the LO cross section ensures this.

This is in contrast to the origin of the IR singularities in the real cross section, as they come from just such configurations where external particles become soft or collinear to one another. These singularities then are encountered when performing the integral over phase space in Eq. (3.3), as opposed to the singularities from the virtual which are present before the phase space integration is performed.

We follow the CS formalism to deal with the cancellation of divergences. A counter term $\mathrm{d}\sigma^A$ is defined in $(m+1)$ phase space in such a way that it matches the singular structure of the real contribution, $d\sigma^R$, in the phase space $d\Phi_{m+1}$. It is possible to define a general counter term because of the universal behaviour of the singular regions of $d\sigma^R$. It is added and subtracted to the NLO cross section so that it acts to cancel the singularities encountered in the real cross section [5]

$$\sigma^{NLO} = \int_{m+1} [d\sigma^R - d\sigma^A] + \int_{m+1} d\sigma^A + \int_m [d\sigma^V + d\sigma^C] \,. \tag{3.18}$$

The first term on the RHS of Eq. (3.18) is now finite, and can be integrated numerically. The remaining $\int_{m+1} d\sigma^A$ is analytically integrated over a one-particle phase space so that the phase space matches that of the virtual integral – this analytic integration necessarily involves probing the divergent regions of phase space, and has to be regularized, which is done using dimensional regularisation, and the expression has an expansion in $1/\epsilon$. When this is combined with the virtual contribution and the collinear counter term, the poles in ϵ cancel, and the limit $\epsilon \to 0$ can be taken safely. Schematically [5]

$$\sigma^{NLO} = \int_{m+1} \left[d\sigma^R|_{\epsilon=0} - d\sigma^A|_{\epsilon=0} \right] + \int_m \left[d\sigma^V + d\sigma^C + \int_1 d\sigma^A \right] \Bigg|_{\epsilon=0} \,, \tag{3.19}$$

and so the integration in 4 dimensions over both $m+1$ and m particle phase space can now be performed numerically in a Monte Carlo program, as both terms in the big brackets under the integrals are separately finite.

Catani-Seymour dipoles

The authors of Ref. [5] presented a formalism where the counter term is given by a sum over dipoles. In this Section we give a very brief description of these contributions – a full treatment is beyond what can be presented here, and for this the reader is referred to the original reference. In this formalism, in the limit $p_i \cdot p_j \to 0$, where i and j label final state partons, the singular terms of the real matrix element squared appearing in Eq. (3.6) are written as[6]

$$
\begin{aligned}
&{}_{m+1;a,b}\!< 1\,,\ldots,m+1;a,b|\,|1\,,\ldots,m+1;a,b>_{m+1;a,b}\equiv|\mathcal{M}^{m+1}_{ab}(p_a,p_b;p_1,\ldots,p_{m+1})|^2\\
&\to_{\text{(sing.)}}\sum_{k\neq i,j}\mathcal{D}_{ij,\,k}(p_a,p_b;p_1,\ldots,p_{m+1})+\mathcal{D}^a_{ij}(p_a,p_b;p_1,\ldots,p_{m+1})+\mathcal{D}^b_{ij}(p_a,p_b;p_1,\ldots,p_{m+1})\,,
\end{aligned}
\tag{3.20}
$$

where $\mathcal{D}_{ij,\,k}(p_a,p_b;p_1,\ldots,p_{m+1})$ and $\mathcal{D}^{a(b)}_{ij}(p_a,p_b;p_1,\ldots,p_{m+1})$ are dipole contributions which both involve the final state partons i and j, and also one other parton, k or $a(b)$ respectively, k being in the final state and $a(b)$ being in the initial state. These dipoles are given by a colour and helicity correlated (see below) matrix element which involves a final state with one less parton – i and j are replaced by a single *emitter* parton $\widetilde{ij}$ [7], and the parton k or $a(b)$ by a *spectator* parton $\tilde{k}$ or $\tilde{a}(\tilde{b})$ – this is the same parton with momentum shifted in the way described in the example below.

As there are no dipoles $\mathcal{D}_{ij,\,k}$ in the process $pp\to W^+W^-+1j$, we will give some details of the dipole $\mathcal{D}^a_{ij}$. It is given by the formula

$$
\begin{aligned}
&\mathcal{D}^a_{ij}(p_a,p_b;p_1,\ldots,p_{m+1})=-\frac{1}{2p_i\cdot p_j}\,\frac{1}{x_{ij,a}}\\
&\cdot\;{}_{m;a,b}\!<1\,,..,\widetilde{ij},..,m+1;\tilde{a},b|\,\frac{\boldsymbol{T}_a\cdot\boldsymbol{T}_{ij}}{\boldsymbol{T}^2_{ij}}\,\boldsymbol{V}^a_{ij}\,|\,1,..,\widetilde{ij},..,m+1;\tilde{a},b>_{m;a,b}\;.
\end{aligned}
\tag{3.21}
$$

The m particle matrix element on the RHS of Eq. (3.21) is obtained from the $m+1$ matrix element appearing in Eq. (3.20) with the replacement $\{i,j\}\to\widetilde{ij}$ and $a\to\tilde{a}$, and the $\boldsymbol{T}$ and $\boldsymbol{V}^a_{ij}$ are matrices defined in colour and helicity space respectively (App. C) – these provide the non-trivial correlations in order to correctly reproduce the singular limit of the $m+1$ particle matrix element squared. The factor $x_{ij,a}$ is

[6]See App. C for the colour + helicity space vectors used in this Section and in Ref. [5].

[7]If i and j are gluons, or if one is a quark and the other an antiquark, then $\widetilde{ij}$ is a gluon. If one of i or j is a (anti-)quark, the other being a gluon, then $\widetilde{ij}$ is an (anti-)quark.

given by

$$x_{ij,a} = \frac{p_i p_a + p_j p_a - p_i p_j}{(p_i + p_j) p_a}\,, \tag{3.22}$$

and the momentum of the emitter and spectator are given by

$$\tilde{p}_a^\mu = x_{ij,a} p_a^\mu, \quad \tilde{p}_{ij}^\mu = p_i^\mu + p_j^\mu - (1 - x_{ij,a}) p_a^\mu\,, \tag{3.23}$$

which puts both of these partons appearing in the m particle matrix element on-shell and exactly conserves momentum (everywhere, and not just at the singular limit): $p_a - p_i - p_j = \tilde{p}_a - \tilde{p}_{ij}$.

In the limit $p_i \cdot p_a \to 0$, where i is a final state parton and a is an initial state parton, the singular terms of the real matrix element squared are given by

$$\begin{aligned} &{}_{m+1;a,b} < 1\,, \ldots, m+1; a, b|\, |1\,, \ldots, m+1; a, b >_{m+1;a,b} \\ &\to_{\text{(sing.)}} \sum_{k \neq i,j} \mathcal{D}_k^{ai}(p_a, p_b; p_1, \ldots, p_{m+1}) + \mathcal{D}^{ai,\,b}(p_a, p_b; p_1, \ldots, p_{m+1})\,, \end{aligned} \tag{3.24}$$

where the dipoles $\mathcal{D}_k^{ai}(p_a, p_b; p_1, \ldots, p_{m+1})$ and $\mathcal{D}^{ai,\,b}(p_a, p_b; p_1, \ldots, p_{m+1})$ now involve an emitter $\widetilde{ai}$ which is an initial state parton (i.e. a splits into i and $\widetilde{ai}$), and a spectator which is in the final state or the initial state, respectively. In Table 3.1 we list the dipoles which contribute in every singular limit of the real emission contribution to the quark-antiquark channel of the process $pp \to W^+W^- + 1j$, which involves the partonic processes (suppressing the W boson labels) $q_1\bar{q}_2 \to g_3 g_4$ and $q_1\bar{q}_2 \to \bar{q}_3 q_4$.

The analytic integration of these dipoles – which is performed in Ref. [5] – produces the IR singularities which cancel the universal IR singularities of the virtual amplitude $q\bar{q} \to W^+W^- g$ (see App. B) and the IR singularities present in the collinear counter term. All of the two-quark two-gluon ($2q2g$) dipoles in Table 3.1 contain soft singularities; none of the four-quark ($4q$) dipoles Table 3.1 contain soft singular-

Singular Limit	$q_1\bar{q}_2 g_3 g_4$ Dipoles	$q_1\bar{q}_2\bar{q}_3 q_4$ Dipoles
$p_3 \cdot p_4 \to 0$	$\mathcal{D}^{q_1}_{g_3 g_4}$ $\mathcal{D}^{\bar{q}_2}_{g_3 g_4}$	$\mathcal{D}^{q_1}_{\bar{q}_3 q_4}$ $\mathcal{D}^{\bar{q}_2}_{\bar{q}_3 q_4}$
$p_1 \cdot p_3 \to 0$	$\mathcal{D}^{q_1 g_3}_{g_4}$ $\mathcal{D}^{q_1 g_3, \bar{q}_2}$	——
$p_1 \cdot p_4 \to 0$	$\mathcal{D}^{q_1 g_4}_{g_3}$ $\mathcal{D}^{q_1 g_4, \bar{q}_2}$	$\mathcal{D}^{q_1 q_4}_{\bar{q}_3}$ $\mathcal{D}^{q_1 q_4, \bar{q}_2}$
$p_2 \cdot p_3 \to 0$	$\mathcal{D}^{\bar{q}_2 g_3}_{g_4}$ $\mathcal{D}^{\bar{q}_2 g_3, q_1}$	$\mathcal{D}^{\bar{q}_2 \bar{q}_3}_{q_4}$ $\mathcal{D}^{\bar{q}_2 \bar{q}_3, q_1}$
$p_2 \cdot p_4 \to 0$	$\mathcal{D}^{\bar{q}_2 g_4}_{g_3}$ $\mathcal{D}^{\bar{q}_2 g_4, q_1}$	——

Table 3.1: Catani-Seymour dipoles contributing to the $q_1\bar{q}_2$ channel of the process $pp \to W^+W^- + 1j$.

ities. The collinear singularities of the $4q$ and $2q2g$ dipoles which contribute in the limit $p_3 \cdot p_4 \to 0$ cancel the virtual amplitude singularities where the loop momentum is collinear to the gluon. The rest of the $4q$ dipoles only have collinear singularities which cancel with collinear counter term singularities, and the rest of the $2q2g$ dipoles have collinear singularities some of which cancel with the virtual singularities where the loop momentum is collinear to the initial state q or $\bar{q}$ and some of which cancel with collinear counter term singularities.

In the calculations of this thesis, the CS formalism is implemented with the modification suggested in [43, 44]. This modification tests how singular the kinematics are, and a parameter α gives the threshold below which the dipole contribution will be included, and above which it will not. This allows for an optimisation of speed, decreasing the size of the dipole phase space, and it also means there is less chance of incomplete cancellations occurring at the boundaries of histogram bins from differently binned kinematics when plotting distributions of variables. It also provides a powerful check on the dipole implementation as the results should be independent of the α variable.

3.4 Implementation in MCFM and checks

The general MCFM [45] framework is used to organise the calculation, in terms of LO, (real + dipole), and (virtual + dipole) contributions. All of these contributions can be run separately. The inbuilt Monte Carlo generator (which relies on the VEGAS algorithm) is used to perform the integration over phase space. To increase the amount of sampling around the physically important regions of phase space, the generation is built around a tree structure where the resonances are sampled highly in this procedure.

The checks performed on the calculation are as follows. A cross check on all tree-level amplitudes is performed against the public program MADGRAPH [46], which automatically generates tree level amplitudes. In particular, this cross checks the leading order and real contributions. The unitarity procedure to evaluate the virtual matrix element is partially validated by checking the pole structure against the known poles of QCD amplitudes (App. B, [42]). The finite piece of the virtual amplitude is, for this process, cross checked against previous results from independent groups for a particular phase space point [18], and full agreement is found. When such a check is not possible, as is the case for some of the other processes presented in this thesis, a cross check using an independent, home grown program can be performed. This program is a Feynman diagram based program – it takes QGraf [47] input, manipulates the one-loop Feynman integrals in FORM language [48], and then outputs a Fortran code, which takes a phase space point and evaluates the Feynman diagram at this point. The OPP method is applied to evaluate each Feynman diagram systematically (here, the number of propagators in a single Feynman diagram, and the ordering of the particles is explicit – it is not a full amplitude being evaluated).

The dipole implementation can be checked in the real emission contribution by probing all singular regions of phase space and confirming that the dipoles are correctly tending towards and subtracting the singular behaviour of the real matrix element squared. The integrated dipoles are checked by ensuring that all of the poles in ϵ cancel for each phase space point. The finite part of the dipoles can be validated using the implementation of the α parameter by evaluating the NLO cross section at different values of α and checking for independence from this parameter.

Finally, there is an aspect of our implementation which deals with numerical instabilities that can arise in the evaluation of the virtual amplitude at particular phase space points. These phase space points are not necessarily themselves identifiable, so methods need to be in place to test the stability of the virtual amplitude 'on the fly'.

The simplest tests are to compare the poles of the 1-loop amplitude with the analytic expressions – this test is considered failed if the double pole does not agree to within 1 part in 10^6, and for the single pole 1 part in 10^4. Another test for instabilities is to check that the scalar integral coefficients obtained as a solution to the linear system of equations (those solved to find the reduction coefficients, Section 2.1.2) really *do* satisfy the equations for a random value of loop momentum to within an acceptable level of numerical precision.

If either of these two test fail, the whole one-loop amplitude is recomputed in higher computer (quadruple) precision, and then the tests are redone. It was found that for this process, these two tests and subsequent recalculations in quadruple precision were sufficient to obtain numerical stability – only 0.4% of phase space points failed the test initially, and only a tiny fraction of these failed the tests after quadruple precision was used (these points are thrown away). In some of the other processes considered in this thesis, a test on the absolute size of the finite part relative to a characteristic scale of the process was found to be another good indicator of numerical instabilities: unstable points produce an unreasonably large result for the amplitude.

3.5 Simple Results

In this final section, some very simple results are presented – these are not designed to be phenomenological results, rather just to highlight the raw features and benefits of going from a LO to a NLO calculation of a given process. The features seen here are rather generic, and similar results are found in all of the processes considered in this thesis. Results which develop the phenomenology of this process at the LHC are presented in the next Chapter.

The process is considered at the LHC for 8 TeV pp collisions, and minimal kinematic cuts are applied. They are: *i*) both leptons have transverse momenta $p_{T,l} > 20$ GeV and pseudorapidity $|\eta_l| < 2.5$, *ii*) the missing transverse momentum satisfies $p_{T,\text{miss}} > 30$ GeV, and *iii*) jets have transverse momenta $p_{T,j} > 20$ GeV and pseudorapidity $|\eta_j| < 3.2$. The W and Z masses are taken to be $M_W = 80.399\,\text{GeV}$ and $M_Z = 91.188\,\text{GeV}$, and the W and Z widths are taken to be $\Gamma_W = 2.085\,\text{GeV}$ and $\Gamma_Z = 2.4952\,\text{GeV}$. The electroweak gauge coupling is defined through $g_W^2 = 8G_F m_W^2/\sqrt{2}$, with $G_F = 1.166364 \times 10^{-5}$ GeV^{-2}, and the weak mixing angle is given by $\sin^2\theta_w = 1 - m_W^2/m_Z^2$. The parton distributions used are those contained in the MSTW08 set [49] – MSTW08LO for the leading order predictions and MSTW08NLO for the next-to-leading order predictions, corresponding to a strong coupling constant $\alpha_S(M_Z)$ of 0.13939 and 0.12018 respectively. Jets are defined through the anti-$k_\perp$ algorithm [50] with $R = 0.4$, as implemented in FastJet [51].

The top panel of Fig. 3.6 shows the dependence of the LO and NLO total cross sections on the renormalisation and factorisation scales, which are set equal to each other for simplicity, $\mu_R = \mu_F = \mu$. Both inclusive ($\geq$1 jet) and exclusive (1 jet) cross sections are shown at NLO. The LO scale dependence comes mainly from the dependence on renormalisation scale through the running of the coupling α_s, which runs to high values as μ drops. We observe the important feature that at NLO, the scale dependence is reduced: $\sigma^{NLO} = 111.3(2)^{-5.5}_{+4.9}$ whereas $\sigma^{LO} = 87.8(1)^{-10.9}_{+13.5}$.

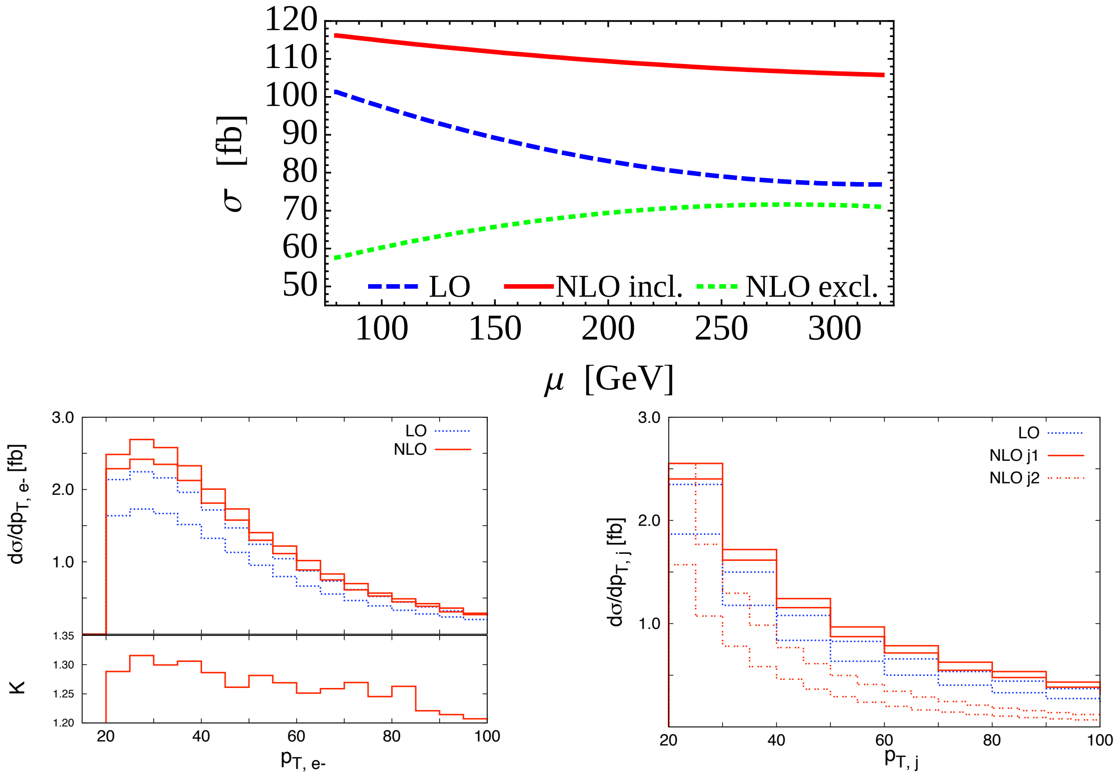

Figure 3.6: Raw features of the NLO calculation of $pp \to W^+W^-j$ compared with the LO calculation, at the 8 TeV LHC. The top panel shows the dependence of the LO, NLO inclusive and NLO exclusive (1 jet) cross section on factorisation (μ_F) and renormalisation (μ_R) scales, which are set equal to each other $\mu = \mu_F = \mu_R$. The bottom two panels show kinematic distributions, as described in the text.

The extra initial state channels that open up in going from LO to NLO obscure this comparison slightly as they boost the size of the NLO cross section to outside the LO scale uncertainty band - the NLO K factor is around 1.3. What is more, these new channels are effectively only getting a LO description, so the scale dependence at NLO may be slightly more than what one might hope for in a calculation of this type. Further into this thesis, the processes where all of the important initial state channels are available at LO show much improved scale dependence behaviour, and the NLO result lies within the LO uncertainty band. The interplay between the real and the virtual contribution can be inferred by seeing the fall of the exclusive cross section at low μ – for the inclusive result, the negative pull of the virtual is becoming compensated by the rise of the real.

Two sample kinematic distributions are also shown in Fig. 3.6. The first plot is of the transverse momentum (p_T) of the negatively charged lepton, and the second plot is of the p_T of the jets in the final state. At NLO there is the possibility of having two hard, clearly separated jets – j_1 corresponds to the jet with the larger p_T, j_2 the softer of the two, if present. Bands are shown with the upper line corresponding to the $\mu = 1m_W$ prediction, the lower line to the $\mu = 4m_W$ prediction. A differential K-factor is defined as $K = \mathrm{d}\sigma_{NLO}/\mathrm{d}\sigma_{LO}|_{\mu=2m_W}$ and is plotted for the lepton p_T distribution.

The reduction in scale dependence is clear in going to NLO (although the scale dependence of the softer jet is 'LO-like', as to be expected since it only feels a LO description). A significant shape change is apparent in the lepton p_T distribution, illustrating that the NLO K-factor is not necessarily spread evenly across phase space. This is interesting from the point of view of experimental methodology – data-driven techniques used to provide an overall normalization for a process to which LO Monte Carlo predictions are applied should be supplemented by theoretical input on NLO shape changes. However, the effect seen in the p_T spectrum of the lepton is partly due to an effect at LO due to the use of a fixed scale, rather than a dynamical one (see e.g. [19]) – using the latter softens the LO high p_T distribution somewhat.

3.6 Chapter Summary

In this Chapter we have summarised a general prescription for putting together the perturbative hard-scattering matrix elements to form an NLO calculation of a process at the LHC. We have used the example of $pp \to W^+W^- + 1j$, describing in detail the leading order, real emission and virtual matrix element contributions to this process, and we presented an overview of the Catani-Seymour dipole formalism that we implement to render the real and virtual contributions separately finite. We discussed the consistency checks that are carried out for the calculations in this thesis, and in the final section we showed results which highlight some raw features that the NLO QCD corrections provide for this process. The set-up and the features of $pp \to W^+W^- + 1j$ displayed in this Chapter are typical of the other NLO calculations in this thesis – for those presented in the next two Chapters we shall focus more on LHC phenomenology, rather than the technical details of the calculations.

Chapter 4

Two Weak Bosons and Higgs Phenomenology at the LHC

Chapter Overview

The search for the neutral, scalar particle which remains in the physical spectrum of particles after electroweak symmetry breaking in the standard model has been ongoing at particle colliders for the past 40 years. It is, then, hugely exciting to be writing this thesis in the weeks after the ATLAS and CMS experiments at CERN announced the discovery of a new resonance, which appears consistent with a standard model Higgs particle of mass $m_H = 125$-$126\,\mathrm{GeV}$. Although tempting, no further discussion of this recent experimental result will be presented here. It remains to be seen over the coming years whether this particle is in fact the standard model Higgs boson or something different – at present the findings are certainly not conclusive. All of the results presented in this Chapter are related to the discovery searches performed and being performed by ATLAS and CMS, and to the important future work of determining the properties of this new particle which will shed light upon its nature.

Previous particle accelerators have only been able to set exclusion limits on the

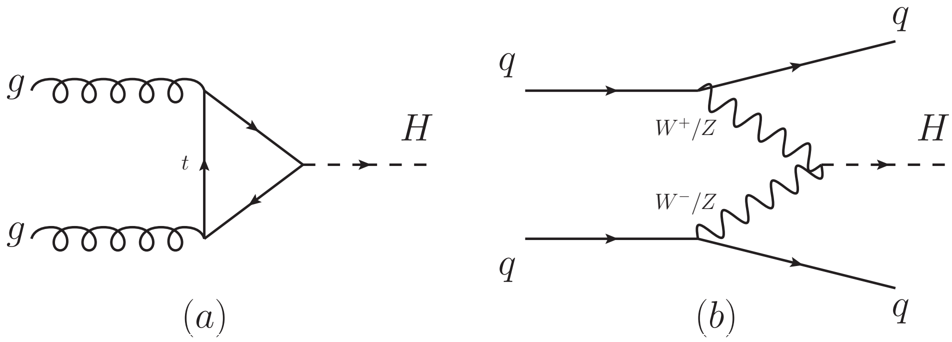

Figure 4.1: Two Higgs boson production mechanisms at the LHC: (a) gluon-gluon fusion (ggF), and (b) weak boson fusion (WBF).

mass of a Higgs boson: the LEP experiment set a bound of $m_H > 114.4\,\mathrm{GeV}$ [52], and the Tevatron is able to place 95% C.L. exclusion limits on a standard model Higgs boson in two mass regions: $100 < m_H < 103\,\mathrm{GeV}$ (already excluded by LEP) and $147 < m_H < 180\,\mathrm{GeV}$ [53], although a $\sim 3.0\sigma$ excess of data events is seen in the mass range $115 < m_H < 140\,\mathrm{GeV}$. It is interesting how different the approaches to Higgs boson searches are at these two colliders. The clean environment of an electron-positron collider allows for a very direct approach to Higgs searches. At LEP, the Higgs boson was looked for in the process $e^+e^- \to Z^{(*)}H \to f\bar{f}H$, with final states such as $\mu^+\mu^-b\bar{b}$ giving extremely clean signatures. Backgrounds do not play a large role in these searches, and this allowed the lower bound on the Higgs mass to be set practically up to the kinematic limit. This is in contrast to the approach that must be taken at hadron colliders – both the Tevatron and the LHC suffer from large QCD backgrounds, and at both, similar strategies are employed for dealing with this problem.

At the LHC, the most important mechanism which can produce a Higgs boson is gluon-gluon fusion (ggF), where the process $gg \to H$ takes place via a top quark loop, as shown in Fig. 4.1 (a). This is a dominant contribution to Higgs production because the gluon flux at the LHC is large (because of the high centre of mass energy of the pp

collisions, a low x region is being probed, where gluon parton distribution functions are dominant). Another important production mechanism which will be of relevance to the work below is that of weak boson fusion (WBF), where the Higgs boson is produced in the process $q\bar{q} \to q\bar{q}H$ via $W^+W^-, ZZ \to H$, as shown in Fig. 4.1 (b). The production of a Higgs in association with a vector boson, $q\bar{q} \to W/Z\, H$, or with a top–anti-top pair, gg, $q\bar{q} \to t\bar{t}H$, have cross sections which are an order of magnitude smaller. All of these production mechanisms involve diagrams where the Higgs boson couples to a particle of significant mass, either a W, Z or t, in order to gain them a large enough cross section to be phenomenologically viable.

The phenomenologically relevant Higgs decay modes also share this feature. At the LHC (and the Tevatron) they are $H \to b\bar{b}$, W^+W^-, ZZ, $\tau^+\tau^-$ and $\gamma\gamma$, where the $\gamma\gamma$ decay mode proceeds via a W/top quark loop. The branching ratios for decay are dependent on the mass of the Higgs boson, but this is far from the only consideration as to which channels can give the most sensitivity to a Higgs signal. An important consideration is the role that the backgrounds play for the different final states. For instance, the relative lack of background to the very rare $\gamma\gamma$ decay mode makes it favourable for light Higgs searches, whereas the similar looking decay into two gluons, a reverse of the production mechanism in Fig. 4.1 (a) (and which has a larger branching ratio) is completely swamped by the QCD production of hadronic jets which is always present at hadron colliders. Leptonic decays of the W, Z or τ are rarer than their hadronic decays, but they too give rise to a final state which gains significance and can compensate for the smaller branching ratio, suffering less from the huge QCD background. The decay $H \to b\bar{b}$ produces two hadronic jets, but the situation can be ameliorated somewhat by using b-tagging to differentiate from the production of light quark QCD jets, and searching for boosted events which are less likely to come from background $b\bar{b}$ production.

An interesting feature of Higgs searches at the LHC, and also the Tevatron, is that events are binned according to the number of jets in the event. This is done because it helps suppress and separate the numerous backgrounds. For example, a Higgs boson produced with a high energy jet will have significant recoil from this jet – its decay products will in turn be more energetic, and this can help with their identification in the detector. What is more, the presence of the hard jet can help to determine the interaction vertex more precisely, and can improve the signal to background ratio, since the majority of the QCD background involves soft hadronic jets. Such effects can compensate for the suppression which comes from the orders of α_S which lower the event rates when additional jets are involved. There are also reasons to study higher jet multiplicity Higgs events which go beyond discovery searches. For instance, angular distributions of jets which are produced in a Higgs event can give information about the CP properties of the Higgs boson [54]. While this jet binning improves experimental analyses, it presents difficulties for theoretical predictions. The exclusivity of looking at a definite number of jets tends to produce a less reliable perturbative result, because the dependency on an extra kinematic scale – the one introduced to define the jet transverse momentum cut-off (see e.g. contributions to [55]).

It is crucial for the Higgs discovery and study (and for all other physics programmes at the LHC) that there is a sound experimental and theoretical understanding of all backgrounds. This Chapter is concerned with the theoretical understanding of QCD WW+jets production, which forms an irreducible background for the case when the Higgs decays as $H \to WW^{(*)}$. This decay mode does not give the highest level of significance for the 125-126 GeV signal seen at the LHC – this comes from the $\gamma\gamma$ and ZZ channels. However, it is an important decay mode for a 125-126 GeV standard model Higgs particle, and it is also the decay mode which allows for the study of the Higgs couplings to W bosons. The signal processes for the ggF mechanism have been calculated (using an effective Lagrangian for the ggH vertex) to NNLO accuracy in the $H + 0j$ bin [56, 57], and to NLO accuracy in the $H + 1j$

[58, 59, 60] and $H + 2j$ bins [29, 61], and the WBF initiated $H + 2j$ process is also known to NLO accuracy in QCD [62, 63]. It is desirable to know the background to the same level of accuracy. Experimental data driven techniques of estimating this background in the signal region are not so well applied for this decay channel when considering the experimentally clean leptonic decay mode due to the presence of two neutrinos in the final state. The kinematic distributions for signal plus background are lacking any resonant region – they are broad distributions – and so theoretical input becomes more important. The original work below consists of making predictions for the $WW + 0j$, $WW + 1j$, and $WW + 2j$ processes. The separate description of these processes is important because of the jet binning of Higgs searches mentioned above.

This Chapter is laid out in two sections, the first considering the $0j$ and $1j$ search bins, and the second the $2j$ search bin. In Sec. 4.1 we consider the $0j$ and $1j$ search bins, with particular attention paid to an NNLO QCD correction coming from gluon fusion, which can form an important contribution to the cross section. We present the first calculation of the gluon fusion contribution to the $1j$ bin. In Sec. 4.2 we focus on the $2j$ bin, and present the calculation of the NLO QCD corrections to the $WW + 2j$ process. In all cases, the focus of this Chapter is on phenomenological results, with less on the technical details of the calculations of the necessary amplitudes. Finally, we summarise the results we find in Sec. 4.3.

4.1 Gluon fusion contribution to the WW background in the $0j$ and $1j$ Higgs search bins

In this section, both the $WW + 0j$ and $WW + 1j$ processes will be considered at the same time and the focus will be on an interesting mechanism which produces these final states. Example diagrams are shown in Fig. 4.2 for both the $0j$ and $1j$ processes.

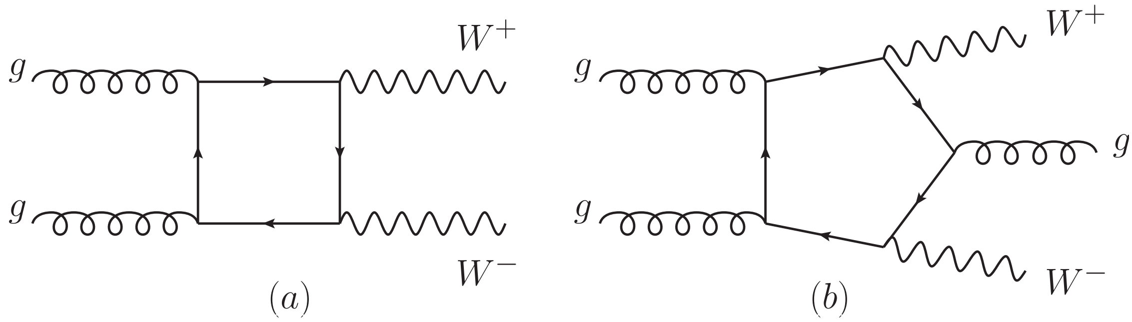

Figure 4.2: Example graphs for gluon fusion contributions to W^+W^- production (a) in the $0j$ bin, and (b) in the $1j$ bin.

These are examples of one-loop amplitudes which cannot contribute to either process at NLO in α_S because there are no corresponding tree-level processes $gg \to WW$ or $gg \to WWg$ with which they can interfere. This mechanism proceeds through the gg initial state which, for the $0j$ process, is an entirely new channel, not present in any part of the LO or the NLO calculation. This situation is analogous to the opening up of new channels in going from LO to NLO, as seen in the previous Chapter, which is often accompanied by a large jump in the cross section, rather than a small correction (within LO uncertainty bounds) expected from a good perturbation series. Here, an increased enhancement is possible because the gluon flux is large at the LHC, so the gg initial state is a particularly important one. There is then motivation to find out just how these gluon fusion diagrams contribute to the cross section.

The diagrams first contribute at NNLO, through their interference with themselves – i.e. virtual-virtual interference – and for each process they form a subset of the total NNLO contributions which is both finite and gauge invariant. This means that these contributions can be considered on their own. The calculation of the $0j$ gluon fusion diagrams was first presented in Ref. [6], and was supplemented in Ref. [7] with the inclusion of the massive third generation quarks in the fermion loop, which were neglected in the original paper. In these papers, a phenomenological study at the LHC was undertaken, the results of which are discussed in greater detail below. The gluon fusion contributions were found to correct the NLO cross section at a level of 5% for generic LHC cuts growing to a level of 30% for cuts applied for Higgs boson searches. These numbers are *a priori* not predictable – in the absence of an explicit calculation, there is no real argument as to what their size will be – and the 30% correction found in Ref. [6, 7] is a very significant one.

It is natural to ask whether the effect of gluon fusion contributions to the $WW+1j$ process are as significant as they are in the $WW+0j$ process. Again, there is no argument to suggest whether they are or not, but there could be an expectation that they would play a similar role. On the other hand, this time the gg initial state has already appeared in the real emission part of the NLO cross section for the $1j$ process, and so it is possible that the relative contribution from the gluon fusion NNLO corrections could be diminished somewhat. The original work laid out below is the explicit calculation of the gluon fusion contributions to the $WW+1j$ process. There are also new results presented which involve revisiting the phenomenology of the $0j$ process, and adding to some of the conclusions made in Refs. [6, 7].

4.1.1 Theoretical set-up

The NLO calculation of the $WW+0j$ process is readily available for use in the public program MCFM [64], as are the NNLO gluon fusion contributions [65]. The implementation of the gluon fusion diagrams in MCFM includes the contribution from massive quarks in the third generation. This contribution is small, but non-negligible[1]. MCFM is used to generate all of the results for the $WW+0j$ process.

A description of the calculation of the NLO corrections to the $WW+1j$ process has already been presented in detail in the previous Chapter of this thesis, and the publicly released code [38] is the one which is used to obtain the results in this section. For the gluon fusion contribution to the $1j$ process, the one-loop amplitude was

[1]The effect of the third generation is shown to become important in certain scenarios [65]

obtained using the same technique of D-dimensional generalised unitarity described in Chapter 2.

The one-loop amplitude for $0 \to gggW^+(\to \nu_e e^+)W^-(\to \mu^- \bar{\nu}_\mu)$ has the following colour decomposition

$$\begin{aligned}\mathcal{A}_f^1(g_1, g_2, g_3; \nu_e, e^+, \mu^-, \bar{\nu}_\mu) = g_s^3 \left(\frac{g_W}{\sqrt{2}}\right)^4 \times \\ \Big(\mathrm{Tr}\big(T^{a_1}T^{a_2}T^{a_3}\big)A_f(g_1, g_2, g_3) + \mathrm{Tr}\big(T^{a_1}T^{a_3}T^{a_2}\big)A_f(g_1, g_3, g_2)\Big)\,,\end{aligned} \tag{4.1}$$

where factors of the strong and weak coupling constants have been taken out, and the colour ordered amplitudes $A_f(g_1, g_2, g_3)$ and $A_f(g_1, g_3, g_2)$ differ in their ordering of the gluons around the fermion loop. Just as outlined in the previous Chapter, the colourless weak bosons are not ordered in such a decomposition and so for D-dimensional generalised unitarity to be applied, further decomposition must be made – this is discussed shortly.

The amplitudes have contributions coming from the first two light generations of quarks, and a third generation of heavy bottom and top quarks

$$A_f = 2A_{f,0} + A_{f,m}\,, \tag{4.2}$$

and have an analogous breakdown to Eq. (3.11)

$$\begin{aligned} A_{f,0} &= A_{f,ud}^{[WW]} + \sum_{q\in\{u,d\}} \left(C_{V,q}^{[Z]}A_{f,q}^{[Z_V]} + C_{A,q}^{[Z]}A_{f,q}^{[Z_A]} + C_q^\gamma A_{f,q}^{[\gamma]}\right)\,, \\ A_{f,m} &= A_{f,tb}^{[WW]} + \sum_{q\in\{t,b\}} \left(C_{V,q}^{[Z]}A_{f,q}^{[Z_V]} + C_{A,q}^{[Z]}A_{f,q}^{[Z_A]} + C_q^\gamma A_{f,q}^{[\gamma]}\right)\,. \end{aligned} \tag{4.3}$$

Here, the first term on the right hand side denotes contributions where the Ws couple directly to the fermion loop, and the remaining terms those where they couple via an intermediate Z or γ. A slight difference to Eqs. (3.11) and (3.12) is that now the vector and axial parts of the Z boson's coupling to the quark loop have been separated. This is because previously there had been an external quark line with fixed helicity which, because the quarks are massless, determined the chirality of the quark line, which in turn determined the form of the Z coupling (see Eq. (3.12)). Here, all quarks are internal and both left and right handed quarks are summed over in the loop. The couplings are $C_{V,q}^{[Z]} = T_q^3 - 2Q_q \sin^2\theta_W$, $C_{A,q}^{[Z]} = -T_q^3$, and $C_q^{[\gamma]} = 2Q_q \sin^2\theta_W$, where Q_q is the electromagnetic charge of the quark in the loop, θ_W is the weak mixing angle, and $T^3_{u,c,t} = 1/2, T^3_{d,s,b} = -1/2$.

To return to the discussion of the ordering of colourless weak bosons, it should be clear that the situation here is exactly the same as that discussed in the context of the calculation of one-loop amplitudes for the NLO corrections to $pp \to W^+W^-j$. The aim is simply to include all possible cuts of each colour ordered amplitude during the OPP procedure – this involves taking into account all possible insertions of W bosons relative to the three gluons, and being careful not to double count contributions when using recursion relations to evaluate the tree-level amplitudes. For instance, consider the amplitude $A_{f,ud}^{[WW]}$. There are twelve possible insertions of the W^+W^- pair relative to the three colour ordered gluons. Each of these has to be considered as a separate parent diagram, and the union of all possible cuts applied to all of the parent diagrams is what is required, throwing away contributions which double count cuts arising from other parent diagrams.

The number of repeated cuts which have to be thrown away is large, owing to the cyclic nature of the fermion loop being considered. On top of this, the method outlined in the previous chapter of using the propagator flavour to identify repeated cuts does not take into account cases where cuts are identical through a cyclic permutation. To deal with this additional problem, it was found easiest to employ a strategy in which the Berends-Giele recursion relations are modified in a way so as to artificially fix the position of one gluon relative to the Ws in the recursion relation – that is *not* to consider all possible insertions of the Ws at every stage of recursion. Conceptually, this has a downside in that it is not strictly a full tree-level amplitude being calculated when such recursions are used. However, it correctly accounts for all of the required cuts, which in turn ensures that the OPP procedure produces the correct, full, one-loop amplitude. That it does this is checked by an independent calculation explicitly using Feynman diagrams – this is the same home-grown program as described in the previous Chapter.

The following parameters are used for this calculation: the W and Z bosons have masses $M_W = 80.399\,\mathrm{GeV}$ and $M_Z = 91.188\,\mathrm{GeV}$, and widths $\Gamma_W = 2.085\,\mathrm{GeV}$ and $\Gamma_Z = 2.4952\,\mathrm{GeV}$, respectively. The top quark mass is set to $M_t = 172.9\,\mathrm{GeV}$, and the bottom quark mass to $M_b = 4.72\,\mathrm{GeV}$. We take $G_F = 1.166364 \times 10^{-5}$ GeV^{-2}, where G_F is the Fermi constant, with the weak coupling is defined through $g_W^2 = 8 G_F m_W^2/\sqrt{2}$; the weak mixing angle is given by $\sin^2\theta_w = 1 - m_W^2/m_Z^2$. All first and second generation quarks are taken to be massless. The parton distributions used are those contained in the MSTW08 set, which includes leading, next-to-leading and next-to-next-to-leading distribution functions. The parton distribution used below is in correspondence to whether the matrix element being evaluated is LO, NLO or NNLO[2]. Jets are defined through the anti-$k_\perp$ algorithm with $R = 0.4$, as implemented in FastJet.

4.1.2 LHC predictions

This section presents theoretical results for the $WW + 0j$ and $WW + 1j$ backgrounds to Higgs production at the LHC, at LO and at NLO in QCD, and investigates the effects of the gluon fusion NNLO contribution to both processes. In these jet bins, Higgs production is overwhelmingly coming from the ggF production mechanism at

[2]In the absence of a full NNLO calculation it is possible that the gluon-gluon contribution to the cross section is underestimated when using NNLO PDFs. If LO PDFs are used for the gluon fusion contribution considered here, a result for the partial NNLO correction which is around 30% larger is obtained. However, in the following, NNLO PDFs are used, as that is what would be used when the full NNLO calculation becomes available.

the LHC. In the following, two different sets of cuts are applied. The first 'generic cuts' are typical for the observation of weak boson pair production at the LHC, and provide a reference point for the subsequent phenomenology. The second set of cuts are 'Higgs search cuts', and these make contact with those used by detector collaborations in Higgs boson search analyses. This set of cuts is inspired by those made by ATLAS, although they are a slightly simplified version of what is described in [66][3]. The Higgs search cuts are of course designed to reduce the WW background process in favour of the Higgs signal. The two sets of cuts are:

Generic cuts: *i*) both leptons have transverse momenta $p_{T,l} > 20$ GeV and pseudorapidity $|\eta_l| < 2.5$, *ii*) the missing transverse momentum satisfies $p_{T,\mathrm{miss}} > 30$ GeV, and *iii*) jets have transverse momenta $p_{T,j} > 20$ GeV and pseudorapidity $|\eta_j| < 3.2$.

Higgs search cuts: *i*) the hardest lepton has $p_{T,l,\max} > 25$ GeV, the softest lepton has $p_{T,l,\min} > 15$ GeV, *ii*) the lepton rapidities are $|\eta_l| < 2.5$, *iii*) the relative azimuthal angle between the two leptons is small $\Delta\phi_{ll} < 1.8$, *iv*) the two leptons are separated from each other by $\Delta R_{ll} = \sqrt{\Delta\phi_{ll}^2 + \Delta\eta_{ll}^2} > 0.3$, *v*) the invariant mass of the charged lepton system must satisfy 10 GeV $< m_{ll} <$ 50 GeV, *vi*) the missing relative transverse energy[4] satisfies $E_{T,\mathrm{rel}}^{\mathrm{miss}} > 25\,\mathrm{GeV}$, and *vii*) jets have $p_{T,j} > 25$ GeV and pseudorapidity $|\eta_j| < 4.5$. Additionally, for the $0j$ process the charged lepton system must have a transverse momentum $p_{T,ll} > 30$ GeV.

The extra cuts on $\Delta\phi_{ll}$, m_{ll} and $p_{T,ll}$ (for the $0j$ process) in the 'Higgs search cuts' serve to improve the signal to background ratio in the $H \to WW$ channel. A major consideration is that the spin correlations between leptons are different

[3]The ATLAS collaboration excludes the rapidity region $1.37 < |\eta| < 1.52$ for electrons. In the following, full acceptance is used for both for electrons and muons. Any issues related to the specifics of the ATLAS detector are also ignored. The treatment of lepton separation is also somewhat simplified here.

[4]This quantity is defined as $E_{T,\mathrm{rel}}^{\mathrm{miss}} = |\mathbf{p}_T^{\mathrm{miss}}| \sin\Delta\phi_{\min}$, where $\Delta\phi_{\min} = \min\big(\Delta\phi_{\mathrm{miss}}, \pi/2\big)$ and $\Delta\phi_{\mathrm{miss}}$ is the azimuthal angle between the missing transverse momentum vector $\mathbf{p}_T^{\mathrm{miss}}$ and the momentum of the nearest charged lepton or jet with $p_T > 25$ GeV.

for the signal and background processes. Leptons coming from $H \to WW$ prefer to have a small opening angle, compared with those from background WW, where the distribution peaks at maximum opening azimuthal angle. The $\Delta\phi_{ll}$ cut clearly exploits this feature, but the m_{ll} cut also picks up on it, since m_{ll} is sensitive to the angle between the leptons' direction[5]. The $p_{T,ll}$ cut also relies on the leptons coming from the signal process to be travelling in the same transverse direction more often. In fact, a rather interesting characteristic of the phenomenology surrounding $pp \to WW$+jets is just how intertwined the different phase space projections are with each other. The conclusions drawn from the following will be found to be highly cut dependent, and it will not be one particular cut which is clearly influencing the results.

As a final remark on the role that the choice of cuts plays in reducing the WW background for Higgs searches, it is worth pointing out that because the NNLO gluon fusion contribution proceeds through the same gg initial state as the signal (as opposed to all or almost all of the LO and NLO contributions to the $WW + 0j$ or $WW + 1j$ processes), it could be that it is relatively less affected by Higgs search cuts. That is that the cuts may be exploiting features of the signal that are a result of proceeding through a gg initial state at the LHC. For instance, the background WW system is generally quite longitudinally boosted, as pointed out in Ref. [67]. This is because a large fraction of the cross section comes from initial states which involve a quark annihilating with an antiquark or a gluon. The form of the PDFs means that the quark will tend to be valence-like, carrying a larger momentum fraction of the proton, x, whereas the antiquark or gluon comes from the sea and has smaller x, which provides the momentum imbalance. In contrast, the Higgs signal process $gg \to H$ has a longitudinal boost peaked around zero. If cuts exploit this feature at some level in order to boost signal to background ratio, then they will increase the relative

[5]The m_{ll} cut also serves to reduce the γ/Z background to the signal process.

importance of the gluon fusion $gg \to WW$ contribution to the background, which also has a boost peaked at zero. However, there is generally considerable interplay between the different factors which become important when cuts are changed or new cuts are introduced, and often it is only an explicit calculation which can determine the overall outcome. The change from the 'generic cuts' to the 'Higgs search cuts' given above is just such an example of a connected case. However, the kind of considerations just outlined give an insight into what distributions (and what cuts on these distributions) can be useful for a given phenomenological scenario – this is a subject which will be returned to in the final section of Chapter 5 in this thesis.

Results

Tables 4.1 and 4.2 display the values of the cross sections for the $0j$ and the $1j$ processes, for two different energies of LHC collisions – 8TeV and 14TeV – and under the two different sets of cuts described above, Table 4.1 containing the 'generic cuts' results and Table 4.2 containing the 'Higgs search cuts' results. The leading order cross section, σ_{LO}, the inclusive and exclusive next-to-leading order cross sections, $\sigma_{\mathrm{NLO}}^{\mathrm{incl}}$ and $\sigma_{\mathrm{NLO}}^{\mathrm{excl}}$, and the gluon fusion contribution, $\delta\sigma_{\mathrm{NNLO}}$, are all displayed.

Focusing first on the generic cuts, similar results are found for the 0-jet bin as were found in Ref [6, 7]. The gluon fusion contribution increases the inclusive cross section by $\sim 3\%$ at 8 TeV, and this number grows to $\sim 5\%$ at 14 TeV. The increase in the relative importance of this contribution at higher LHC energies is expected because the gluon flux grows rapidly at small $x \sim m_{WW}/\sqrt{s}$. The first results for gluon fusion in the $1j$ bin are found to be in accordance with the expectations outlined above – the contribution is of a similar magnitude, but is slightly smaller than in the $0j$ bin. The scale dependencies of the cross sections are also shown in Table 4.1 where factorisation and renormalisation scales are set equal to each other $\mu_R = \mu_F = \mu$, and varied as $m_W < \mu < 4m_W$. The gluon fusion contributions are as large as the scale

Generic Cuts

		σ_{LO}	$\sigma^{\mathrm{incl}}_{\mathrm{NLO}}$	$\sigma^{\mathrm{excl}}_{\mathrm{NLO}}$	$\delta\sigma_{\mathrm{NNLO}}$	$\delta\sigma_{\mathrm{NNLO}}/\sigma^{\mathrm{incl}}_{\mathrm{NLO}}$
8 TeV	WW	$141.0(1)^{+2.8}_{-4.0}$	$232.0(4)^{-5.8}_{+7.5}$	$143.8(2)^{+4.2}_{-4.1}$	$8.1(1)^{-1.7}_{+2.2}$	3.5%
	WWj	$87.8(1)^{-10.9}_{+13.5}$	$111.3(2)^{-5.5}_{+4.9}$	$66.6(2)^{+4.4}_{-9.0}$	$3.4(1)^{-1.0}_{+1.6}$	3.1%
14 TeV	WW	$259.6(2)^{+14.2}_{-17.2}$	$448.3(5)^{-7.4}_{+11.6}$	$242.0(3)^{+9.2}_{-8.6}$	$23.6(1)^{-4.1}_{+5.2}$	5.3%
	WWj	$203.4(1)^{-19.9}_{+22.9}$	$254.5(4)^{-10.2}_{+9.0}$	$127.6(4)^{+14.8}_{-24.1}$	$11.8(4)^{-3.2}_{+4.7}$	4.6%

Table 4.1: Cross-sections for $pp \to W^+(\nu_e e^+)W^-(\mu^-\bar{\nu}_\mu) + n$ jets, $n = 0, 1$ at the $\sqrt{s} = 8$ TeV and $\sqrt{s} = 14$ TeV LHC, using the 'generic cuts' described in the text. All cross-section values are in femtobarns. The central values are computed with factorisation and renormalisation scales $\mu = 2m_W$, with the statistical error shown in parentheses. The upper and lower values for cross-sections are obtained with the choice of scale $\mu = m_W$ (subscript) and $\mu = 4m_W$ (superscript). The last column shows the relative size of the NNLO contribution and the *inclusive* NLO cross-section for the central scale choice.

Higgs search cuts

		σ_{LO}	$\sigma^{\mathrm{incl}}_{\mathrm{NLO}}$	$\sigma^{\mathrm{excl}}_{\mathrm{NLO}}$	$\delta\sigma_{\mathrm{NNLO}}$	$\delta\sigma_{\mathrm{NNLO}}/\sigma^{\mathrm{excl}}_{\mathrm{NLO}}$
8 TeV	WW	$35.6(1)^{+0.9}_{-1.3}$	$51.1(1)^{-0.4}_{+0.9}$	$38.8(1)^{+1.0}_{-0.8}$	$2.7(1)^{-0.5}_{+0.7}$	7.0%
	WWj	$12.6(1)^{-1.5}_{+1.8}$	$10.8(1)^{+0.3}_{-0.7}$	$10.6(1)^{+0.3}_{-0.9}$	$0.6(1)^{-0.2}_{+0.2}$	5.7%
14 TeV	WW	$63.4(1)^{+3.9}_{-4.7}$	$91.9(2)^{-0.1}_{+0.4}$	$63.4(2)^{+2.1}_{-2.0}$	$7.5(1)^{-1.2}_{+1.5}$	11.8%
	WWj	$28.7(1)^{-2.6}_{+2.9}$	$21.6(1)^{+1.2}_{-2.1}$	$20.5(1)^{+1.7}_{-2.2}$	$1.8(2)^{-0.5}_{+0.7}$	8.8%

Table 4.2: As for Table 4.1, but using the 'Higgs search cuts' described in the text. The ratio in the last column is taken using the *exclusive* NLO cross-section.

uncertainties on the NLO cross section[6]. Finally, for these cuts, the size of the NLO corrections to the LO cross section are very large. This has already been seen in the previous Chapter for the $1j$ process – here again the corrections are $\mathcal{O}(15\% - 25\%)$ of the LO result. The situation is even more dramatic for the $0j$ process, where the NLO corrections are $\mathcal{O}(65\% - 70\%)$. As already discussed, these huge increases are attributed to the opening up of new initial state channels – the size of the corrections are larger in the $0j$ case as the quark-gluon initial state channel opens up for the first time.

Turning now to the cross sections for the 'Higgs search cuts', it is found that

[6]The scale dependences on the NNLO ggF part were calculated using NNLO PDFs, and do not on their own give a scale variation which would be expected from the full NNLO calculation.

the relative importance of the gluon fusion contribution to both the $0j$ and the $1j$ processes increases. For Higgs searches with jet binning, it is the exclusive cross sections which are of interest – NNLO gluon fusion increases the exclusive NLO cross section for the $0j$ process by $\sim 7\%/12\%$ at $8\,\text{TeV}/14\,\text{TeV}$, and for the $1j$ process by $\sim 6\%/9\%$. As for the 'generic cuts', the $gg \to WW$ mechanism is slightly less important for the $1j$ process than for the $0j$ process. In moving to the 'Higgs search cuts', the relative contribution from gluon fusion has increased by about a factor of two, but it should be kept in mind that this is in part attributed to the change in interest from the inclusive cross section to the exclusive cross section. The NLO corrections to the LO cross section are seen to be significantly smaller in the region of phase space allowed by these cuts, and the differences between the inclusive and exclusive NLO cross sections are smaller too. Again, the $\delta\sigma_{\text{NNLO}}$ contributions are as large as the scale uncertainties on the NLO cross section – in fact for the $0j$ process they are larger.

The results for the $0j$ process should be compared to those found in Refs. [6, 7], which reported the $\mathcal{O}(30\%)$ corrections to the NLO $WW + 0j$ cross section coming from the NNLO gluon fusion contribution. The Higgs search cuts employed in Ref. [6, 7] are more aggressive than those used above – in particular $\Delta\phi_{ll} < 0.79$, $m_{ll} < 35\,\text{GeV}$, $p_{T,l,\max} > 35\,\text{GeV}$ and $p_{T,l,\min} > 25\,\text{GeV}$ – and they reduce the size of the NLO cross section to $\sim 4.8\,\text{fb}$. Under these stricter cuts the gluon fusion contribution significantly increases in importance relative to the rest of the cross section. A detailed study in which the 'Higgs search cuts' used above are slowly changed to the cuts of Ref. [6, 7] reveals that it is mainly a combination of the ϕ_{ll}, m_{ll} and $p_{T,l}$ cuts which causes this effect, and not the effect of one particular cut by itself. A conclusion that can be drawn from this work is that the $gg \to WW$ mechanism produces contributions which are strongly cut dependent and the dependency is not easily identified, so that if new cuts are proposed for a study, then the theoretical analysis should be redone.

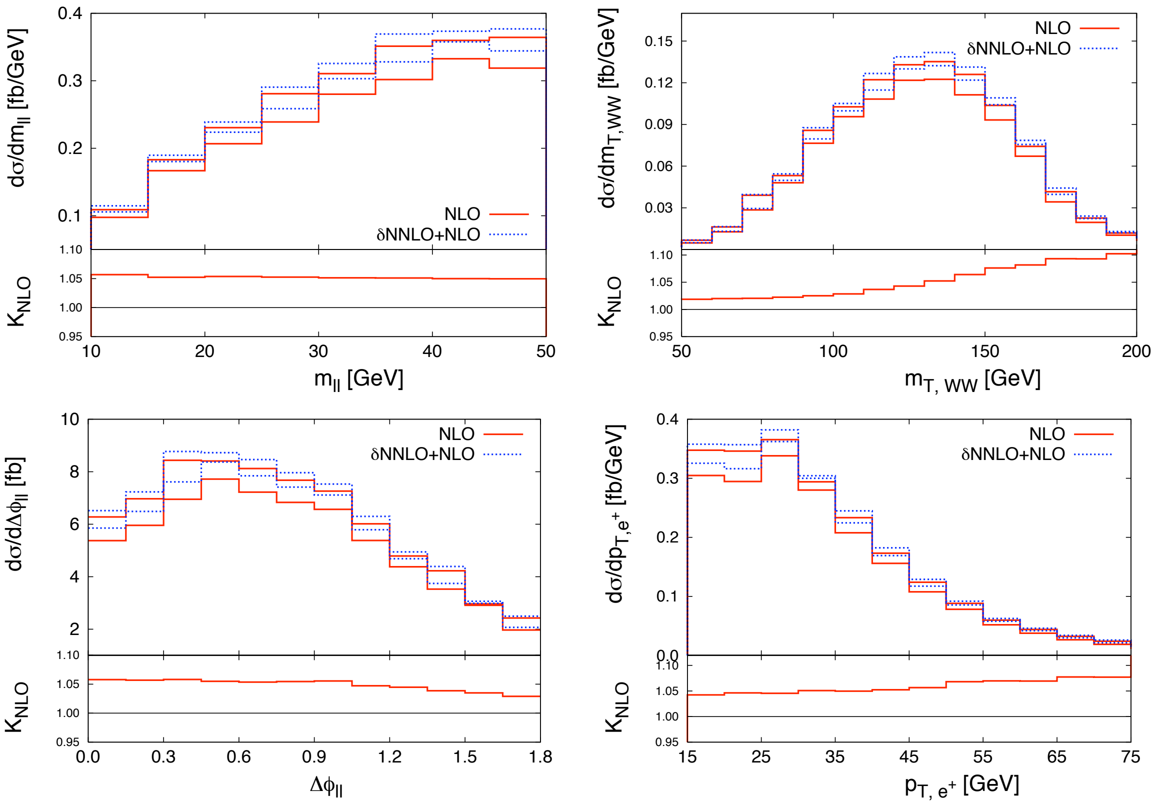

Figure 4.3: $WW + 1j$ distributions of the mass of the charged lepton system m_{ll}, transverse mass of the W-pair $m_{T,WW}$, the azimuthal angle between the leptons $\Delta\phi_{ll}$ and the transverse momentum of the positron p_{T,e^+}, shown at NLO accuracy with and without the fermion loop NNLO contribution. The Higgs search cuts are used, as described in the text, and results are displayed for the 8 TeV LHC. The upper and lower bands show the maximum and minimum deviations from the central scale value $2m_W$. The ratio K_{NLO} as defined in Sec. 3.5 is also displayed.

Turning back to the new results for the $WW+1j$ process, the shapes of distributions should also be considered. These are important experimentally – for instance, ATLAS uses the distribution of the variable $m_{T,WW}$ when searching for the presence of a Higgs signal, where $m_{T,WW}$ is defined as

$$m_{T,WW} = \sqrt{(E_{T,ll} + p_{T,\text{miss}})^2 - |\mathbf{p}_{T,ll} + \mathbf{p}_{T,\text{miss}}|^2}\,, \tag{4.4}$$

with $E_{T,ll} = \sqrt{|\mathbf{p}_{T,ll}|^2 + m_{ll}^2}$ and $p_{T,\text{miss}} = |\mathbf{p}_{T,\text{miss}}|$. Restricting this variable to values around the Higgs mass[7] helps to reduce the WW background and also to exclude regions of phase space where there is significant interference between the signal and the gluon fusion $gg \to WW$ contribution to the background that is being considered here [65].

This distribution is plotted for the $WW+1j$ process in Fig. 4.3, which also displays the differential K-factor, defined as

$$K_{\mathrm{NLO}} = \left.\frac{\mathrm{d}\sigma_{\mathrm{NLO}+\delta\mathrm{NNLO}}}{\mathrm{d}\sigma_{\mathrm{NLO}}}\right|_{\mu=2m_W} . \tag{4.5}$$

The distributions of ϕ_{ll}, m_{ll} and p_{T,e^+} for the $WW+1j$ process, along with their differential K-factors are also shown in Fig. 4.3. The K-factor for the $m_{T,WW}$ distribution is far from flat, showing that the relative importance of the gluon fusion contribution increases with $m_{T,WW}$. In contrast, the K-factors for ϕ_{ll}, m_{ll} and p_{T,e^+} are reasonably flat across the distributions, although the gluon fusion contribution shows more favour for smaller ϕ_{ll} and m_{ll} and for higher p_{T,e^+} than the NLO cross section.

Finally, the size of this background should be compared to that of the signal process $H \to WW$ under the 'Higgs search cuts'. For a Higgs of mass 125 GeV the cross section is ~ 5 fb (~ 12 fb) at 8 TeV (14 TeV) in the 0-jet bin, and ~ 2 fb (~ 5 fb) at 8 TeV (14 TeV) for the 1-jet process. The non-resonant WW background has a significantly larger cross section than the signal, and the gluon fusion $gg \to WW$ process alone contributes an amount of around half of the signal. This, along with its size compared to the NLO scale uncertainties, highlights the importance of this part of the NNLO calculation, which can become even more important under certain cuts.

[7] A cut of $0.75 m_H < m_{T,WW} < m_H$ is employed by the ATLAS collaboration in Ref. [66] (when the Higgs boson has a mass $m_H < 220$ GeV).

4.2 NLO QCD corrections to the W^+W^-+2j background in the $2j$ Higgs search bin

In this section the focus now turns to the $H \to WW$ search at the LHC in the $2j$ bin and to a description of the calculation of the NLO QCD corrections to the irreducible background process $pp \to WW + 2j$.

When searching for a Higgs boson in the 2-jet bin, the WBF production mechanism also becomes important since $qq \to Hqq$ contains two jets in the final state. The ggF mechanism is still of relevance, where $gg \to H$ occurs with two extra jets being radiated in the process. The 2-jet bin provides some sensitivity to a Higgs boson discovery – in particular, the two jets which come with the WBF mechanism are experimentally looked for and 'tagged', which helps to gain some background suppression. However, the 2-jet bin is mostly important because it is a window for studying Higgs boson properties – these are vital experimental measurements which will determine the nature of the particle. It is interesting that different aspects of Higgs boson properties are probed by the two different production mechanisms. Firstly, through the WBF mechanism, the strength of the couplings of the Higgs boson to the W and Z bosons can be tested, as WBF proceeds through either $WW \to H$ or $ZZ \to H$. Secondly, information can come from the ggF mechanism about the coupling of the Higgs to the top quark (present in the loop $gg \to H$) – the CP properties of the coupling can be elucidated by studying angular distributions of the two final state jets. A feature of the WBF mechanism is that the two jets are produced in the forward region of the detector, and they are widely separated in rapidity from each other (i.e. one jet in each direction). This is in contrast to jets radiated from the ggF process – these tend to be much more central. This allows for a separation of $H + 2j$ events into those most likely to come from WBF, and those most likely to come from ggF, and this is particularly useful when the different properties of the Higgs are being studied.

This section will again be concerned with an irreducible background to the $H \rightarrow WW$ decay mode – the QCD production $pp \rightarrow WW + 2j$. Prior to the completion of the work in Ref. [9] that we present here, this process was only known at LO. It has a larger cross section than the signal and is the dominant background, so it is clearly important to understand it theoretically and experimentally. The jets produced by this background have a very similar distribution to those coming from the ggF mechanism – they are central in the detector – and this is why this QCD background can be suppressed well with cuts which only allow forward jets typical of WBF Higgs production. Suppression of the background process to the ggF produced Higgs signal can be achieved in the same way as in the last Section of this thesis – the leptons in the final state have different distributions owing to the different spin correlations depending on whether the Ws are produced via a scalar particle or not. Below, the calculation of the NLO QCD corrections to the $WW + 2j$ background is presented, and particular emphasis is given to the effect that these corrections have on the distributions relevant for Higgs phenomenology.

Again, there is considerable motivation for knowing this process beyond LO in α_S. The QCD corrections to the signal process $H + 2j$ are already known (using an effective coupling for the ggH vertex), and it is desirable to know the background at the same order. The fact that the computation of the $WW + 2j$ process involves an additional particle in the amplitudes complicates it considerably relative to that of the signal process. There is also the theoretical motivation of being able to demonstrate the new techniques outlined in Chapter 2 can be applied to such complicated final states, and in particular to show they can be developed to deal with the two colourless particles present in these amplitudes. What is more, the NLO corrections to the $0j$ and $1j$ processes have been seen to be large, so it is important to know if the same is true for the $2j$ process. The calculation described below was the first calculation of these NLO QCD corrections – the results have since been verified by an independent calculation in Ref. [68].

4.2.1 Theoretical set-up

This NLO calculation follows very closely the one of $pp \to WW+1j$ outlined in detail in Chapter 3 – the virtual corrections are calculated using D-dimensional generalised unitarity, with QCDloop used to evaluate scalar integrals; all tree-level amplitudes are calculated using Berends-Giele recursion relations; the Catani-Seymour dipole formalism with the α parameter modification provides the subtraction terms; the full calculation is embedded within the MCFM framework; and all of the same checks on the calculation are carried out as described previously, as is the implementation of quadruple precision to improve numerical stability. The technical details presented here will be those where a notable difference arises in the set-up of the calculation.

Leading order

The leading order contributions to this process are just the real emission corrections to the $pp \to WW + 1j$ process – there are contributions involving two gluons and two quarks, as well as contributions involving four quarks (see Fig. 3.4). The colour decompositions have been already given in Eqs. (3.13) and (3.14). All of the same flavour considerations apply – these are rather more involved in the four quark amplitudes than the two gluon amplitudes. Contributions from Z and γ coupling directly to quark lines are accounted for in exactly the same way (as in Eq. (3.12)) except for this calculation only the double resonant diagrams are included.

Real emission

The real emission contributions involve an addition gluon but apart from that the flavour and helicity structure of the amplitudes are the same as for the leading order contributions. This is true for both the two quark, two gluon and the four quark contributions. For the two quark, two gluon amplitudes, the colour decomposition reads, in the same notation as Eq. (3.10),

$$\mathcal{A}^{\rm real}(\bar{q}_1, q_2, g_3, g_4, g_5; \nu_\mu, \mu^+, e^-, \bar{\nu}_e) = g_s^3 \left(\frac{g_W}{\sqrt{2}}\right)^4 \\ \times \sum_{\sigma=S_3} \left((T^{a_{\sigma_3}} T^{a_{\sigma_4}} T^{a_{\sigma_5}})_{i_2}^{\bar{i}_1} \; A_0(\bar{q}_1, q_2, g_{\sigma_3}, g_{\sigma_4}, g_{\sigma_5}) \right)$$

where A_0 is further split up as in Eq. (3.11), except here there is an extra gluon, where the sum is over all permutations of the three gluons. For the four quark amplitudes the colour decomposition is [9]

$$\mathcal{A}^{\rm real}(\bar{q}_1, q_2, \bar{q}_3, q_4, g; \nu_\mu, \mu^+, e^-, \bar{\nu}_e) = g_s^2 \left(\frac{g_W}{\sqrt{2}}\right)^4 \times \\ \Bigg[\delta_{\bar{i}_3 i_2} (T^a)_{i_4}^{\bar{i}_1} B_0(\bar{q}_1, q_2, \bar{q}_3, q_4, g) + \frac{1}{N_c} \delta_{\bar{i}_3 i_4} (T^a)_{i_2}^{\bar{i}_1} B_0(\bar{q}_1, g, q_2, \bar{q}_3, q_4) \\ \delta_{\bar{i}_1 i_4} (T^a)_{i_2}^{\bar{i}_3} B_0(\bar{q}_1, q_2, g, \bar{q}_3, q_4) + \frac{1}{N_c} \delta_{\bar{i}_1 i_2} (T^a)_{i_4}^{\bar{i}_3} B_0(\bar{q}_1, q_2, \bar{q}_3, g, q_4)\Bigg] \tag{4.6}$$

where B_0 is further split up as in Eqs. (3.15) and (3.16) (depending on the flavour structure), except here too there is an extra gluon, with a cyclic position made clear by its ordering in the argument of the amplitude. The presence of this gluon does not change any of the considerations about s- and t-channel contributions, nor the flavour structure which has been discussed in the context of the real emission part of the $WW + 1j$ calculation.

Virtual contribution

Here the two quark, two gluon amplitudes are very similar to the virtual amplitudes described in detail for $WW + 1j$. In particular, the flavour and helicity structures

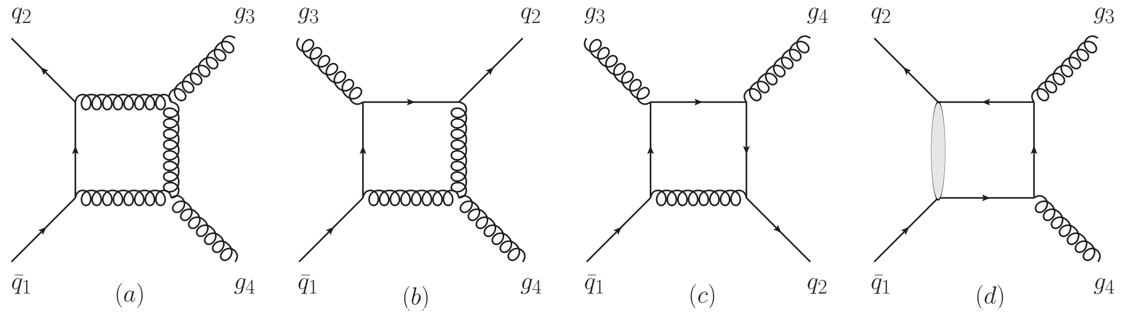

Figure 4.4: Left primitive amplitudes a) $A_1(\bar{q}_1, q_2, g_3, g_4)$, b) $A_1(\bar{q}_1, g_3, q_2, g_4)$, c) $A_1(\bar{q}_1, g_3, g_4, q_2)$, and d) $A_1^{[1/2]}(\bar{q}_1, q_2, g_3, g_4)$. The W bosons are not shown.

are the same. The extra gluon leads to a more complicated colour decomposition

$$\begin{aligned}\mathcal{A}^{1\mathrm{L}}(\bar{q}_1, q_2, g_3, g_4; \nu_\mu, \mu^+, e^-, \bar{\nu}_e) &= g_s^4 \left(\frac{g_W}{\sqrt{2}}\right)^4 \\ \times \sum_{\sigma\in S_2} \Bigg[&\left(T^{x_2} T^{a_{\sigma_3}} T^{a_{\sigma_4}} T^{x_2}\right)_{i_2}^{\;\bar{i}_1} A_1(\bar{q}_1, g_{\sigma_4}, g_{\sigma_3}, q_2) \\ &+ \left(T^{x_2} T^{a_{\sigma_3}} T^{x_1}\right)_{i_2}^{\;\bar{i}_1} \left(F^{a_{\sigma_4}}\right)_{x_1 x_2} A_1(\bar{q}_1, g_{\sigma_3}, q_2, g_{\sigma_4}) \\ &+ \left(T^{x_2} T^{x_1}\right)_{i_2}^{\;\bar{i}_1} \left(F^{a_{\sigma_3}} F^{a_{\sigma_4}}\right)_{x_1 x_2} A_1(\bar{q}_1, q_2, g_{\sigma_4}, g_{\sigma_3}) \\ &+ \frac{n_f}{N_c} \mathrm{Gr}_4 A_1^{[1/2]}(\bar{q}_1, q_2, g_{\sigma_3}, g_{\sigma_4}) \Bigg].\end{aligned} \tag{4.7}$$

where $\mathrm{Gr}_4 = N_c\left(T^{a_{\sigma_3}} T^{a_{\sigma_4}}\right)_{i_2}^{\;\bar{i}_1} - \mathrm{Tr}\left(T^{a_{\sigma_3}} T^{a_{\sigma_4}}\right)\delta_{\bar{i}_1 i_2}$. The amplitudes $A_1(\ldots)$ and $A_1^{[1/2]}$ are all left primitive amplitudes (see App. A) and are shown in Fig. 4.4. All of the same considerations for dealing with the colourless particles under the D-dimensional unitarity framework apply. Here though, a new feature is introduced in order to deal with the amplitude $A_1^{[1/2]}$, which is a fermion loop – this is the concept of a 'dummy line', shown in Fig. 4.4 (d) as a grey oval, which denotes a propagator which is never part of the loop. These dummy lines allows for 'all possible cuts' to be applied to a diagram with an additional rule imposed so that whenever a dummy line is cut, the contribution is thrown away. The W bosons (not shown in Fig. 4.4) can couple to the

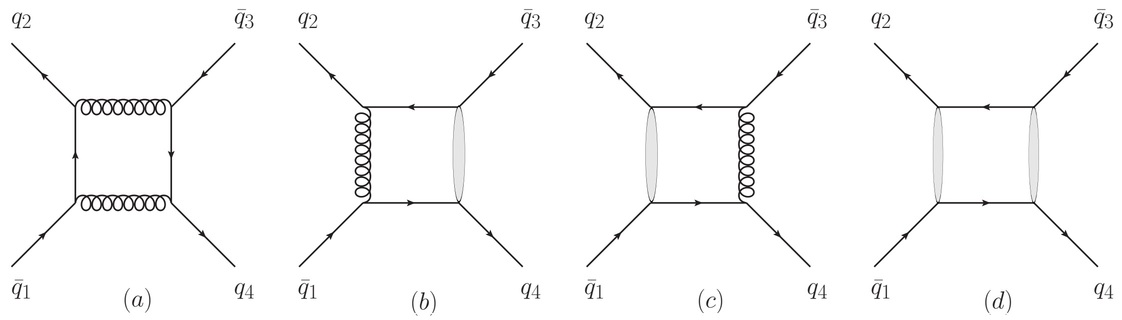

Figure 4.5: Diagrams for one-loop primitive amplitudes: (a) $B_1^{(a)}$, (b) $B_1^{(b)}$, (c) $B_1^{(c)}$, (d) $B_1^{(d)}$, for $0 \to (\bar{q}_1 q_2 \bar{q}_3 q_4) + W^+W^-$, where the flavours of the quarks are not specified, and the diagrams are examples with the maximum number of propagators (the W bosons are not shown). Shaded areas represent dummy lines which are not cut.

dummy lines[8]. This has the result that the amplitude in Fig. 4.4 (d) only consists of fermion loop contributions. The concept is very similar to the use of parent diagrams for dealing with the colourless W-bosons – dummy lines allow one to draw a diagram which contains the maximum number of propagators (six in this case, including the W-bosons). As in the $gg \to WWg$ process, the Berends-Giele recursion relations have to be modified in order to reproduce correctly the full one-loop amplitude.

For the four quark contributions, dummy lines are also used in the definition of the four different types of primitive amplitude $B^{(a,b,c,d)}$ which can occur – diagrams which involve a maximum number of propagators are shown in Fig. 4.5. The contributions $B^{(a)}$ can have the maximum of six propagators in the loop (the W bosons are again not shown in Fig. 4.5). The amplitudes $B^{(b,c)}$ have virtual gluon contributions which attach to one quark line only, and the amplitude $B^{(d)}$ is the fermion loop contribution.

[8]In Fig. 4.4 (d), the W bosons are not allowed to couple to the quark lines in the loop – these form the finite, gauge invariant contributions where the W bosons both couple to the fermion loop, which we neglect here, as in the $WW + 1j$ process.

The full four quark one-loop amplitude has the colour decomposition [9]

$$\begin{aligned}\mathcal{B}^{1\mathrm{L}}(\bar{q}_1,q_2,\bar{q}_3,q_4;\nu_\mu,\mu^+,e^-,\bar{\nu}_e) &= g_s^4\left(\frac{g_W}{\sqrt{2}}\right)^4\times\\ &\Big(\delta_{\bar{i}_1 i_4}\delta_{\bar{i}_3 i_2}B_1^{(1)}(\bar{q}_1,q_2,\bar{q}_3,q_4)+\delta_{\bar{i}_1 i_2}\delta_{\bar{i}_3 i_4}B_1^{(2)}(\bar{q}_1,q_2,\bar{q}_3,q_4)\Big)\,,\end{aligned} \tag{4.8}$$

where

$$\begin{aligned}B_1^{(1)}(\bar{q}_1,q_2,\bar{q}_3,q_4) &= \big(N_c-\frac{2}{N_c}\big)B_1^{(a)}(\bar{q}_1,q_2,\bar{q}_3,q_4)-\frac{2}{N_c}B_1^{(a)}(\bar{q}_1,q_2,q_4,\bar{q}_3)\\ &-\frac{1}{N_c}B_1^{(b)}(\bar{q}_1,q_2,\bar{q}_3,q_4)-\frac{1}{N_c}B_1^{(c)}(\bar{q}_1,q_2,\bar{q}_3,q_4)+n_f B_1^{(d)}(\bar{q}_1,q_2,\bar{q}_3,q_4),\end{aligned} \tag{4.9}$$

and

$$\begin{aligned}B_1^{(2)}(\bar{q}_1,q_2,\bar{q}_3,q_4) &= \frac{1}{N_c^2}B_1^{(a)}(\bar{q}_1,q_2,\bar{q}_3,q_4)+\big(1+\frac{1}{N_c^2}\big)B_1^{(a)}(\bar{q}_1,q_2,q_4,\bar{q}_3)\\ &+\frac{1}{N_c^2}B_1^{(b)}(\bar{q}_1,q_2,\bar{q}_3,q_4)+\frac{1}{N_c^2}B_1^{(c)}(\bar{q}_1,q_2,\bar{q}_3,q_4)-\frac{n_f}{N_c}B_1^{(d)}(\bar{q}_1,q_2,\bar{q}_3,q_4),\end{aligned} \tag{4.10}$$

where the following relation holds: $B_1^{(a)}(\bar{q}_1,q_2,q_4,\bar{q}_3)=(-1)\times B_1^{(a)}(\bar{q}_1,q_2,\bar{q}_4,q_3)$.

In this calculation, top and bottom quarks in the final state are not considered – these give rise to distinct experimental signatures. In particular, the QCD production of W^+W^- with a $b\bar{b}$ pair is dominated by the on-shell production of $t\bar{t}$, which has been studied in Refs. [69, 70, 71]. As in the calculation of W^+W^-+1j described in the previous Chapter, we choose to neglect all contributions from the third generation of quarks, and we do not include the production mechanism where the W bosons couple directly to a fermion loop. Both of these contributions to this process are expected to be small[9].

Because the production of $WW+2j$ can occur through an electroweak mechanism (to which the NLO QCD corrections are known [72]), there is an interference term

[9]The subsequent calculation of Ref. [68] found that these approximations do turn out to hold to the percent level.

between this and the QCD process, even at leading order. However, this interference is strongly suppressed, firstly because the electroweak production only occurs through four quark processes, and these only make up $\sim$ 15% of the QCD cross section. Further suppression occurs because the interference terms require the certain flavour combinations, and they are also colour suppressed. So the interference term is not considered in the following, and the QCD process alone is studied.

The input parameters used for this calculation slightly different to those used in Section 4.1.2. The W mass is taken to be $M_W = 80.419\,\text{GeV}$, and the W and Z widths are taken to be $\Gamma_W = 2.141\,\text{GeV}$ and $\Gamma_Z = 2.49\,\text{GeV}$. The electroweak gauge couplings are computed using the inputs $1/\alpha_{\text{QED}} = 128.802$ and $\sin^2\theta_W = 0.2222$, with the Z mass given by $M_Z^2 = M_W^2/(1 - \sin^2\theta_W)$. The parton distributions used are again those contained in the MSTW08 set – MSTW08LO for the leading order predictions and MSTW08NLO for the next-to-leading order predictions, corresponding to a strong coupling constant $\alpha_S(M_Z)$ of 0.13939 and 0.12018 respectively. Jets are defined through the anti-$k_\perp$ algorithm with $R = 0.4$, as implemented in FastJet. Quark mixing is neglected, and a unit CKM matrix is used throughout.

4.2.2 LHC predictions

The phenomenology of this process is presented in a slightly different way to that of the $0j$ and $1j$ bins – the cuts applied are 'generic' and are designed for observation of this process at the LHC. This is done as the following is the first calculation of the NLO QCD corrections to $pp \to WW + 2j$, so it is interesting to know how they affect the differential cross section over as much of the phase space as possible. The distributions which are relevant for Higgs phenomenology are investigated so as to look for any shape change in going from LO to NLO. In particular, cuts which reduce this background heavily in favour of the WBF signal are *not* applied, but the distribution $\eta_{j1} - \eta_{j2}$ is discussed below.

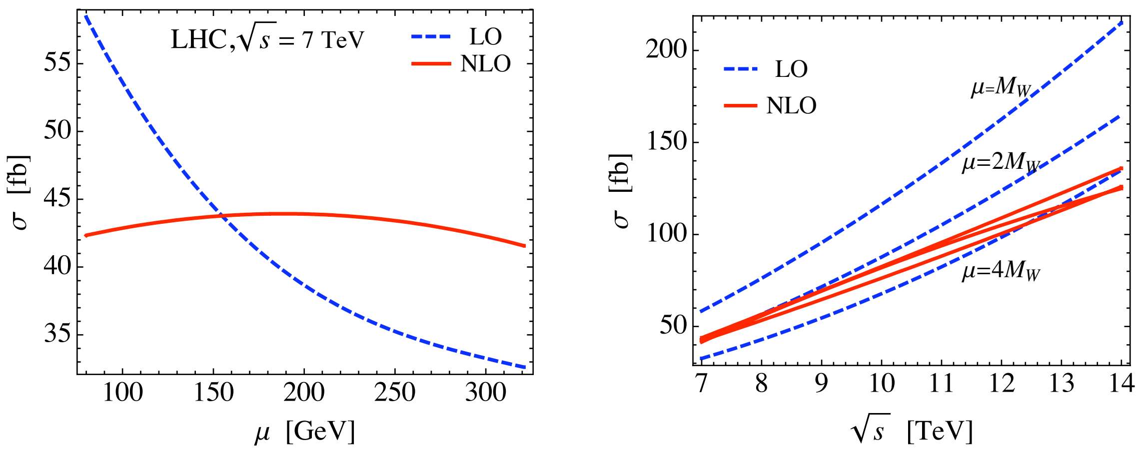

Figure 4.6: In the left panel, we show the production cross section of the process $pp \to W^+(\to \nu_\mu \mu^+)\, W^-(\to e^- \bar{\nu}_e) + 2j$ at the 7 TeV run of the LHC in dependence on the factorisation and renormalisation scales $\mu_F = \mu_R = \mu$, at LO and NLO in perturbative QCD. In the right panel, the dependence of the cross-section on the center-of-mass energy $\sqrt{s}$ is shown. LO results are shown in dashed blue; NLO results are in solid red. Three choices of μ are shown: $\mu = M_W, 2M_W, 4M_W$.

The cuts studied are: *i*) both leptons have transverse momenta $p_{T,l} > 20$ GeV and pseudorapidity $|\eta_l| < 2.4$, *ii*) the missing transverse momentum satisfies $p_{T,\text{miss}} > 30$ GeV, and *iii*) jets have transverse momenta $p_{T,j} > 30$ GeV and pseudorapidity $|\eta_j| < 3.2$.

The plots in this section are predictions for the LHC running at a centre of mass energy of 7 TeV[10]. The left panel of Fig. 4.6 illustrates the typical reduction in scale uncertainty in going from a LO to an NLO theoretical description of a process. In this plot the renormalisation and factorisation scales are set equal to each other, $\mu = \mu_R = \mu_F$, and are varied between $\mu = m_W$ and $\mu = 4m_W$. The LO scale dependence arises mainly from the running of the strong coupling (and only slightly on the factorisation scale), and the cross section for $pp \to W^+(\to \nu_\mu \mu^+)W^-(\to e^- \bar{\nu}_e)+2j$ has a value of $\sigma_{LO} = 46 \pm 13$ fb. At NLO the cross section is $\sigma_{NLO} = 42 \pm 1$ fb, which is a dramatic reduction in scale dependence. Here now, there is no significant jump

[10] At the time at which this work was published, this was the running energy, $\sqrt{s}$, of the LHC. We discuss the dependence of this process on $\sqrt{s}$ in this Section.

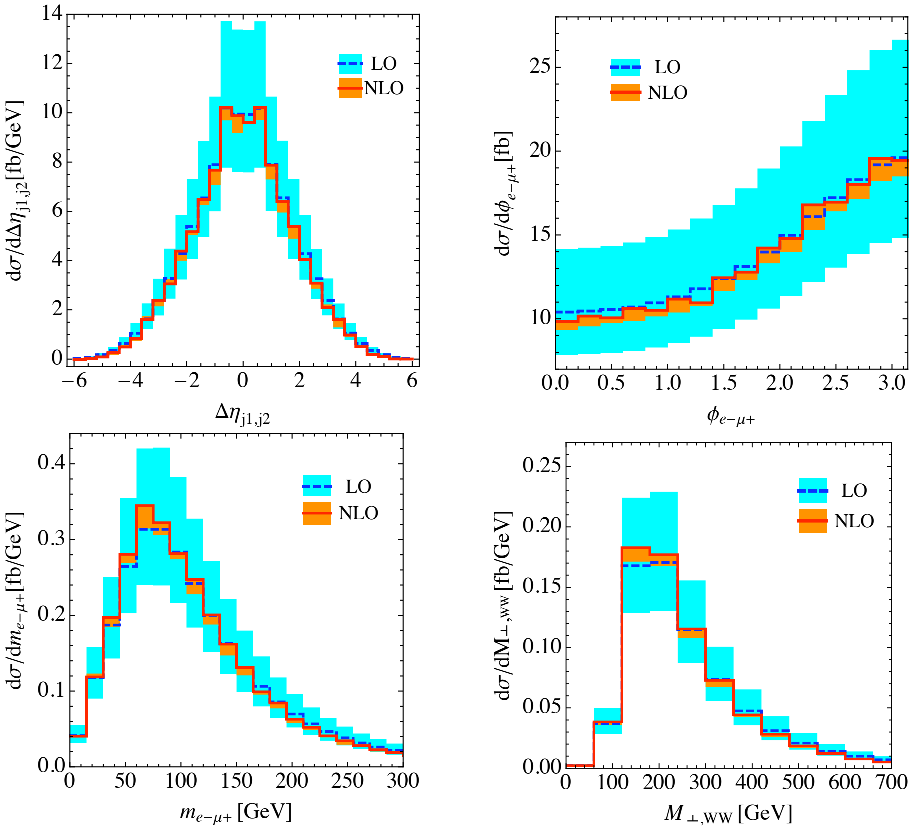

Figure 4.7: Distributions of jet pseudorapidity difference, lepton opening angle and invariant mass, and the transverse mass for $pp \to \nu_\mu \mu^+ e^- \bar{\nu}_e + 2j$ at the 7 TeV run of the LHC. LO results are shown in blue; NLO results are in red and orange. The uncertainty bands are for scale $M_W \le \mu \le 4M_W$, and the solid lines show the results at $\mu = 2M_W$.

in the value of the cross section after taking into account the NLO corrections – at $\mu = 2m_W$ the increase is only 2%. This is in keeping with the trend seen in going from the $0j$ to the $1j$ process, and now there are no new initial partonic states which become available when the NLO corrections are included. The NLO cross section lies well within the the LO scale uncertainty bounds, and there is a complete NLO description for all possible initial partonic states.

The different energies that the collider has and will be running at motivates the study of how the cross section for this process changes with $\sqrt{s}$. This is shown in right panel of Fig. 4.6, where predictions are given for different scales μ. Again, the reduced scale dependence at NLO is obvious in this plot, and the dependence on $\sqrt{s}$ becomes almost linear at this order. There is a change in the optimal[11] LO scale choice from $\mu = 2m_W$ at $\sqrt{s} = 7\,\text{TeV}$ to $\mu = 4m_W$ at $\sqrt{s} = 14\,\text{TeV}$. The LHC has collected around $5\,\text{fb}^{-1}$ of data at both 7 TeV and 8 TeV by the time of writing, and this corresponds to around $800 - 900$ $e^+e^- + \mu^+e^- + e^+\mu^- + \mu^+\mu^-$ events already, assuming a fifty percent efficiency. This demonstrates that on its own, this process is a viable one for detailed study as part of the LHC programme.

Distributions relevant to Higgs boson searches and studies for the set of cuts given above are displayed in Fig. 4.7. The distributions of ϕ_{ll}, m_{ll} and $m_{\perp WW}$ have been discussed before for the $0j$ and the $1j$ bins. Again here, this background prefers a large ϕ_{ll} in contrast to the signal process where the leptons tend to have a small opening azimuthal angle. The m_{ll} and $m_{\perp WW}$ distributions peak at higher values for this background than they do for the signal. These leptonic distributions in particular are those considered when devising 'Higgs search cuts' such as those in the previous section. A new distribution in the $2j$ bin which is shown is that of $\Delta\eta_{j_1 j_2} = \eta_{j_1} - \eta_{j_2}$, and it is peaked around $\Delta\eta_{j_1 j_2} = 0$ and has a very similar distribution to the signal process when it proceeds via ggF. This is in stark contrast to the distribution of the two jets produced in the WBF signal mechanism, which tend to have large values of $\Delta\eta_{j_1 j_2}$. A typical 'WBF search cut' of $|\Delta\eta_{j_1 j_2}| > 4.2$ would remove almost all of this background (and the ggF Higgs signal), as can be seen from Fig. 4.7.

Emphasis should be placed on how the description of these distributions changes when the NLO QCD corrections are taken into account. As would be expected from what has been seen with the total cross section, the reduction in scale uncertainty is striking in going from LO to NLO in QCD. These higher-order results should provide useful input for experimental analyses involving this process. There is very little shape change observed in any of the distributions shown in Fig. 4.7, and in fact in

[11]Defined as the scale for which the LO cross section equals the NLO result.

the work of Ref. [9], many more were analysed and in all cases the NLO K-factor was found to be spread evenly. It can be observed however from Fig. 4.7 that both the invariant mass and the transverse mass of the lepton pair are slightly softer when the NLO corrections are included.

4.3 Chapter Summary

In this Chapter we have presented phenomenology relevant for Higgs searches at the LHC in the decay mode $H \to WW$. This involved considering the processes $pp \to W^+W^- + nj$ with $n = 0, 1, 2$ which are standard model backgrounds in the different jet multiplicity search bins. In the $0j$ and the $1j$ bin, we investigated the impact of an NNLO contribution arising from the one-loop gluon-gluon fusion diagrams. We presented the calculation of the one-loop process $gg \to W^+W^-g$, which was performed using D-dimensional generalised unitarity. We found that this provides a significant contribution to the cross section when Higgs search cuts are applied, although slightly less so than for the $0j$ NNLO one-loop contribution, $gg \to W^+W^-$. The level at which both of these processes contribute was found to be highly sensitive to the cuts applied. For the $2j$ bin, we presented the NLO QCD corrections to the process $pp \to W^+W^- + 2j$, and presented phenomenologically relevant distributions for Higgs searches at the LHC. We found that the scale uncertainty in the theoretical predictions is significantly reduced by taking into account these corrections. In the next Chapter, we turn to phenomenology relevant for beyond the standard model physics searches at the LHC.

Chapter 5

Two Weak Bosons and New Physics at the LHC

Chapter Overview

The standard model explains a huge amount of collected data from many different particle physics experiments. There are, however, a number of experimental observations which it can not account for such as neutrino oscillations, the existence of dark matter, and of course the existence of gravitational forces. Even putting aside these experiments which require there to be physics beyond the standard model, within the standard model itself there are theoretical reasons which point towards some deeper theory of physics at a fundamental level. There is no explanation for the values that the nineteen parameters of the standard model take, and there are problems of naturalness due to the large hierarchy between the electroweak scale and the Plank scale.

Because of this, the standard model is considered to be an effective field theory which is valid up to some energy scale. If this scale is around a TeV, as suggested by arguments based on the level of naturalness present in the theory, then new physics should become apparent at the LHC. There are two ways to search for BSM physics at the LHC – through indirect searches, where the effect of the new physics is seen via deviations from predictions for the interactions of standard model particles, or through direct searches where new particles are actually produced in the detector.

The first part of this Chapter, Sec. 5.1, is concerned with indirect searches and deviations from the standard model predictions for W^+W^- and WZ production at the LHC. Any 'anomalous couplings' that the weak bosons possess would indicate the presence of physics beyond the standard model. The results in this section were first presented in [10] as part of an implementation of the processes $pp \to W^+W^-$, $W^\pm Z$, and ZZ production in a NLO calculation merged with a parton shower (NLO+PS) framework. The second part of this Chapter focuses on direct searches. Even if new particles are produced at the LHC, it is not necessarily easy to be able to detect and study them. One problem is knowing accurately the QCD background to the particular search channel. In Sec. 5.2, another example of an NLO QCD calculation with two weak bosons is presented, this time the more unusual process of $pp \to W^+W^+ + 2j$, which is a background to several interesting BSM searches involving like-sign leptons. In Sec. 5.3 we present research which addresses another difficulty that can arise in measuring the properties of any new particles produced at the LHC – we consider the issue of spin determination in a BSM scenario. Sec. 5.4 is a summary of the results contained in this Chapter.

5.1 Anomalous tri-linear gauge couplings in weak boson pair-production

The pair-production of two weak bosons in a single process provides a crucial test of the $SU(2) \times U(1)$ gauge invariance which lies at the heart of the standard model. It is the simplest process for which the self-interactions of the weak bosons play a role, and these interactions are a fundamental prediction of a non-abelian gauge theory. The couplings are completely fixed in the standard model by the $SU(2) \times U(1)$ gauge invariance, and any deviation from their SM values would indicate the presence of new physics.

When LEP was upgraded to LEP2, it started running at energies mainly above the threshold for producing W pairs (in its final year of running, it was collecting data at $\sqrt{s} = 205\,\text{GeV}$ and $207\,\text{GeV}$). This provided about 10,000 W-pair events for each experiment to analyse, and opened a window for precision tests of the gauge boson tri-linear self-couplings in the W^+W^- process [73], which is sensitive to both the $WW\gamma$ and the WWZ vertices. Effects of purely neutral gauge boson self-couplings $ZZ\gamma$, $Z\gamma\gamma$, and ZZZ were also searched for in the processes $e^+e^- \to Z\gamma$ and $e^+e^- \to ZZ$ – such vertices are not present in the standard model. No deviations from standard model predictions were observed, and limits were set on how large the anomalous tri-linear gauge couplings (ATGCs) could be.

The LEP experiment left a fantastic legacy of precision electroweak tests from the run at the Z pole and from the upgraded run, such as those above. Precision tests are not, however, associated so much with hadron collider physics, because of the large QCD backgrounds and the lack of knowledge of the centre of mass energy and longitudinal boost of the collision frame (this lack of knowledge is a subject which will be returned to in Sec. 5.3 of this Chapter as it can severely affect the ability to determine properties of new particles, such as their masses and spins). However, because hadron colliders can probe higher energies, if no new physics is seen then the scale at which it could appear is pushed to even higher energies which in turn places more stringent limits on the anomalous couplings. The bounds set by the Tevatron, which observed many W boson pairs over the course of its physics run [74, 75, 76], can not better those of the LEP machine. However, the LHC is able to place surprisingly strong bounds on these anomalous couplings, as will be illustrated below. Already published results quote bounds which are competitive with those from LEP, and with more data the LHC will go beyond the limits already set.

5.1.1 The anomalous coupling Lagrangian

The study of anomalous couplings given here will be restricted to the ATGCs tested in the processes $pp \to W^+W^-$ and $pp \to W^\pm Z$, that is to the anomalous vertices $WW\gamma$ and WWZ. The most general[1] Lagrangian which describes these interactions and which conserves C and P [2] takes the standard form [78]

$$\mathcal{L} = ig_{WWV}\left(g_1^V(W^+_{\mu\nu}W^{-\mu} - W^{+\mu}W^-_{\mu\nu})V^\nu + \kappa_V W^+_\mu W^-_\nu V^{\mu\nu} + \frac{\lambda_V}{M_W^2}W^{\nu+}_\mu W^{-\rho}_\nu V^\mu_\rho\right) \quad (5.1)$$

where $V = Z/\gamma$, $W_{\mu\nu} = (\partial_\mu W_\nu - \partial_\nu W_\mu)$, $V_{\mu\nu} = (\partial_\mu V_\nu - \partial_\nu V_\mu)$, $g_{WW\gamma} = -e$, and $g_{WWZ} = -e\cot\theta_W$. Electromagnetic gauge invariance requires the coupling $g^\gamma = 1$, and in the standard model, $g_1^V = 1$, $\kappa_V = 1$ and $\lambda_V = 0$ for $V = Z/\gamma$. Deviations from these values are parameterised as $\Delta g_1^V = 1 - g_1^V$, $\Delta\kappa_V = 1 - \kappa_V$ and $\Delta\lambda_V = \lambda_V$.

It is instructive to see how this Lagrangian comes out of a more structured effective field theory approach. Effective field theories are a powerful way to study physics in an energy regime where the details of higher energy effects are not important. The high energy degrees of freedom are integrated out, leaving only the relevant degrees of freedom for the problem at hand. This can be done systematically by ordering the Lagrangian as an expansion in inverse powers of the mass scale, Λ, at which the high energy degrees of freedom become important. It is a model independent, extremely general approach, and has the added benefit of being able to quantify to what extent

[1] With each term being constructed using the fewest number of derivatives. It is not clear from this viewpoint of writing down the most general Lagrangian why higher derivative, dimension six terms can be ignored, yet the dimension six λ term be included (derivatives come with a factor of m_W^{-1}, the only mass scale in the theory, and this does not suppress such terms at LHC energies). This point is only made clear within the effective field theory approach [77].

[2] The restriction to a Lagrangian which conserves C and P separately is for simplicity only – in general this does not have to be true.

any new physics is excluded.

The procedure is to write down all higher dimension (i.e. dimension greater than four) operators consistent with the gauge symmetries of the low energy theory, and which are composed of the fields which make up the particle content below the new physics scale Λ. Dimensional analysis requires these operators to come with inverse factors of a mass scale – this is the scale Λ where the new physics giving rise to these couplings becomes manifest. Here the low energy theory is taken to be the standard model (i.e. with the standard Higgs doublet to break electroweak symmetry), and so the effective Lagrangian is written as

$$\mathcal{L} = \mathcal{L}_{\rm SM} + \sum_i \frac{c_i}{\Lambda^i}\mathcal{O}_i \tag{5.2}$$

The coefficients of the higher dimensional operators, c_i, come with suppression factors of Λ^{-i} and so the ones with the lowest dimension are expected to dominate, the level of approximation in the expansion behaving like $([\text{low energy scale}]/\Lambda)^i$.

This approach can be applied to study ATGCs. Considering only dimension six operators constructed out of the fields of the standard model[3], and again making the restriction that C and P are separately conserved, the relevant ones for the WWV couplings are

$$\begin{aligned}
\mathcal{O}_{WWW} &= \mathrm{Tr}[W_{\mu\nu}W^{\nu\rho}W_\rho^\mu] && (5.3)\\
\mathcal{O}_W &= (D_\mu\Phi)^\dagger W^{\mu\nu}(D_\nu\Phi) && (5.4)\\
\mathcal{O}_B &= (D_\mu\Phi)^\dagger B^{\mu\nu}(D_\nu\Phi) && (5.5)
\end{aligned}$$

where $D_\mu = (\partial_\mu + \frac{i}{2}g\tau^I W_\mu^I + \frac{i}{2}g' B_\mu)$, $W_{\mu\nu} = \frac{i}{2}g\tau^I(\partial_\mu W_\nu^I - \partial_\nu W_\mu^I + g\epsilon_{IJK}W_\mu^J W_\nu^K)$, and $B_{\mu\nu} = \frac{i}{2}g'(\partial_\mu B_\nu - \partial_\nu B_\mu)$. The coefficients appearing in Eq. (5.2) can then be

[3]The only possible dimension five operator is a lepton number violating term which gives rise to a Majorana mass for neutrinos, and is not relevant for these tri-linear weak boson couplings.

related to those of the standard anomalous coupling Lagrangian of Eq. (5.1):

$$\begin{aligned} g_1^Z &= 1 + c_W \frac{m_Z^2}{2\Lambda^2} & (5.6)\\ \kappa_\gamma &= 1 + (c_W + c_B)\frac{m_W^2}{2\Lambda^2} & (5.7)\\ \kappa_Z &= 1 + (c_W - c_B \tan^2\theta_W)\frac{m_W^2}{2\Lambda^2} & (5.8)\\ \lambda_\gamma = \lambda_Z &= c_{WWW}\frac{3g^2 m_W^2}{2\Lambda^2} & (5.9) \end{aligned}$$

Eq. (5.9) and the relation which follows from Eq. (5.6)-(5.8),

$$\Delta g_1^Z = \Delta\kappa_Z + \tan^2\theta_W \Delta\kappa_\gamma \,, \tag{5.10}$$

reduce the number of free parameters from five (after imposing electromagnetic gauge invariance) to three. This is a consequence of including only up to dimension six operators – the inclusion of dimension eight operators would spoil these relations [79]. The inclusion of only up to dimension six operators in the expansion of Eq. (5.2) and the relations between coupling constants that follow is referred to as the 'LEP scenario'. For further simplification the 'HISZ scenario' [79] is sometimes employed for experimental analyses, where the number of free parameters is reduced further by assuming $c_W = c_B$.

The Lagrangian Eq. (5.1) gives rise to amplitudes which violate unitarity at high energy. From the effective Lagrangian point of view, this presents no inconsistency, because the effective theory is only valid for energies up to the scale Λ – above this scale the new physics becomes important. This is clear from the expansion Eq. (5.2), as the coefficients ([energy scale]$/\Lambda)^i$ become of $\mathcal{O}(1)$ and all higher dimension operators become important. The justification of keeping only the lower dimension ones is lost and so is the predictiveness of the theory.

However, it has been common practice, particularly in Tevatron analyses, to introduce form factors which temper the bad behaviour of the amplitudes by mimicking the behaviour of new physics. The couplings are given an energy dependence

$$\Delta g_1^Z \to \frac{\Delta g_1^Z}{(1 + M_{VV}^2/\Lambda^2)^2} \tag{5.11}$$

where M_{VV} is the invariant mass of the vector boson pair, and Λ is a value for the scale of new physics. This is an attempt to produce a more realistic prediction of what might be seen at a collider, at the expense of somewhat removing the model independence of the approach to studying these anomalous couplings. Results below are presented both with a form factor, in order to make contact with experimental analyses, and without one, where it should be understood that there is an upper limit of the validity of the theory given by the scale Λ.

5.1.2 WW, WZ and ZZ production in the `POWHEG BOX` and anomalous couplings

This section investigates the effect that anomalous couplings in the process $pp \to W^+(\to \nu_e e^+)W^-(\to \mu^- \bar{\nu}_\mu)$ can have on LHC observables. It begins with a brief description of the original work performed in Ref. [10], which involved the implementation of the processes ZZ, $W^\pm Z$, and W^+W^- in the `POWHEG BOX` program, including the anomalous couplings of Eq. (5.1).

The `POWHEG BOX` is a framework which exists to merge the results of an NLO calculation with a parton shower (PS) program. Parton shower programs can provide accurate predictions for exclusive quantities, as they sum contributions to all orders in regions of phase space where final particles become soft or collinear. This is in contrast to NLO calculations which can only provide accurate predictions for inclusive quantities – they take the soft and collinear divergences in the final state into account at finite order. When a scale is introduced to define an exclusive quantity (i.e. a jet transverse momentum), a fixed order calculation misses possible higher order large logarithms which involve this scale – this is the problem with the theoretical description of the jet binning of Higgs search results, as discussed in Chapter 4. The `POWHEG` method [80, 81] is one of two implemented techniques[4] to merge the two approaches, so that both the leading logarithmic behaviour of the parton shower *and* the NLO accuracy of inclusive quantities are included in the description of a process.

A discussion of NLO and PS matching is beyond the scope of this thesis – Ref. [83] is a good review. The `POWHEG BOX` will be treated as it is in a way designed to be treated, that is as a black box into which the NLO matrix elements and flavour and phase space information about a process are fed, and the NLO+PS matching proceeds automatically. However, the focus in this thesis will not be on the features of the outcome such a matching, the details of which can be found in Ref. [10]. Rather, it is the results (also in Ref. [10]) on anomalous couplings relevant to this section which are presented.

The work in Ref. [10] was instigated by the need for a full, public program to provide experimental collaborations with the implementation of electroweak boson pair production, including their fully spin-correlated leptonic decays, taking into account Z/γ^* interference, single resonant graphs, and the effects of interference between identical final state leptons, all at NLO+PS accuracy. The details of the implementation of the processes $pp \to WW/WZ/ZZ \to$ leptons are outlined in [10] and are not repeated in this thesis. The resulting code is available at the website [84].

This code is used for the following study of the ATGCs in both the $pp \to WW \to \nu_e e^+ \mu^- \nu_\mu$ and $pp \to W^\pm Z \to \nu_e e^\pm \mu^- \mu^+$ processes. A cut of $p_{t,\text{lead}} > 20\,\text{GeV}$ is made on the charged lepton with the hardest transverse momentum, and for all other charged leptons the cut $p_{t,l} > 10\,\text{GeV}$ is applied. For the WZ case, a cut on the invariant mass of the muon-antimuon pair $M_{\mu^-\mu^+} > 20\,\text{GeV}$ is made in order to ensure

[4]The other being MC@NLO [82].

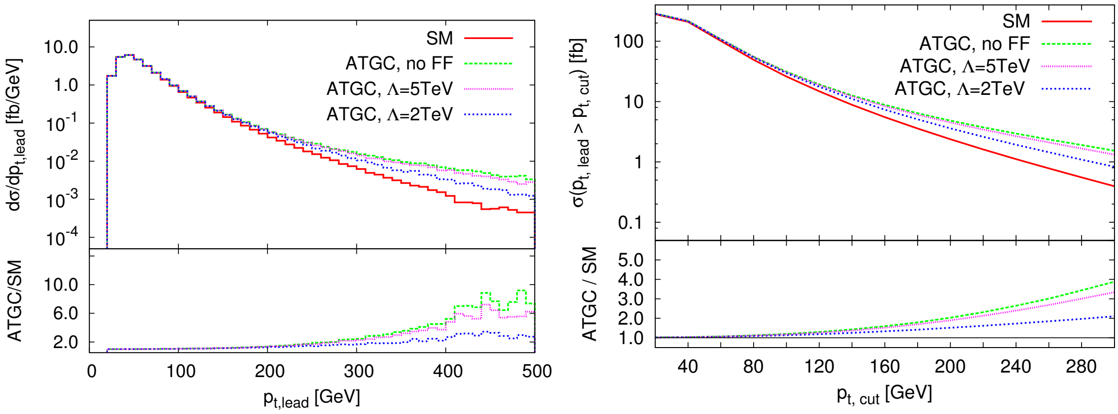

Figure 5.1: The p_T distribution for the leading lepton in W^+W^--production is shown on the left, and the integrated cross-section as a function of the cut on the transverse momentum of the leading lepton is shown on the right. The results are shown using Standard Model couplings (in red, labelled 'SM'), as well as with the anomalous couplings given in the text (in green, labelled 'ATGC, no FF'). The effect of a form factor given in Eq. (5.11) is also shown, both for a value of $\Lambda = 5$ TeV and $\Lambda = 2$ TeV (in pink and blue respectively).

that no divergence is encountered from soft photon emission. The implementation of anomalous couplings in the generator [84] allows for the six couplings of Eq. (5.1) to be set independently. However, following the discussion in the previous section, Δg_1^γ is set to zero to preserve electromagnetic gauge invariance, and the relations (5.9) and (5.10) are used so that only three input values are needed for the ATGCs. For the purposes of illustration, the values $\Delta g_Z = -0.027$, $\Delta\lambda_\gamma = -0.044$, and $\Delta\kappa_\gamma = -0.112$ are chosen[5].

The left hand panel of Fig. 5.1 shows the leading lepton transverse momentum in the process $pp \to WW$ both in the standard model case and with the above values for the anomalous couplings. Form factors as given in Eq. (5.11) are used for the ATGC curves, with different values of Λ (the case $\Lambda = \infty$ corresponds to using no form factors). The effects of the ATGCs appear, as is to be expected, when there is large energy transfer through the WWV vertex in the process; their contribution

[5]These correspond to maximum values of ATGCs consistent with the LEP bounds where each ATGC is allowed to vary independently.

Λ	Δg_1^Z	$\Delta\kappa_Z$	λ_Z
3 TeV	$[-0.064,\ 0.096]$	$[-0.100,\ 0.067]$	$[-0.090,\ 0.086]$
∞	$[-0.052,\ 0.082]$	$[-0.071,\ 0.071]$	$[-0.079,\ 0.077]$

Table 5.1: This table reproduces results from an ATLAS analysis, Ref. [85], showing 95% confidence limits on individual anomalous ATGCs, in the LEP scenario, assuming that the other couplings are set to their SM values.

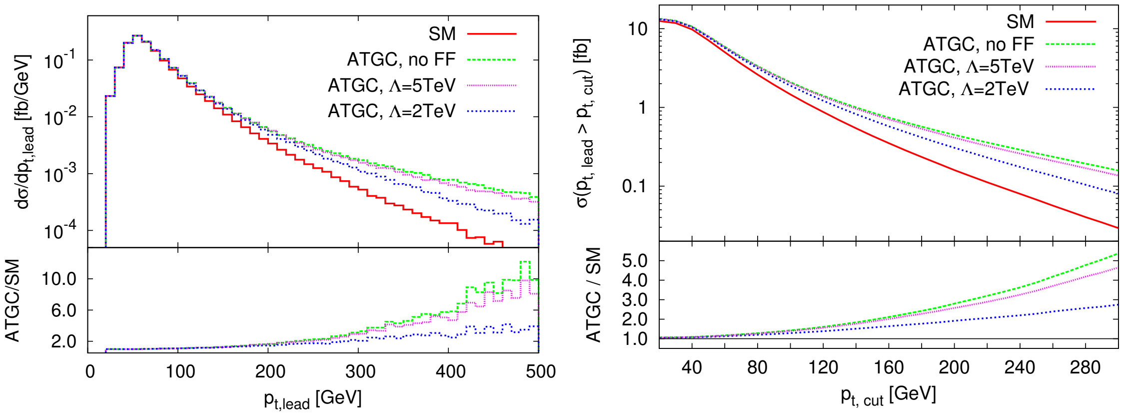

Figure 5.2: As in Fig. 5.1 for W^-Z production.

can be clearly seen in the high-p_t tail of the distribution. The advantage of the LHC is that because of the large collision energy, the cross section for producing such high-p_t leptons is sizeable, and discrimination between the standard model case and the anomalous case (which in practice would lie somewhere between the $\Lambda = \infty$ and standard model curves – the form factors give a feel for what might be seen) can take place. The right hand panel of Fig. 5.1 shows the total cross section for the $pp \to WW$ process as a function of the minimum cut on the leading lepton transverse momentum. When the hardest lepton is required to have $p_t \gtrsim 250\,\mathrm{GeV}$, the standard model cross section is about 1 fb, but with the given anomalous couplings, the cross section is around three times that. This will easily be discovered, or ruled out, by the LHC.

The ability of ATLAS and CMS to place good limits on these ATGCs has already been proven. A measurement of WW production[6] published by ATLAS with 1.02fb^{-1} of 7 TeV data, Ref. [85] derives 95% confidence limits on each anomalous ATGCs in the LEP scenario, assuming that the other couplings take their standard model values – we reproduce these numbers in Table 5.1.2. The limits set by ATLAS are already more stringent than those set by the Tevatron experiments [74, 75, 76], which is expected because of both the larger energy transfer through the WWV vertex, and also to the larger WW cross section at the LHC. With only 1.02fb^{-1} of data, and at this CoM energy, the ATLAS limits do not improve on the LEP limits, Ref. [73]. However, they come impressively close – especially given that the LEP limits are from the combination of four experiments, and they also include non-leptonic decays of the W bosons. With more data at higher energy, ATLAS and CMS will certainly be able to improve on the LEP limits.

The process $pp \to WZ \to$ leptons can also probe anomalous couplings, although this process is not sensitive to the $WW\gamma$ vertex. Fig. 5.2 illustrates the effect of anomalous couplings taking the same numerical values as above on the high-p_t lepton spectrum. Again, in the high transverse momentum region, the cross section differs from the standard model one. However, the limits placed here are less stringent because the cross section is an order of magnitude smaller – the published ATLAS measurements of WZ production [86] with 1.02fb^{-1} of 7 TeV data place less stringent limits on the ATGCs than those published for WW results.

With more data at higher energy, the LHC will be able to study the above ATGCs in more detail, as well as searching for other anomalous tri-linear couplings in processes such as ZZ and $Z\gamma$ production (published analyses for these already exist – see Refs. [87, 88]), and anomalous quartic couplings in processes with three vector bosons in the final state. It is exciting that there is such an opportunity for new physics to present itself in this sector over the coming years. If on the other hand nothing is

[6] In the decay channel $WW \to l\nu l\nu$, where l is an electron or a muon.

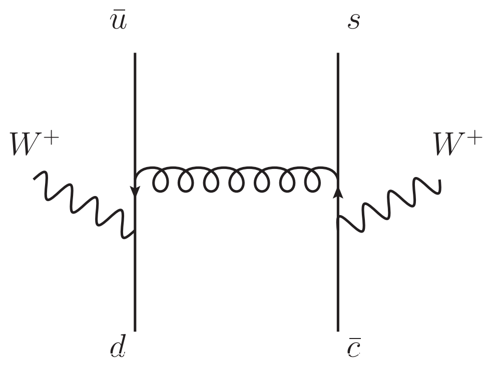

Figure 5.3: A Feynman diagram for the process $pp \to W^+W^+ + 2j$ (all particles are outgoing).

seen which deviates from the standard model, the effective Lagrangian approach will place strong constraints on the scale at which new physics can affect these weak boson vertices. This is interesting in itself, because it will in turn place constraints on any BSM model which aims to address the experimental and theoretical problems that the standard model alone can not explain.

5.2 $W^+W^+ + 2j$ as a background to BSM physics

If new particles are created at the LHC, looking for and interpreting the detector signatures they produce is essential work. This involves a full understanding of the standard model background for the particular signature under consideration, so that any excess can be identified. As always, the input must be both experimental and theoretical, and for accurate theoretical predictions, NLO QCD corrections to contributing processes should be taken into account. As for most searches at the LHC, those which involve leptons in the final state benefit from a QCD background which is relatively small (compared to that for fully hadronic final states), and which is under better experimental and theoretical control. The processes of W^+W^-+jets production which were presented at NLO (and beyond) in QCD in the previous Chapter as backgrounds to Higgs searches are of course also relevant as backgrounds to BSM searches. Popular BSM theories such as R-parity conserving SUSY or Universal Extra Dimensions (UED) have a classic detector signature of two oppositely charged leptons, jets and missing energy (here there is missing energy because the lightest of the new particles is stable and invisible to the detector, taking away unobserved transverse momentum from the event). The processes W^+W^-+jets, where the W bosons decay leptonically (the neutrinos providing the missing energy), are irreducible standard model backgrounds to such events.

A particularly stark detector signature that can arise in BSM theories occurs when there are same-sign leptons in the final state of the event. The reason that this signature is a good one is that is quite exotic – the standard model background is very small. Example BSM scenarios which can give rise to same-sign leptons in association with jets are: resonant slepton production in R-parity violating supersymmetry [89]; the production of a doubly charged Higgs boson [90]; and di-quark production, with subsequent decay of the di-quark into pairs of top quarks [91]. Both ATLAS and CMS have searches specifically looking for same-sign leptons, with and without jets and missing energy (see e.g. Refs. [92, 93]).

The first time same-sign leptons are produced in a single standard model process[7] has to be in association with two jets, via diagrams like the one shown in Fig. 5.3. The electroweak production mechanism, with the exchanged gluon being replaced by a neutral weak boson, is also important, and we will discuss this in more detail below. We proceed to a description of the process $pp \to W^+W^+ + 2j$ at NLO in QCD, and because of its small cross section we will present results for the 14 TeV LHC, where it takes a value of about 1pb and is therefore accessible. Observation at the LHC is interesting in its own right, since it is an exotic standard model process. And as a

[7]The phenomenon of double parton scattering (DPS) can also give rise to same-sign leptons – Ref. [94, 95, 96] suggests that this signature can be used to measure the rate at which DPS occurs at the LHC.

background, it should be remembered that many of the BSM processes also have a similar sized cross section, so despite its small rate, it is still relevant.

5.2.1 NLO QCD results for $pp \to W^+W^+ + 2j$ at $14\,\mathrm{TeV}$

There are several reasons why $pp \to W^+W^+ + 2j$ is an interesting processes theoretically. Firstly, it is a $2 \to 4$ process and so is a considerably complicated one for which to calculate the NLO QCD corrections. It provides a challenging test of the method outlined in Chapter 2, especially since there are two colourless particles in the final state. Secondly, the graphs which contribute to this process form a subset of those which contribute to $pp \to W^+W^- + 2j$ (the order in which these different calculations are presented in this thesis is contrary to the order in which the research was performed). The present calculation of Ref. [9] was seen as a stepping-stone to the calculation of $pp \to W^+W^- + 2j$ which, given its importance as a background to Higgs searches, is arguably a more important process to know accurately at the LHC. Finally, $pp \to W^+W^+ + 2j$ exhibits interesting behaviour in that the cross section is infrared finite as the jet transverse momentum goes to zero. Charge conservation requires one W^+ particle to be emitted from each quark line (see Fig. 5.3), and this prevents any IR divergence in the LO amplitude. This allows for the study of $W^+W^+ + n$ jets, where $n = 0, 1, 2$ or $n \geq 2$, which in turn allows for a knowledge of how jetty this process is – this is useful when considering it as a background to BSM physics as jet vetoes could be imposed in such a search.

The electroweak production is larger than would be naively expected from the different magnitude of α_S and α_{EW}, and given that $\sigma_{\mathrm{EW}} \sim \alpha_{\mathrm{EW}}^4$ and $\sigma_{\mathrm{QCD}} \sim \alpha_{\mathrm{EW}}^2 \alpha_S^2$. In fact the QCD production is only around 50% larger. The NLO QCD corrections to the electroweak production process have calculated in Ref. [97][8]. The two different mechanisms interfere, so they cannot just be computed separately and their individual

[8]This calculation, although also a $2 \to 4$ process, does not require anything higher than four-point tensor integrals, in contrast to the six-point tensor integrals required for the QCD process.

contributions added. However, the interference terms are doubly suppressed – they occur at sub-leading colour only, and only when all the quarks are identical. We will proceed by considering the QCD production alone. As the structure of these amplitudes has already been discussed in the previous Chapter for the process $W^+W^- + 2j$ we will not present this here again, and proceed straight to phenomenological results.

Results are presented for the final state $e^+\nu_e\mu^+\nu_\mu$, and results for the full leptonic state ($l = e, \mu$) can be obtained by multiplying the results by a factor of two, neglecting interference terms which occur when there are identical leptons in the final state[9]. The following cuts are imposed: *i)* both leptons have $p_{T,l} > 30\,\text{GeV}$, *ii)* the lepton rapidities are $|\eta_l| < 2.5$, and *iii)* the missing transverse momentum $p_{T,miss} > 30\,\text{GeV}$. Jets are defined as having $p_{T,j} > 30\,\text{GeV}$ and $|\eta_j| < 3.5$, using the anti-k_T algorithm with $R = 0.4$, as implemented in FastJet. We will consider all the 0, 1, 2 and ≥ 2 jet cases, since the cross section is finite even as the jet transverse momentum goes to zero. Results are presented using the MSTW08LO and MSTW08NLO parton distribution functions for the leading order and NLO calculations respectively. Electroweak inputs values are $M_W = 80.419\,\text{GeV}$, $\Gamma_W = 2.140\,\text{GeV}$, $\sin^2\theta_W = 0.2222$, and $\alpha_{EM}(M_Z) = 1/128.802$. The results for $pp \to W^-W^- + 2j$ can be obtained by considering the process $\bar{p}\bar{p} \to W^+W^+ + 2j$, reversing any parity odd distributions and simply treating the final state leptons as negatively charged [97] – this process is $\sim 40\%$ of the size of the results found below.

The cross sections for the LO and NLO theoretical predictions for $pp \to e^+\nu_e\mu^+\nu_\mu +$ n jets are shown in Fig. 5.4 with *i)* $n \geq 2$, *ii)* $n = 2$, *iii)* $n = 1$, and *iv)* $n = 0$ with a varying renormalisation scale and factorisation scale, which we set equal to each other $\mu_R = \mu_F = \mu$. The leading order dependence for all cases is driven by the dependence of α_s on the renormalisation scale – the cross section increases monotonically as μ is decreased. For the two jet inclusive NLO cross section, the scale dependence is re-

[9]Such terms are highly suppressed as they force the W bosons off-shell.

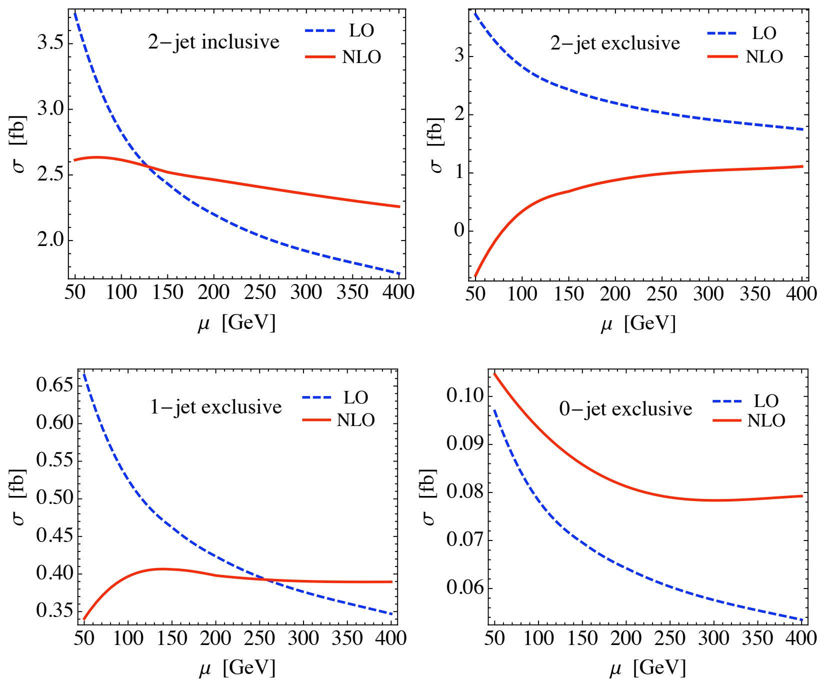

Figure 5.4: The dependence on factorisation and renormalisation scales of cross-sections for $pp \to e^+ \mu^+ \nu_e \nu_\mu + n$ jets, $n = 0, 1, 2$ at leading and next-to-leading order in perturbative QCD. We set the two scales equal to each other $\mu_F = \mu_R = \mu$.

duced quite dramatically: varying μ between 50 GeV and 500 GeV, $\sigma_{LO} = 2.7 \pm 1.0$ fb compared with $\sigma_{NLO} = 2.44 \pm 0.18$ fb, which is a reduction in scale dependence from 40% to less than 10%.

Both the 1-jet exclusive and 0-jet exclusive cross sections exhibit a similar reduction in dependence on scale, but the trend is not so for the 2-jet exclusive cross section. Because of its exclusive nature, it is reasonable to expect that it is a poor convergence of the perturbation series which accounts for the bad behaviour of the cross section, which even goes negative below $\mu = 80$ GeV. This can be tested by tightening up the transverse momentum cut on the jet, to remove the effect of large logarithms of the form $\log(p_{T,j}/M_W)$. The change in both the inclusive and exclusive two jet cross sections as the $p_{T,j}$ cut is increased is shown in Fig. 5.5, where the scale is varied between 100 GeV and 200 GeV, with a central value of $\mu = 140$ GeV. It can be seen that the dependence of the exclusive cross section becomes better behaved as

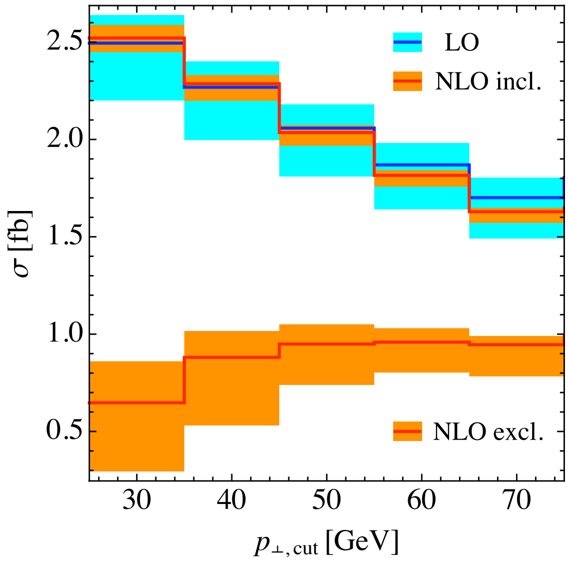

Figure 5.5: The dependence on the jet $p_\perp$ cut of the 2-jet inclusive and 2-jet exclusive cross-sections for $pp \to e^+\, \mu^+\, \nu_e\, \nu_\mu + 2j$ at leading and next-to-leading order in perturbative QCD. We show scale uncertainty bands, for values of the renormalisation and factorisation scales set to a common value μ, which is varied in the interval 100 GeV $\leq \mu \leq$ 200 GeV. Results for $\mu = 140$ GeV are shown as solid lines.

this jet cut is increased. However, it is unclear why the 1-jet and 0-jet exclusive cross sections are so much better behaved than the 2-jet exclusive.

The total number of $e^+\mu^+ + e^+e^+ + \mu^+\mu^+$ events coming from this standard model process at the 14 TeV LHC for 10 fb^{-1} of luminosity is around 60, which although a small number is certainly observable, given the distinct signature. This number is of the same order of magnitude as the number of events which could be expected from the possible BSM signals discussed at the beginning of this section. The cross sections above indicate that most events will contain at least two jets as well as the same-sign leptons, and that roughly half of these events will contain a relatively hard third jet. Although the precise value of the 2-jet exclusive cross section is somewhat unclear, the results indicated by Fig. 5.5 suggest that this conclusion holds true. With the presence of a relatively hard third jet in the standard model events, it is possible that selection cuts for BSM searches could utilise this feature. We found that dependence

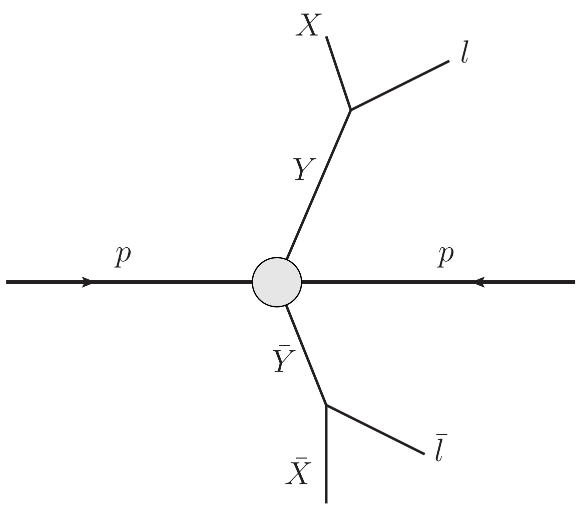

Figure 5.6: The event topology $pp \to Y\overline{Y} \to lX\bar{l}\,\overline{X}$.

of these results on the value of R used in the jet definition is small.

5.3 Spin determination of new states

When two charged weak bosons are produced, and when they decay leptonically, $pp \to W^+(\to \nu_e e^+)W^-(\to \mu^- \bar{\nu}_\mu)$, there is not enough information in the final state to be able to completely reconstruct the kinematics of the event. This is because the neutrinos evade detection, and because the boost and the centre of mass energy of the initial partonic collision are unknown. This means, for instance, that the invariant mass of either W can not be reconstructed, nor the invariant mass of the WW system – this is particularly unhelpful for Higgs searches in the $H \to W^+W^-$ channel, as no resonant mass peak can be reconstructed from the data, and this is one of the reasons why discovery and mass determination in this channel is more challenging than in $H \to ZZ^* \to 4l$ or $H \to \gamma\gamma$. In this thesis we have already met a variable related to the WW invariant mass – the transverse mass $m_{T,WW}$, defined in Eq. (4.4). Even if there was no resonance seen in other fully reconstructed channels, a fit of the observed data in the $H \to WW$ channel could be performed for different values of the Higgs mass. This, with enough data, would select a preferred mass for the H resonance.

Similar complications can arise in a wide class of new physics events at the LHC, in particular those arising from BSM theories which invoke some symmetry which (a) requires new particles to be produced in pairs, and (b) also implies that the lightest of the new states is stable (and therefore must only interact very weakly with standard model matter). Examples of such theories are R-parity conserving SUSY and UED. Conditions (a) and (b) ensure that in each event there are two new particles which will be invisible to the detector and that the final state is not reconstructible.

The situation is even more difficult than the $H \to WW$ case discussed above, because there can be many new states which are produced which all have unknown masses, spins and other quantum numbers, and all of which we would want to determine experimentally. The subject of the final section of this thesis is a method of using observables which are sensitive to the spin of new particles produced at the LHC. This falls under the broader topic of LHC phenomenology which this thesis encompasses, but it is fitting that the topology in which spin determination is studied in what follows is exactly the topology of the production of two charged weak bosons $pp \to W^+(\to \nu_e e^+)W^-(\to \mu^- \bar{\nu}_\mu)$. We shall also find that the standard model background to the process we consider are the weak boson pair production processes implemented in the `POWHEG BOX`: $pp \to WW$, WZ, and ZZ.

5.3.1 Initial discussion

We will study a method of spin determination in the topology shown in Fig. 5.6: a new particle-antiparticle pair $Y\overline{Y}$ is produced, followed by the decays $Y \to lX$ and $\overline{Y} \to \bar{l}\,\overline{X}$ where l is either an electron or a muon, and X and $\overline{X}$ are the lightest of the new particle states, which we assume are stable and invisible to the detector. We investigate the use of observables which do not take as input the mass spectrum of Y and X and show that the two introduced here are independent of the mass of X. The first is related to the variable $\cos\theta_{ll}$ introduced in Ref. [98], which approximates the polar production angle, $\cos\theta$, of Y with respect to the beam axis in the $Y\overline{Y}$ centre of mass frame. We find an improvement on $\cos\theta_{ll}$'s statistical power in determining the spin of Y. The second is an asymmetry which picks up on a term which can be present in the production matrix element squared for a spin half Y, $|\mathcal{M}|^2 \propto \pm\cos\theta$. We will discuss the possibility of using this asymmetry to provide information about the couplings of Y, something which is difficult to do using polar angle distributions alone.

The problems that come with having two invisible particles in the final state of an event have been discussed above. Because mass measurement is usually 'easier' than spin measurement, in the sense that fewer events are required to obtain a reasonably accurate result, methods of spin determination are often happy to make the assumption that the mass spectrum of the theory is known. We do not go into detail here as to the methods which can be employed at hadron colliders to measure mass, and instead refer the reader to a recent review [99]. It is true, however, that the event topology being considered is an example in which mass determination is particularly difficult [100]. This is down to not having two or more visible particles in the decay chain of Y – there are no edges or endpoints which could come from the invariant mass distributions of such particles to provide relations between the new state masses and help to pin them down [99]. Nor is there an experimentally stark M_{T2} 'kink' [101, 102, 103] which would point directly to the mass of both particles. It would require many events to determine even the mass scale of the new physics, or else rely on mass measurements from elsewhere. At any rate, it is interesting to ask the question: what can we say about spin without any knowledge of the particle masses?

Likelihood analysis techniques for spin determination use the complete event information and so can make statistically optimal statements, but their implementation becomes extremely complicated if the masses are unknown and need to be scanned over. Methods based on the total cross section [104] can also be very powerful, as can those which use kinematic reconstruction [105, 106, 107], but they too require at least the masses to be known before they become useful. We shall investigate spin determination during an initial discovery phase, before these two techniques become viable, simply by studying the angular distributions of visible particles in this topology – these are affected by the particular spin configuration at hand [98, 108, 109, 110]. We shall find that the properties of the observables introduced here make them ideal for use in a 'no mass input' approach and this leaves us in a position where it actually becomes possible to determine the spin of a new particle before we know its mass.

5.3.2 Theoretical testing ground

To introduce and illustrate the use of the new variables, we will consider the s-channel production of Y and $\overline{Y}$ by a spin one particle Z, as shown in Fig. 5.7, where Y is either a spin zero or a spin half particle. The particle Z could be either the standard model Z^0 weak boson or it could be some new spin one state. We aim to discriminate between these two spin assignments where the Ys are produced according to distributions which go something like $\sim \sin^2\theta$ and $\sim (1+\cos^2\theta)$ respectively. We make the assumption that one can neglect all production diagrams other than the one in Fig. 5.7 – we shall discuss how this situation can arise shortly – and continue in a model independent fashion. We allow for the couplings between Z and Y to be those of the most general, renormalisable interaction: $CZ^\mu(Y^*(\partial_\mu Y) - (\partial_\mu Y^*)Y)$ for a spin zero Y and $\overline{Y}\not{Z}(V + A\gamma_5)Y$ for a spin half Y, where C, A and V are the coupling constants. Because we are considering an early discovery phase at the LHC when the cross section for such a process won't be accurately known, we shall be comparing normalised distributions of variables. Given this, in the spin zero case there is no room for manoeuvre – the spin contribution is fixed as there is just an overall factor

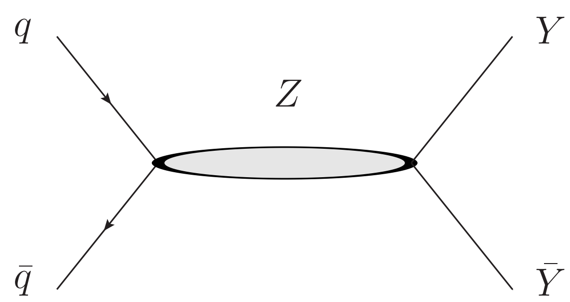

Figure 5.7: Production of $Y\overline{Y}$ by a spin one particle, Z, in the s-channel.

of the coupling constant, C. On the other hand, for the spin half case, there is the relative size of V and A, the vector-like and axial-like couplings of Y to Z, which is a free parameter in this set-up.

Under what conditions does the diagram of Fig. 5.7 dominate the production of $Y\overline{Y}$? The importance of other diagrams, especially t-channel ones, must be minimal, since these can serve to make equal the angular distributions for spin zero and spin half Y [111]. Fig. 5.7 automatically depicts the dominant production mechanism in the case where $M_Z > 2M_Y$ so that the particle Z, some new state, is resonantly produced. Alternatively, one could simply imagine that some symmetry of the theory describing these particles forbids any t-channel diagram[10]. Because the former situation is more general, we choose to select some example masses for Y and Z so that Z can be resonantly produced, and use these values to illustrate the various steps along the way. We take $M_Y = 800\,\mathrm{GeV}$ and $M_Z = 2.5\,\mathrm{TeV}$, and we shall return to discuss how different choices for these masses affect our results (and will find that so long as Y and $\overline{Y}$ are reasonably well boosted in the LAB frame, which can happen for both $M_Z \gtrless 2M_Y$, then this is all we need to leave our conclusions unchanged). We shall also present results for the case when Z is the standard model Z^0.

[10]For example in the supersymmetric example in Ref. [98], $Z = Z^0$ and so $M_Z < 2M_Y$ and there is no resonance. But here the Ys are sleptons and conservation of lepton and baryon number forbids any tree level t-channel diagrams.

The two different spin assignments provide two different matrix elements to evaluate. We choose to do so in the centre of mass frame of the $Y\overline{Y}$ pair, where we write Y's momentum as $p_Y^{\rm CM} = \gamma M_Y\,(1, 0, \beta\,\sin\theta, \beta\cos\theta)$, where β is the velocity of Y and $\gamma = 1/\sqrt{1-\beta^2}$. In terms of these variables, the matrix element squared, summed over final particle spin and averaged over initial quark spin and colour is

$$\overline{|\mathcal{M}|^2} = \mathcal{N}\; F_+\; P(\gamma)\;{\rm SPIN}(\beta, \cos\theta)\,, \tag{5.12}$$

where

$$P(\gamma) = \frac{\gamma^4}{(4\,\gamma^2 - M_Z^2/M_Y^2)^2 + (\Gamma_Z M_Z/M_Y^2)^2} \tag{5.13}$$

shows the effect of the Z propagator with a Breit-Wigner width Γ_Z, $\mathcal{N}$ is a numerical constant and F_+ is given in terms of the vector and axial couplings of Z to the quarks

$$F_+ = (f_q^V)^2 + (f_q^A)^2\,. \tag{5.14}$$

Now we turn to the important difference. For a spin zero Y

$${\rm SPIN}(\beta, \cos\theta) = C^2\,\beta^2\left(1 - \cos^2\theta\right)\,, \tag{5.15}$$

whereas for a spin half Y

$${\rm SPIN}(\beta, \cos\theta) = V^2\left(2 + \beta^2(\cos^2\theta - 1)\right) + A^2\,\beta^2\,\left(1 + \cos^2\theta\right) \pm 8\frac{f_q^A f_q^V}{F_+} V A\,\beta\cos\theta\,. \tag{5.16}$$

We see an interesting final term in Eq. (5.16), asymmetric in $\cos\theta$, which arises from an $\epsilon^{\mu\nu\rho\sigma}$ term coming out of the Dirac matrix algebra. This term is positive if $\theta = 0$ is taken in the direction of the quark, and is negative if it is taken in the direction of the antiquark. Non-zero vector and axial couplings are needed at both the $Zq\overline{q}$ and the $ZY\overline{Y}$ vertices for this term to be present in the first place. At this stage then we discuss the coupling of Z to the quarks, through f_q^V and f_q^A. The overall factor of F_+ in Eq. (5.12) will not affect the normalised distributions we are interested in and so the only place these couplings matter is in determining the relative size of the asymmetric term. We proceed by considering the case where $f_q^A f_q^V / F_+ \sim \mathcal{O}(1)$ and find it useful to just take the values of these couplings as we would were Z the standard model Z^0. This way, when we later set the mass and width of Z to those of Z^0, this particle couples as the true standard model particle to the quarks.

Finally we let the pair-produced particles decay: $Y \to lX$ and $\overline{Y} \to \bar{l}\,\overline{X}$. We let the above decay happen isotropically in the rest frame of Y, which means we take no spin correlations into account. To ignore spin correlations is to ignore an interesting way of determining spin in these situations (if the correlations are there, Y and $\overline{Y}$ are not spin zero), but here they only have a small effect for two reasons. The first is that because all the final spin states are being summed over, the correlation is only observable through an overall production polarisation of Y and $\overline{Y}$, if one exists. Secondly, Y and $\overline{Y}$ are produced with a sizeable boost in the LAB frame – this acts to wash out the effect of any lepton-lepton correlation. Because X and $\overline{X}$ are invisible to the detector, the final state cannot be reconstructed and in particular $\cos\theta$ can not be measured.

5.3.3 Variables to determine spin

In reference [98], Barr introduces a variable which approximates $\cos\theta$ in the production and decay topology described above. This variable $\cos\theta_{ll} = \tanh(\Delta\eta_{ll}/2)$ is invariant under longitudinal boosts as it is a function of $\Delta\eta_{ll}$, the pseudorapidity difference between the leptons. This is an attractive quality at the LHC where we do not know the boost of the partonic centre of mass frame along the beam-axis.

In a similar fashion, we now introduce a new visible variable $\cos\theta^V$, which we

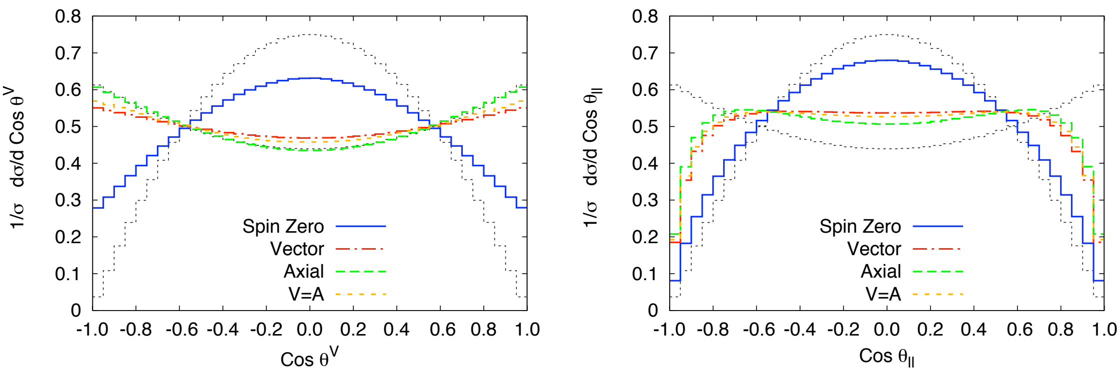

Figure 5.8: Comparing the distribution of the variable introduced here, $\cos\theta^V$ (left), with that of $\cos\theta_{ll}$ (right) for the different spin scenarios described in the text. The faint, grey, dotted lines show the true $\cos\theta$ curves for a spin zero Y, and for a spin half Y with a purely vector coupling (in the left hand plot, this lies beneath the purely axial coupling (green) curve). We use the example masses for Y and Z. The mass of X has absolutely no impact on the shape of these distributions.

define as the cosine of the angle between l's direction of motion and the beam-axis in the centre of mass frame of the two visible leptons. That is one takes the sum of lepton momenta $P = p_l + p_{\bar{l}}$, calculates the invariant mass $m_{ll} = \sqrt{P^2}$ and boosts the lepton momenta into the frame in which $P = (m_{ll}, 0, 0, 0)$. This is the reference frame in which the angle θ^V is defined. This new variable $\cos\theta^V$ coincides with $\cos\theta_{ll}$ when the leptons have equal and opposite transverse momenta.

We plot the distribution of both of these visible variables in Fig. 5.8 for pp collisions at 14 TeV and using our example masses for Y and Z. Normalised differential cross sections are shown for four different cases for the couplings: a spin zero Y; a spin half Y with a purely vector coupling (that is, setting $A = 0$ in Eq. (5.16)); a spin half Y with purely axial couplings (setting $V = 0$ in Eq. (5.16)); and a spin half Y with mixed couplings, where we choose for illustration $V = A = 1$. To produce the distributions we need also to select a value for the mass of X, and we choose $M_X = 500\,\text{GeV}$. The remarkable thing is that we could choose any value of M_X here ($M_X < M_Y$, of course) and the distributions shown in Fig. 5.8 would stay exactly the same. A proof that this interesting result must hold is given in App. D.

In Fig. 5.8 the true $\cos\theta$ distributions are faintly shown and we can see that $\cos\theta^V$ tracks these true curves better than $\cos\theta_{ll}$, which suffers from a pseudorapidity 'drag down' at large $|\cos\theta_{ll}|$. However, the important point is how well the visible curves can be distinguished from one another. By eye one might expect $\cos\theta^V$ to perform better – this is made into a statistical statement once detector effects have been taken into account in Sec. 5.3.4.

There is a lack of asymmetry even when the $VA\cos\theta$ term is present. The symmetry of the initial pp state of course prevents such an asymmetry being present in the distribution of $\cos\theta$. To understand this in terms of Eq. (5.16), if we choose to measure $\cos\theta$ with respect to the direction of motion of the right-moving proton (which we call proton 1), then we are just as often defining $\theta = 0$ with respect to the direction of motion of a quark as we are an anti-quark.

To observe the asymmetry we introduce two other variables x_1^V and x_2^V

$$
\begin{aligned}
x_1^V &= \frac{1}{\sqrt{S}}(E_l + E_{\bar{l}} + p_l^z + p_{\bar{l}}^z) \\
x_2^V &= \frac{1}{\sqrt{S}}(E_l + E_{\bar{l}} - p_l^z - p_{\bar{l}}^z)
\end{aligned} \tag{5.17}
$$

and define the asymmetry

$$
\mathcal{A}_{ll}^V = \frac{N_{\cos\theta^V>0}^{x_1^V>x_2^V} + N_{\cos\theta^V<0}^{x_1^V<x_2^V} - N_{\cos\theta^V<0}^{x_1^V>x_2^V} - N_{\cos\theta^V>0}^{x_1^V<x_2^V}}{N_{\text{Tot}}} \,. \tag{5.18}
$$

This reintroduces an asymmetry by distinguishing between events which are boosted in the positive z direction and those boosted in the negative z direction. Consider the case when the $Y\overline{Y}$ rest frame is boosted in the positive z direction in the LAB frame. This means that $x_1 > x_2$, where x_1 and x_2 are the momentum fractions of the partons coming from proton 1 and proton 2 (left-moving) respectively. For $x_1 > x_2$,

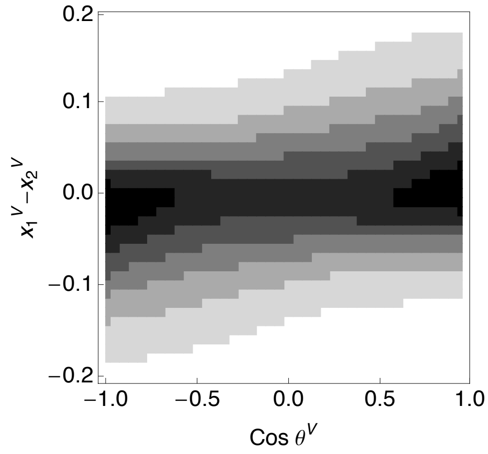

Figure 5.9: An observable asymmetry (spin half Y, $V = A = 1$) is obtained by plotting events as a function of $\cos\theta^V$ and $x_1^V - x_2^V$. Darker areas mean more events and the normalisation is arbitrary. We use the example masses for Y and Z, and show the distribution for the choice $M_X = 500\,\text{GeV}$. A larger value of M_X does squash this distribution towards $x_1^V - x_2^V = 0$, but does not change the value of the asymmetry $\mathcal{A}_{ll}^V$.

the parton distribution functions yield a higher probability for parton 1 to be a quark and parton 2 to be an antiquark, rather than the other way round. Overall there is a preference for the + sign in Eq. (5.16). We plot this visible asymmetry in the $(\cos\theta^V, x_1^V - x_2^V)$ plane in Fig. 5.9.

A proof is given in App. D that the variable $\mathcal{A}_{ll}^V$ is also independent of the mass of X, as well as $\cos\theta^V$. This is a nice feature for variables if they are to be used without any mass input. We now show how they can be used to determine the spin of Y once some idealised detector effects have been taken into account.

5.3.4 Collider simulation and differently boosted Ys

This collider simulation will be one skewed towards the theoretical end of the spectrum – in particular we consider only partonic processes and do not degrade the particles' momenta in any way. In reality many effects will lead to a smearing of the distributions – for example, detector resolution and the issue of low p_T initial

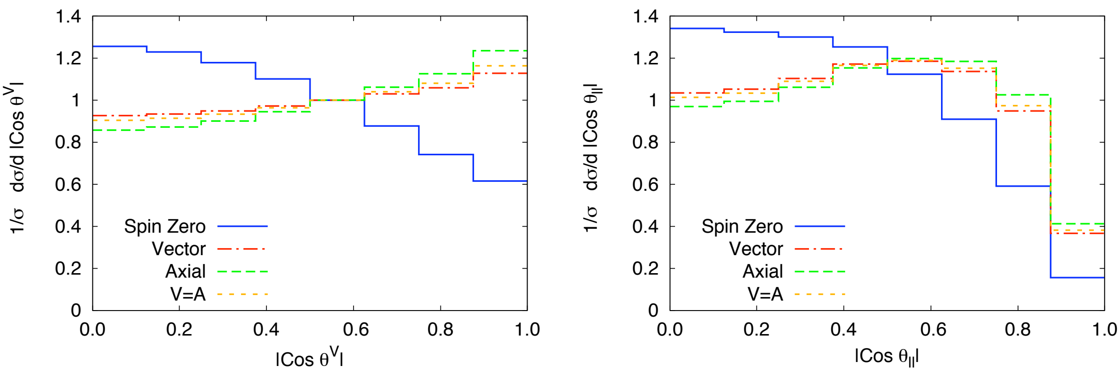

Figure 5.10: Comparing the normalised distributions of $\cos\theta^V$ (left) and $\cos\theta_{ll}$ (right), after applying the kinematic cuts outlined in the text, for the four different spin scenarios considered throughout this paper. We use the example masses for Y and Z, and here X is not closely degenerate in mass with Y – so long as this is the case, these curves are very insensitive to M_X (see text for details).

state radiation[11] – and we shall bear this in mind when making our conclusions. This approach is satisfactory because in [98] Barr carried out a realistic simulation beyond the scope of this thesis in the context of $\cos\theta_{ll}$ and found that this variable could be used at the LHC for spin measurement – we can draw upon the similarities with this work below.

We do however want to include detector effects which affect things at the parton level – this involves making kinematic cuts and studying the impact these have on the signal and the standard model backgrounds to this process. The cuts which we will employ are those of [98]: $p_{T,l_{\rm max}} > 40\,\text{GeV}$, $p_{T,l_{\rm min}} > 30\,\text{GeV}$, where $l_{\rm max(min)}$ is the lepton with the larger (smaller) transverse momentum; a cut on the rapidity of the leptons, $|\eta_l| < 2.5$; and a requirement for missing transverse momentum $p_{T,\rm miss} > 100\,\text{GeV}$. In addition, the following cuts are designed to remove the main standard model backgrounds: $M_{T2} > 100\,\text{GeV}$ and $M_{ll} > 150\,\text{GeV}$[12]. The main backgrounds

[11] By this we mean immeasurable initial state radiation (ISR), in the sense that no hard jet is observed in the event. It would be interesting to further study whether hard ISR in the event could be turned into something useful, as was done in [112].

[12] As the case we are considering involves an on-shell Z, an even higher cut on M_{T2} could in fact be used to reduce the WW background further.

Process	σ (fb)	$\mathcal{A}_{ll}^V$
WW	0.98(1)	-0.044(1)
ZZ	0.46(1)	0.22(1)
WZ	0.11(1)	0.042(1)

Table 5.2: Cross sections and values of $\mathcal{A}_{ll}^V$ for the main standard model background processes. Exactly two opposite sign, same flavour leptons (e or μ) satisfying the cuts described in the text are required, along with missing energy. These were produced at leading order using the POWHEG Box [10] at the 14 TeV LHC. Renormalisation and factorisation scales were set to the sum of the two vector boson masses in the process. The error shown is statistical only. In the ZZ case, only the two lepton, two neutrino final state was considered.

for this channel of opposite sign, same flavour leptons are WW and ZZ production (both decaying to $l^+l^-\nu\nu$), and we will also consider the WZ production background.

In Fig. 5.10 we plot normalised distributions for $\cos\theta^V$ and $\cos\theta_{ll}$, after these cuts have been made, for a spin zero Y and three types of spin half Y (vector coupling, axial coupling, and for couplings $V = A = 1$) at the 14 TeV LHC and with our example masses, $M_Y = 800\,\text{GeV}$ and $M_Z = 2.5\,\text{TeV}$. Because we are now cutting on the lepton momenta, a slight dependence on the value of the mass of X is introduced and so we quote that the distributions shown are with $M_X = 500\,\text{GeV}$. However, for M_X in the range $0 - 700\,\text{GeV}$ these distributions only experience changes at the few percent level. For M_X above this range, the signal cross section becomes very small as the cuts really start to have an effect; in fact for $M_X = 750\,\text{GeV}$ the M_{T2} cut entirely kills the signal[13]. If the case where X and Y are closely degenerate in mass is realised at the LHC, it will be very difficult to see the signal process above the standard model background anyway. The value for the asymmetry $\mathcal{A}_{ll}^V$ for a spin half Y with couplings $V = A = 1$ is found to be $\mathcal{A}_{ll}^V = 0.16(1)$, where the error is purely statistical.

The main standard model background cross sections can be found in Table 5.2,

[13]An animation which shows how these distributions change as M_X is varied from zero right up to the point at which the signal is killed by the cuts is available at [38].

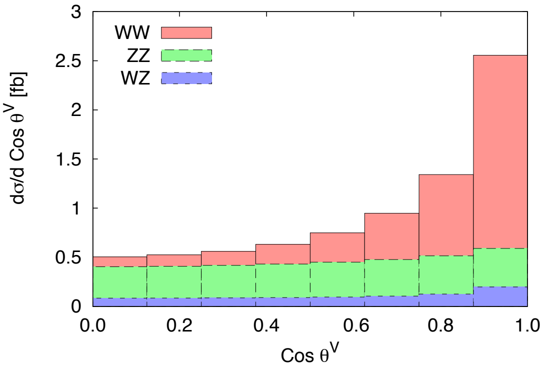

Figure 5.11: The $\cos\theta^V$ distributions of the main standard model backgrounds in the two opposite sign, same flavour leptons plus missing energy channel, produced in the POWHEG box for the 14 TeV LHC with the cuts described in the text.

along with values for the asymmetry, $\mathcal{A}^V_{ll}$. Their distributions in $\cos\theta^V$ – this time *not* normalised to unity – are plotted in Fig. 5.11. The importance of these backgrounds depends on the relative size of the beyond the standard model (BSM) process cross section. We include them to show their shape and magnitude. What was found in [98] was that they do not pose a major problem for using $\cos\theta_{ll}$ to determine spin for BSM cross sections of order a few tens of femtobarns (provided X and Y are not closely degenerate in mass). We would expect this conclusion to hold true for $\cos\theta^V$ as well. Unfortunately, the standard model backgrounds, especially ZZ production, yield rather large values of $\mathcal{A}^V_{ll}$. Since this variable has not been studied with realistic collider effects before, it is difficult to make a similar conclusion about the feasibility of observing and using this asymmetry at the LHC for spin determination, especially without a BSM cross section in mind.

We now proceed to make a statistical statement about the power of $\cos\theta^V$ in determining the spin of Y, which comes down to being able to tell apart the different distributions in Fig. 5.10. Following the method of reference [113], we estimate the number of events N needed to disfavour one spin configuration S in favour of another,

		Variable Used		
T	S	$\cos\theta$	$\cos\theta^V$	$\cos\theta_{ll}$
Vector	Spin Zero	28	153	179
Axial	Spin Zero	25	135	158
$V=A$	Spin Zero	21	106	124
Vector	Axial	1126	4008	4870
$V=A$	Axial	2487	8863	10794

Table 5.3: This table shows the number of events N needed to discredit the spin configuration S in favour of spin T using the distributions of the variables $\cos\theta^V$ and $\cos\theta_{ll}$ in figure 5.10. For reference, the number of events needed using (the immeasurable) $\cos\theta$ are included. The top half of the table shows comparisons between spin zero and spin half cases, and the bottom half shows some comparisons between different coupling spin half cases.

T, by a factor R as

$$N \sim \frac{\log R}{\mathrm{KL}(T,S)}\,, \tag{5.19}$$

where $\mathrm{KL}(T,S)$ is the *Kullback-Leibler distance* [114] between the two curves. The results of this test are shown in Table 5.3 for a value of $R = 1000$, where the number of events needed for distinguishing a spin zero Y from a spin half Y using $\cos\theta^V$ are compared with those needed using $\cos\theta_{ll}$. We also show results for distinguishing an axially coupling spin half Y from the other spin half cases (but not for telling apart a vector coupling and a mixed coupling Y – these distributions lie almost on top of each other in Fig. 5.10 and so will certainly be indistinguishable at the LHC). It can be seen that $\cos\theta^V$ performs around 20% better than $\cos\theta_{ll}$ in determining spin, and we would expect this to propagate through into a more realistic collider simulation. Secondly, using $\cos\theta^V$ to discriminate between the differently coupling spin half Ys requires enough events to most likely render it an unrealistic approach at the LHC. Because of this, it would be very interesting if a more detailed and realistic detector study proved that $\mathcal{A}_{ll}^V$ could be used to give information about the couplings of a spin half Y.

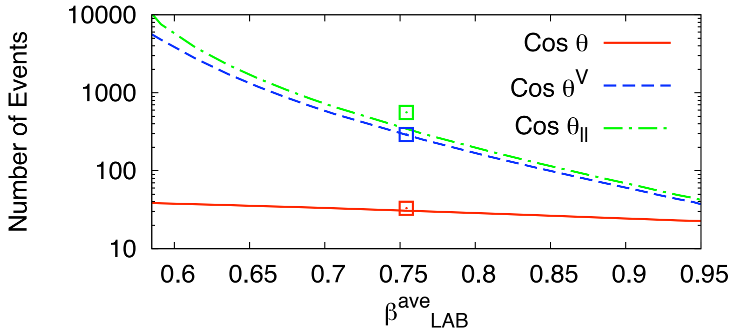

Figure 5.12: This plot shows the number of events needed to discredit the spin zero Y hypotheses in favour of a spin half (purely vector coupling) Y as a function of $\beta^{\text{ave}}_{\text{LAB}}$ – the average boost of Y in the LAB frame. This parameter is affected by the relative values of M_Z and M_Y, and is what is relevant for this method of spin determination (see text for details of how $\beta^{\text{ave}}_{\text{LAB}}$ is varied here). Curves for $\cos\theta^V$, $\cos\theta_{ll}$ and (the immeasurable) $\cos\theta$ are compared. The results for the case when $Z = Z^0$, the standard model weak boson, are plotted as open squares.

We move on to address the question of how things change when we pick different values for the mass of Y and Z. The relevant parameter which is affected by these masses is the boost of Y in the LAB frame, and in Fig. 5.12 we show how the number of events needed to disfavour a spin zero Y hypothesis in favour of a vector coupling spin half Y changes as the average value of this parameter, $\beta^{\text{ave}}_{\text{LAB}}$, varies. We choose to do this by keeping the mass of Y fixed at 800 GeV and varying the mass of Z. The lowest value of $\beta^{\text{ave}}_{\text{LAB}}$ is where we approach the limit of threshold production of $Y\overline{Y}$ in the Z rest frame. Shown also are results for the case when Z is the standard model Z^0 – these points lie off the other curves because in this case the shape of the β spectrum is different, owing to the fact that we are no longer considering an on-shell resonance decaying to $Y\overline{Y}$. As $\beta^{\text{ave}}_{\text{LAB}}$ tends towards one, we see the behaviour we would expect from Fig. D.1 – the number of events using the three different variables all tend towards the same value. This is because both $\cos\theta^V$ and $\cos\theta_{ll}$ approximate ever more closely the true $\cos\theta$ distribution, owing to the fact that the decay products from an increasingly relativistic Y will follow ever more closely the direction in which

Y travels. On the other hand, as $\beta^{\text{ave}}_{\text{LAB}}$ decreases, the number of events needed to determine Y's spin using $\cos\theta^V$ and $\cos\theta_{ll}$ rises exponentially, but we note that at the same time, $\cos\theta^V$ becomes increasingly better at determining spin than $\cos\theta_{ll}$. In the case where $Z = Z^0$, there is a factor of two gain in statistics in using $\cos\theta^V$. The number of events needed diverge at threshold production due to the fact we considered an isotropic decay of Y. An animation which shows the changes taking place in the $\cos\theta^V$ and $\cos\theta_{ll}$ distributions as $\beta^{\text{ave}}_{\text{LAB}}$ is varied is also available at the website [38].

Realistic collider effects will certainly increase the number of events indicated in Table 5.3 and Fig. 5.12, but so long as Y and $\overline{Y}$ are produced with a boost greater than ~ 0.75 then one might expect to be able to make a spin measurement (spin zero or spin half) with a few hundred events. This would require the BSM cross section to be at least around the 10 fb level. Furthermore, X and Y can't be too closely degenerate in mass if the signal is not to be lost in the standard model background. These conclusions are backed up by what was found in the particular cases studied in [98]. Finally, with reference to early spin measurement, we point out that the value of $R = 1000$ chosen in Eq. (5.19) could be relaxed somewhat which would give a (less certain) indication of the spin of Y with fewer events.

5.4 Chapter Summary

In this Chapter we presented phenomenology related to searches for BSM physics at the LHC. We used an implementation of WW and WZ production in the `POWHEG BOX` to investigate the study of ATGCs in these processes and to illustrate that, in the near future, the LHC will be able to either observe a deviation from the standard model prediction which would indicate the presence of new physics, or set new bounds on ATGCs. Next, we presented the NLO QCD corrections to the process

$pp \to W^+W^+ + 2j$, which gives rise to an exotic signature: two like-sign leptons, jets and missing energy. This is a standard model background to BSM searches at the LHC involving this signature. Including the NLO QCD corrections provides a more accurate theoretical description of this process, and we predicted that most events will contain two or more hard jets – about half of them with a third hard jet. Finally we discussed phenomenology relevant to the determination of the spin of new states, if they were to be produced at the LHC. We introduced two new variables which can be used to determine the spin of Y in the topology $pp \to Y\overline{Y} \to X\overline{X}l\bar{l}$, which do not take any input from the mass spectrum of X and Y and which are independent of the mass of X. We concluded that using $\cos\theta^V$ to discriminate between the two spin assignments considered could become possible after a few hundred events, without any knowledge either of the particle masses. Further study is needed to understand whether the asymmetry $\mathcal{A}_{ll}^V$ could be used when realistic collider effects are accounted for.

Chapter 6

Discussion and Conclusion

This thesis began in Chapter 2 with a summary of the recently proposed technique of D-dimensional generalised unitarity. We first showed how the OPP reduction method in D-dimensions can be used to express tensor integrals in a basis of scalar integrals and a rational part, following an efficient procedure to obtain the reduction coefficients. Then, following Ref. [3], we summarised how the technique can be adapted so it can be applied numerically to obtain cyclically ordered one-loop amplitudes through the evaluation of simple tree-level amplitudes in higher spatial dimensions. In Chapter 3 we outlined the general set-up of an NLO QCD calculation and described the Berends-Giele recursion relations used to obtain tree level amplitudes in this thesis. We presented a detailed account of the calculation of the NLO QCD corrections to $pp \to W^+W^- + 1j$, using D-dimensional generalised unitarity to obtain the one-loop amplitude, and showed some simple results for this process. This showed that D-dimensional generalised unitarity can be straightforwardly developed to deal with amplitudes involving two colourless particles. Chapter 4 contained phenomenological results involving two weak bosons which are relevant to Higgs boson physics at the LHC in the decay channel $H \to WW$. We calculated an NNLO contribution to the standard model background in the $H(\to WW) + 1j$ search bin which arises from gluon-gluon fusion, $gg \to W^+W^-g$, and showed that at the LHC it can cause a sizeable increase in the total cross section for $pp \to W^+W^- + 1j$. We revisited the previously known calculation of gluon-gluon fusion contribution to the background in the $H(\to WW) + 0j$ bin, $gg \to W^+W^-$, and found that with current ATLAS and CMS higgs search cuts, the contribution is no longer of the order of 30% of the NLO cross section as reported in Ref. [6, 7]. We concluded that the results for these NNLO contributions are highly sensitive to the experimental cuts applied. The dominant standard model background to the $H(\to WW) + 2j$ search bin at the LHC is $pp \to W^+W^- + 2j$, and we presented the calculation of the NLO QCD corrections, which were shown to provide a more theoretically reliable prediction for this process at the LHC. In Chapter 5 we considered BSM phenomenology related to the production of two weak bosons. We used an implementation of W^+W^- and WZ production in the `POWHEG BOX` to study anomalous tri-linear gauge couplings at the LHC, and showed that early results from this collider could improve upon the current bounds on their values. The NLO QCD corrections to the process $pp \to W^+W^+ + 2j$ were presented, which is a background to direct searches for BSM physics with a detector signature of like-sign leptons. We found that they improved the reliability of the theoretical description, and we predicted that most events would contain two or more hard jets, with about half of these having the third jet. Finally, we introduced two new variables and showed that they could be used to determine the spin of a new state without any mass input in a BSM topology where both mass and spin determination are difficult.

The NLO QCD calculations which form the main body of work in this thesis are typical of the many that have appeared over the course of the past few years. Taken together they have all but fulfilled the 2005, 2007 and 2009 Les Houches experimenter's wishes [20]. With the prospect of full automation of NLO QCD corrections in the near future, the frontier has turned to NNLO descriptions of the most relevant processes at the LHC, as well as to merging the NLO results with parton showers. However, there is still much phenomenology to perform with the available NLO results, and detailed comparison between theory and LHC experimental data as it comes out is exciting physics which will take place over the next few years.

In conclusion, we have found improved theoretical descriptions of processes at the LHC which involve the production of two weak bosons, and which were highlighted as being of experimental importance. This should help to improve future analyses of data at this experiment. We have presented phenomenological analyses at the LHC which are of interest to Higgs boson studies and BSM searches. This thesis is a small contribution to the many theoretical results and advances over many years which have already played crucial role in the discovery of the new 125-126 GeV state at the LHC. Ongoing research in this field will be central to maximising the potential for performing physics at CERN over the next twenty years.

Appendix A

Colour decomposition of amplitudes with a quark-antiquark pair and $(n-2)$ gluons

The colour decomposition we use for amplitudes involving a quark-antiquark pair and $(n-2)$ gluons is that of Ref. [31], the results of which we reproduce in this Appendix. At tree level

$$\mathcal{A}_n^{\text{tree}}(q_1, g_2, \ldots, g_{n-1}, \bar{q}_n) = g^{n-2} \sum_{\sigma \in S_{n-2}} (T^{a_{\sigma_2}} \cdots T^{a_{\sigma_{n-1}}})_{i_1}^{\;\bar{\imath}_n} A_n^{\text{tree}}(1_q, \sigma_2, \ldots, \sigma_{n-1}, n_{\bar{q}}) \,, \tag{A.1}$$

where $(T^a)_{i_1}^{\;\bar{\imath}_n}$ are $SU(N_c)$ matrices in the fundamental representation, g is the strong coupling constant, and the sum is over all permutations of $n-2$ objects, $\sigma(2, \ldots, n-1) = (\sigma_2, \ldots, \sigma_{n-1})$. This defines the primitive tree level amplitude A_n^{tree}, which can be directly obtained by computing cyclically ordered tree level amplitudes using colour

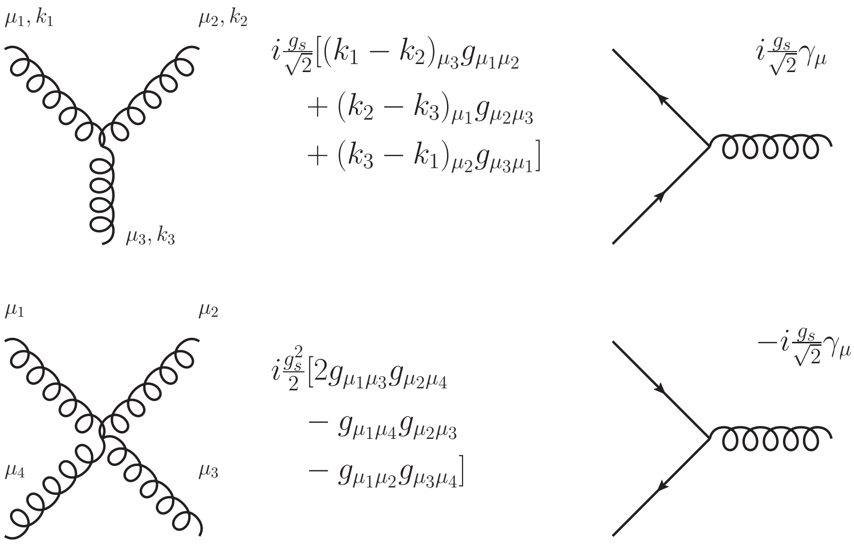

Figure A.1: Colour ordered Feynman rules used to construct the primitive amplitudes.

ordered Feynman rules (see Fig. A.1). At one-loop the colour decomposition is

$$\begin{aligned}
\mathcal{A}_n^{\text{1-loop}}(\bar{q}_1, q_2, g_3, \ldots, g_n) \;=\;& g^n \Bigg[\sum_{p=2}^{n} \sum_{\sigma\in S_{n-2}} (T^{x_2}T^{a_{\sigma_3}}\cdots T^{a_{\sigma_p}}T^{x_1})_{i_2}^{\;\bar{\imath}_1} (F^{a_{\sigma_{p+1}}}\cdots F^{a_{\sigma_n}})_{x_1x_2} \\
& \qquad\qquad \times A_n^{R,[1]}(1_{\bar{q}}, \sigma_{p+1}, \ldots, \sigma_n, 2_q, \sigma_3, \ldots, \sigma_p) \qquad \text{(A.2)} \\
& + \frac{n_f}{N_c} \sum_{j=1}^{n-1} \sum_{\sigma\in S_{n-2}/S_{n;j}} \text{Gr}_{n;j}^{(\bar{q}q)}(\sigma_3, \ldots, \sigma_n) A_{n;j}^{[1/2]}(1_{\bar{q}}, 2_q; \sigma_3, \ldots, \sigma_n) \Bigg],
\end{aligned}$$

where $(F^a)_{bc} \equiv if^{bac}$ is a $SU(N_c)$ generator in the adjoint representation; where for $p = n$ the product of generators in the adjoint representation reduces to the identity, $(F\cdots F)_{x_1x_2} \to \delta_{x_1x_2}$; with the colour structures $\text{Gr}_{n;j}^{(\bar{q}q)}$ defined as

$$\begin{aligned}
\text{Gr}_{n;1}^{(\bar{q}q)}(3, \ldots, n) &= N_c (T^{a_3}\cdots T^{a_n})_{i_2}^{\;\bar{\imath}_1}, \\
\text{Gr}_{n;2}^{(\bar{q}q)}(3; 4, \ldots, n) &= 0, \\
\text{Gr}_{n;j}^{(\bar{q}q)}(3, \ldots, j+1; j+2, \ldots, n) &= \text{tr}(T^{a_3}\cdots T^{a_{j+1}})(T^{a_{j+2}}\cdots T^{a_n})_{i_2}^{\;\bar{\imath}_1}, \qquad j = 3, \ldots, n-2, \\
\text{Gr}_{n;n-1}^{(\bar{q}q)}(3, \ldots, n) &= \text{tr}(T^{a_3}\cdots T^{a_n})\,\delta_{i_2}^{\;\bar{\imath}_1}, \qquad \text{(A.3)}
\end{aligned}$$

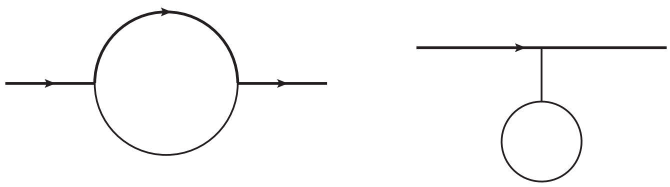

Figure A.2: Left primitive amplitudes, where the external quark line (in bold) turns left when entering the loop or passing the loop.

and where $S_{n;j} = \mathbb{Z}_{j-1}$ is the subgroup of S_{n-2} that leaves $\mathrm{Gr}^{(\bar{q}q)}_{n;j}$ invariant; with n_f the number of fermions propagating in a closed fermion loop; and where

$$\begin{aligned} A^{[1/2]}_{n;1}(1_{\bar{q}}, 2_q, 3, \ldots, n) &= A^{L,[1/2]}_n(1_{\bar{q}}, 2_q, 3, \ldots, n), \\ A^{[1/2]}_{n;j}(1_{\bar{q}}, 2_q; 3, \ldots, j+1; j+2, j+3, \ldots, n) &= (-1)^j \sum_{\sigma \in \mathrm{COP}\{\alpha\}\{\beta\}} A^{R,[1/2]}_n(\sigma(1_{\bar{q}}, 2_q, 3, \ldots, n)), \end{aligned} \tag{A.4}$$

where $\alpha_i \in \{\alpha\} \equiv \{j+1, j, \ldots, 4, 3\}$ and $\beta_i \in \{\beta\} \equiv \{1, 2, j+2, j+3, \ldots, n-1, n\}$, and $\mathrm{COP}\{\alpha\}\{\beta\}$ is the set of all permutations of $\{1, 2, \ldots, n\}$ with 1 held fixed that preserve the cyclic ordering of the α_i within $\{\alpha\}$ and the β_i within $\{\beta\}$, while allowing for all possible relative orderings of the α_i with respect to the β_i [1]. This defines the primitive one-loop amplitudes $A^{R,[1]}_n$, $A^{R,[1/2]}_n$ and $A^{L,[1/2]}_n$, where the superscript $[j]$ denotes the spin of the particles in the loop when the external quark line is not in the loop. The primitive amplitudes $A^{R,[1]}_n$ can be directly obtained by using the colour ordered Feynman rules and computing cyclically ordered one-loop diagrams which involve a gluon in the loop and where when following the direction of the quark line, it turns to the right either as it enters the loop or as it passes the loop – this is the origin of the superscript R. Similarly the primitive amplitudes $A^{R(L),[1/2]}_n$ can be directly obtained by using the colour ordered Feynman rules and computing cyclically

[1]E.g. for $\{\alpha\} = \{4,3\}$ and $\{\beta\} = \{1,2,5\}$, then $COP\{\alpha\}\{\beta\} =$

$$\begin{aligned} &(1,2,5,4,3), \quad (1,2,4,5,3), \quad (1,2,4,3,5), \quad (1,4,2,5,3), \quad (1,4,2,3,5), \quad (1,4,3,2,5), \\ &(1,2,5,3,4), \quad (1,2,3,5,4), \quad (1,2,3,4,5), \quad (1,3,2,5,4), \quad (1,3,2,4,5), \quad (1,3,4,2,5). \end{aligned}$$

ordered one-loop diagrams which only involve quarks in the loop and where, when following the direction of the quark line, it turns to the right (left) as it passes the loop. Left and right primitive amplitudes are related by the reflection identity

$$A_n^{R,[j]}(1_{\bar{q}}, 3, 4, \ldots, 2_q, \ldots, n-1, n) = (-1)^n A_n^{L,[j]}(1_{\bar{q}}, n, n-1, \ldots, 2_q, \ldots, 4, 3)\,. \quad \text{(A.5)}$$

In this thesis we work entirely in terms of left handed amplitudes (see Fig. A.2).

Appendix B

Singular terms of one-loop QCD helicity amplitudes

In this Appendix we reproduce results from Ref. [42] for the singular terms in one-loop amplitudes in D-dimensional regularisation, where $D = 4 - 2\epsilon$. There is an UV divergence which is cancelled by the $\overline{\mathrm{MS}}$ counter term

$$\mathcal{A}^{\mathrm{UV}} = -\frac{(n-2)(4\pi)^{\epsilon}}{2\epsilon\Gamma(1-\epsilon)} \left(\frac{g}{4\pi}\right)^{2} \beta_0 \mathcal{A}^{\mathrm{tree}}\,, \tag{B.1}$$

where n is the number of external legs, $\beta_0 = (11N_c - 2N_f)/3$, where N_c is the number of colours and N_f the number of fermions, g is the renormalized coupling constant, and Γ is the gamma function. IR singularities occur when the loop momentum becomes collinear to one of the external particles and are given by

$$\mathcal{A}^{\mathrm{col}} = -\left(\frac{g}{4\pi}\right)^{2} \sum_{a}^{n} \frac{\gamma(a)}{\epsilon} \mathcal{A}^{\mathrm{tree}} \tag{B.2}$$

where the sum is over all a external quarks and gluons, with $\gamma(g) = (11N_c - 2N_f)/6$ and $\gamma(q) = 3(N_c^2 - 1)/4N_c$. There are also IR singularities when an internal gluon connecting two external legs goes soft, given by

$$\mathcal{A}^{\text{soft}}(2 \to n-2)_{c_1 c_2 .. c_n} = \sum_{i<j} \left(\frac{g}{4\pi}\right)^2 c_\Gamma \frac{1}{\epsilon^2} \left(-\frac{\mu^2}{s_{ij}}\right)^\epsilon \sum_{a, c'_i c'_j} t^a_{c_i c'_i} t^a_{c_j c'_j} \mathcal{A}^{\text{tree}}(2 \to n-2)_{c_1 .. c'_i .. c'_j .. c_n} \, , \tag{B.3}$$

where $t^a_{c_i c'_i}$ is the $SU(3)$ colour generator matrix for the representation of the line i. For outgoing partons, t^a_{ij} is $(1/2)T^a_{ij}$ for a quark, $-(1/2)(T^a_{ij})^*$ for an antiquark, and if^{aij} for a gluon. For incoming partons, t^a_{ij} is $-(1/2)(T^a_{ij})^*$ for a quark, $(1/2)T^a_{ij}$ for an antiquark, and if^{aij} for a gluon. The quantity $s_{ij} = (p_i + p_j)^2$, and the factor c_Γ is given by

$$c_\Gamma = (4\pi)^\epsilon \frac{\Gamma^2(1-\epsilon)\Gamma(1+\epsilon)}{\Gamma(1-2\epsilon)} \, . \tag{B.4}$$

Appendix C

Colour and helicity space vectors for the CS dipole definitions

In this Appendix we reproduce results from Ref. [5] which defines the notation used in Eqs. (3.20), (3.21) and (3.24) in Sec. 3.3.

A tree-level matrix element with m QCD partons has the structure

$$\mathcal{M}_m^{c_1,..,c_m;s_1,..,s_m}(p_1,\ldots,p_m) \tag{C.1}$$

where the c_i are $SU(N_c)$ the colour indices, the s_i are the spin indices, and the p_i are the momenta of the partons. A basis in colour + helicity space can be introduced, $\{|c_1,\ldots,c_m> \otimes |s_1,\ldots,s_m>\}$, so that

$$\mathcal{M}_m^{c_1,..,c_m;s_1,..,s_m}(p_1,\ldots,p_m) \equiv \Big(< c_1,\ldots,c_m| \otimes < s_1,\ldots,s_m| \Big) |1,\ldots,m>_m \; . \tag{C.2}$$

This defines a vector $|1,\ldots,m>_m$ in colour + helicity space. The colour charge operator $\boldsymbol{T}_i$ is associated with the emission of a gluon from a parton i, and provides the colour correlations in Eq. (3.21)

$$
\begin{aligned}
&{}_m < 1,\ldots,m|\boldsymbol{T}_i \cdot \boldsymbol{T}_k|1,\ldots,m >_m \\
&= \left[\mathcal{M}_m^{a_1..b_i..b_k..a_m}(p_1,\ldots,p_m)\right]^* t^c_{b_i a_i} t^c_{b_k a_k} \mathcal{M}_m^{a_1..a_i..a_k..a_m}(p_1,\ldots,p_m)\,,
\end{aligned}
\tag{C.3}
$$

where $t^a_{cb} = if_{cab}$ if the emitting particle i is a gluon, $t^a_{\alpha\beta} = T^a_{\alpha\beta}$ if i is a quark, and $t^a_{\alpha\beta} = -T^a_{\beta\alpha}$ if i is an antiquark, The colour charges satisfy $\boldsymbol{T}_i^2 = C_i$, the Casimir operator: $C_i = C_A = N_c$ if i is a gluon and $C_i = C_F = (N_c^2-1)/2N_c$ if i is a quark or an antiquark.

The *splitting function* $\boldsymbol{V}^a_{ij}$ appearing in Eq. (3.21) (and similar splitting functions contained within other dipoles) are matrices in helicity space, and can all be found in Ref. [5] – to give an example which appears in Table 3.1 , the splitting function contained within the dipole $\mathcal{D}^{q_1}_{\bar{q}_3 q_4}$ is $\boldsymbol{V}^{q_1}_{\bar{q}_3 q_4}$ and is defined by

$$
< \mu|\boldsymbol{V}^{q_1}_{\bar{q}_3 q_4}|\nu >= 8\pi\mu^{2\epsilon}\alpha_S T_R\left[-g^{\mu\nu} - \frac{2}{p_3 p_4}(\tilde{z}_3 p_3^\mu - \tilde{z}_4 p_4^\mu)(\tilde{z}_3 p_3^\nu - \tilde{z}_4 p_4^\nu)\right], \tag{C.4}
$$

where α_S is the strong coupling constant, T_R is the normalisation of the colour matrices, $\mathrm{Tr}[T^a T^b] = T_R \delta^{ab}$, and where (see also Eq. 3.23)

$$
\tilde{z}_3 = \frac{p_3 \cdot \tilde{p}_a}{\tilde{p}_{34} \cdot \tilde{p}_a}, \quad \tilde{z}_4 = 1 - \tilde{z}_3\,. \tag{C.5}
$$

Appendix D

Mass independence of spin determination variables $\cos\theta^V$ and $\mathcal{A}_{ll}^V$

We begin by showing that the angle between l and Y's direction of motion in any frame of reference is independent of the mass of X. The way in which $\cos\theta^V$ and $\mathcal{A}_{ll}^V$ are independent of M_X follows easily from this observation.

Consider the decay of Y in its own rest frame into X and l. Here we write the momentum of l as

$$p_l^* = \begin{pmatrix} E^* \\ 0 \\ E^* \sin\theta^* \\ E^* \cos\theta^* \end{pmatrix}, \tag{D.1}$$

where $E^* = (M_Y^2 - M_X^2)/2M_Y$. Now boost this to the frame in which Y travels with momentum $p_z = M_Y\gamma'\beta'$ along the z axis (the primes are to distinguish these quantities from those used in the centre of mass frame of Y and $\overline{Y}$) to obtain

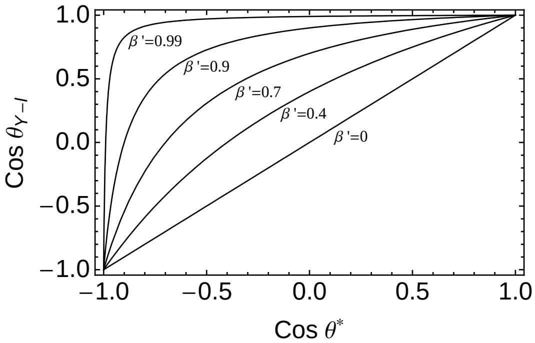

Figure D.1: Plotting the relationship (D.3) between $\cos\theta_{Y-l}$ and $\cos\theta^*$ (both defined in the text) for various values of β'. A flat distribution in the centre of mass angle $\cos\theta^*$ leads to a distribution in $\cos\theta_{Y-l}$ which becomes increasingly polarised towards $\cos\theta_{Y-l} = 1$ as Y becomes more boosted.

$$p_l = \begin{pmatrix} \gamma' E^*(1+\beta'\cos\theta^*) \\ 0 \\ E^*\sin\theta^* \\ \gamma' E^*(\beta' + \cos\theta^*) \end{pmatrix} . \tag{D.2}$$

We can compute the cosine of the angle between l and Y's direction of motion

$$\cos\theta_{Y-l} = \frac{\gamma'(\beta' + \cos\theta^*)}{\left(\sin^2\theta^* + \gamma'^2(\beta' + \cos\theta^*)^2\right)^{1/2}} . \tag{D.3}$$

This result does not depend on our choice of the z-axis, and is true in a general frame of reference. There are two things worth pointing out. Firstly, as β' becomes large, the lepton really does start to track the direction of its parent's motion very well, as illustrated in figure D.1. This is how the variables introduced in Sec. 5.3 can pick up on the information about the polar production angle of Y. Secondly, E^* has cancelled in this expression and so we see that this angle is independent of the mass of X.

The way in which E^* cancels here points us to the reason why $\cos\theta^V$ and $\mathcal{A}_{ll}^V$ are independent of M_X. The above result tells us that in any frame of reference, the momenta of l and $\bar{l}$ take the form $p_l = E_l(1, \hat{\mathbf{n}})$ and $p_{\bar{l}} = E_{\bar{l}}(1, \hat{\mathbf{m}})$, where $\hat{\mathbf{n}}$ and $\hat{\mathbf{m}}$ are unit vectors which have a distribution unaffected by the value of M_X. All dependence on M_X is contained within the overall factors E_l and $E_{\bar{l}}$ which are both proportional to $\Delta M^2 = (M_Y^2 - M_X^2)$. It follows then that *any dimensionless observable in any reference frame must be independent of the mass of X if the only dimensionfull inputs are components of the leptons' four momenta.* The common factor of ΔM^2 has to cancel. This completes the proof that $\cos\theta^V$ is independent of M_X. We also point out that $\cos\theta_{ll}$, along with many other dimensionless variables which have been studied in the past such as $\Delta\phi_{ll}$, $\cos\theta_l - \cos\theta_{\bar{l}}$, etc. all enjoy this property too.

Turning to the asymmetry $\mathcal{A}_{ll}^V$, we now have a dimensionfull input which is not a lepton momentum component: $\sqrt{S}$. We can see from equation (5.17) that $x_1^V - x_2^V$ is proportional to the mass difference ΔM^2, so that the distribution shown in Fig. 5.9 gets squashed towards $x_1^V - x_2^V = 0$ for larger M_X. However, the value of M_X has no effect on the sign of $x_1^V - x_2^V$, and so with the result for $\cos\theta^V$ we conclude that $\mathcal{A}_{ll}^V$ is also independent of M_X.

Bibliography

[1] **ATLAS Collaboration** Collaboration, G. Aad *et. al.*, *Observation of a new particle in the search for the Standard Model Higgs boson with the ATLAS detector at the LHC*, *Phys.Lett.B* (2012) [arXiv:1207.7214].

[2] **CMS Collaboration** Collaboration, S. Chatrchyan *et. al.*, *Observation of a new boson at a mass of 125 GeV with the CMS experiment at the LHC*, *Phys.Lett.B* (2012) [arXiv:1207.7235].

[3] W. T. Giele, Z. Kunszt, and K. Melnikov, *Full one-loop amplitudes from tree amplitudes*, *JHEP* **0804** (2008) 049, [arXiv:0801.2237].

[4] J. M. Campbell, J. Huston, and W. Stirling, *Hard Interactions of Quarks and Gluons: A Primer for LHC Physics*, *Rept.Prog.Phys.* **70** (2007) 89, [hep-ph/0611148].

[5] S. Catani and M. Seymour, *A General algorithm for calculating jet cross-sections in NLO QCD*, *Nucl.Phys.* **B485** (1997) 291–419, [hep-ph/9605323].

[6] T. Binoth, M. Ciccolini, N. Kauer, and M. Kramer, *Gluon-induced WW background to Higgs boson searches at the LHC*, *JHEP* **0503** (2005) 065, [hep-ph/0503094].

[7] T. Binoth, M. Ciccolini, N. Kauer, and M. Kramer, *Gluon-induced W-boson pair production at the LHC*, *JHEP* **0612** (2006) 046, [hep-ph/0611170].

[8] T. Melia, K. Melnikov, R. Rontsch, M. Schulze, and G. Zanderighi, *Gluon fusion contribution to W+W- + jet production*, *JHEP* **1208** (2012) 115, [arXiv:1205.6987].

[9] T. Melia, K. Melnikov, R. Rontsch, and G. Zanderighi, *NLO QCD corrections for W^+W^- pair production in association with two jets at hadron colliders*, *Phys.Rev.* **D83** (2011) 114043, [arXiv:1104.2327].

[10] T. Melia, P. Nason, R. Rontsch, and G. Zanderighi, *W+W-, WZ and ZZ production in the POWHEG BOX*, *JHEP* **1111** (2011) 078, [arXiv:1107.5051].

[11] T. Melia, K. Melnikov, R. Rontsch, and G. Zanderighi, *Next-to-leading order QCD predictions for W^+W^+jj production at the LHC*, *JHEP* **1012** (2010) 053, [`arXiv:1007.5313`].

[12] T. Melia, *Spin before mass at the LHC*, *JHEP* **1201** (2012) 143, [`arXiv:1110.6185`].

[13] C. Buttar, S. Dittmaier, V. Drollinger, S. Frixione, A. Nikitenko, *et. al.*, *Les houches physics at TeV colliders 2005, standard model and Higgs working group: Summary report*, `hep-ph/0604120`.

[14] R. Britto, F. Cachazo, and B. Feng, *Generalized unitarity and one-loop amplitudes in N=4 super-Yang-Mills*, *Nucl.Phys.* **B725** (2005) 275–305, [`hep-th/0412103`].

[15] G. Ossola, C. G. Papadopoulos, and R. Pittau, *Reducing full one-loop amplitudes to scalar integrals at the integrand level*, *Nucl.Phys.* **B763** (2007) 147–169, [`hep-ph/0609007`].

[16] S. Dittmaier, S. Kallweit, and P. Uwer, *NLO QCD corrections to WW+jet production at hadron colliders*, *Phys.Rev.Lett.* **100** (2008) 062003, [`arXiv:0710.1577`].

[17] J. M. Campbell, R. K. Ellis, and G. Zanderighi, *Next-to-leading order predictions for $WW + 1$ jet distributions at the LHC*, *JHEP* **0712** (2007) 056, [`arXiv:0710.1832`].

[18] **NLO Multileg Working Group** Collaboration, Z. Bern *et. al.*, *The NLO multileg working group: Summary report*, `arXiv:0803.0494`.

[19] **SM and NLO Multileg Working Group** Collaboration, J. Andersen *et. al.*, *The SM and NLO Multileg Working Group: Summary report*, `arXiv:1003.1241`.

[20] **SM AND NLO MULTILEG and SM MC Working Groups** Collaboration, J. Alcaraz Maestre *et. al.*, *The SM and NLO Multileg and SM MC Working Groups: Summary Report*, `arXiv:1203.6803`.

[21] V. Hirschi, R. Frederix, S. Frixione, M. V. Garzelli, F. Maltoni, *et. al.*, *Automation of one-loop QCD corrections*, *JHEP* **1105** (2011) 044, [`arXiv:1103.0621`].

[22] G. Bevilacqua, M. Czakon, M. Garzelli, A. van Hameren, A. Kardos, *et. al.*, *HELAC-NLO*, `arXiv:1110.1499`.

[23] G. Cullen, N. Greiner, G. Heinrich, G. Luisoni, P. Mastrolia, *et. al.*, *Automated one-loop calculations with GoSam*, `arXiv:1201.2782`.

[24] F. Cascioli, P. Maierhofer, and S. Pozzorini, *Scattering Amplitudes with Open Loops*, *Phys.Rev.Lett.* **108** (2012) 111601, [arXiv:1111.5206].

[25] G. Passarino and M. Veltman, *One Loop Corrections for e+ e- Annihilation Into mu+ mu- in the Weinberg Model*, *Nucl.Phys.* **B160** (1979) 151.

[26] R. K. Ellis, Z. Kunszt, K. Melnikov, and G. Zanderighi, *One-loop calculations in quantum field theory: from Feynman diagrams to unitarity cuts*, arXiv:1105.4319.

[27] R. Britto, F. Cachazo, B. Feng, and E. Witten, *Direct proof of tree-level recursion relation in Yang-Mills theory*, *Phys.Rev.Lett.* **94** (2005) 181602, [hep-th/0501052].

[28] A. Lazopoulos, *Precise evaluation of the Cut Constructible part of one loop amplitudes within D-dimensional unitarity*, arXiv:0911.5241.

[29] J. M. Campbell, R. K. Ellis, and G. Zanderighi, *Next-to-Leading order Higgs + 2 jet production via gluon fusion*, *JHEP* **0610** (2006) 028, [hep-ph/0608194].

[30] M. L. Mangano, *The Color Structure of Gluon Emission*, *Nucl.Phys.* **B309** (1988) 461.

[31] V. Del Duca, L. J. Dixon, and F. Maltoni, *New color decompositions for gauge amplitudes at tree and loop level*, *Nucl.Phys.* **B571** (2000) 51–70, [hep-ph/9910563].

[32] M. L. Mangano and S. J. Parke, *Multiparton amplitudes in gauge theories*, *Phys.Rept.* **200** (1991) 301–367, [hep-th/0509223].

[33] L. J. Dixon, *Calculating scattering amplitudes efficiently*, hep-ph/9601359.

[34] L. Landau, *On analytic properties of vertex parts in quantum field theory*, *Nucl.Phys.* **13** (1959) 181–192.

[35] R. Cutkosky, *Singularities and discontinuities of Feynman amplitudes*, *J.Math.Phys.* **1** (1960) 429–433.

[36] Z. Bern, A. De Freitas, L. J. Dixon, and H. Wong, *Supersymmetric regularization, two loop QCD amplitudes and coupling shifts*, *Phys.Rev.* **D66** (2002) 085002, [hep-ph/0202271].

[37] S. Dittmaier, S. Kallweit, and P. Uwer, *NLO QCD corrections to pp/ppbar to WW+jet+X including leptonic W-boson decays*, *Nucl.Phys.* **B826** (2010) 18–70, [arXiv:0908.4124].

[38] http://www-thphys.physics.ox.ac.uk/people/TomMelia/tommelia.html.

[39] G. Altarelli and G. Parisi, *Asymptotic Freedom in Parton Language*, *Nucl.Phys.* **B126** (1977) 298.

[40] F. A. Berends and W. Giele, *Recursive Calculations for Processes with n Gluons*, *Nucl.Phys.* **B306** (1988) 759.

[41] W. Giele and G. Zanderighi, *On the Numerical Evaluation of One-Loop Amplitudes: The Gluonic Case*, *JHEP* **0806** (2008) 038, [arXiv:0805.2152].

[42] Z. Kunszt, A. Signer, and Z. Trocsanyi, *Singular terms of helicity amplitudes at one loop in QCD and the soft limit of the cross-sections of multiparton processes*, *Nucl.Phys.* **B420** (1994) 550–564, [hep-ph/9401294].

[43] Z. Nagy and Z. Trocsanyi, *Next-to-leading order calculation of four jet observables in electron positron annihilation*, *Phys.Rev.* **D59** (1999) 014020, [hep-ph/9806317].

[44] Z. Nagy, *Next-to-leading order calculation of three jet observables in hadron hadron collision*, *Phys.Rev.* **D68** (2003) 094002, [hep-ph/0307268].

[45] J. M. Campbell and R. K. Ellis, *Radiative corrections to Z b anti-b production*, *Phys.Rev.* **D62** (2000) 114012, [hep-ph/0006304].

[46] J. Alwall, P. Demin, S. de Visscher, R. Frederix, M. Herquet, *et. al.*, *MadGraph/MadEvent v4: The New Web Generation*, *JHEP* **0709** (2007) 028, [arXiv:0706.2334].

[47] P. Nogueira, *Automatic Feynman graph generation*, *J.Comput.Phys.* **105** (1993) 279–289.

[48] J. Vermaseren http://www.nikhef.nl/ form/.

[49] A. Martin, W. Stirling, R. Thorne, and G. Watt, *Parton distributions for the LHC*, *Eur.Phys.J.* **C63** (2009) 189–285, [arXiv:0901.0002].

[50] M. Cacciari, G. P. Salam, and G. Soyez, *The Anti-k(t) jet clustering algorithm*, *JHEP* **0804** (2008) 063, [arXiv:0802.1189].

[51] M. Cacciari, G. P. Salam, and G. Soyez, *FastJet User Manual*, *Eur.Phys.J.* **C72** (2012) 1896, [arXiv:1111.6097].

[52] **LEP Working Group for Higgs boson searches, ALEPH Collaboration, DELPHI Collaboration, L3 Collaboration, OPAL Collaboration** Collaboration, R. Barate *et. al.*, *Search for the standard model Higgs boson at LEP*, *Phys.Lett.* **B565** (2003) 61–75, [hep-ex/0306033].

[53] **Tevatron New Physics Higgs Working Group, CDF Collaboration, D0 Collaboration** Collaboration, C. Group, D. Collaborations, the Tevatron New Physics, and H. Working, *Updated Combination of CDF and D0 Searches for Standard Model Higgs Boson Production with up to 10.0 fb^{-1} of Data*, arXiv:1207.0449.

[54] G. Klamke and D. Zeppenfeld, *Higgs plus two jet production via gluon fusion as a signal at the CERN LHC*, *JHEP* **0704** (2007) 052, [hep-ph/0703202].

[55] S. Dittmaier, S. Dittmaier, C. Mariotti, G. Passarino, R. Tanaka, *et. al.*, *Handbook of LHC Higgs Cross Sections: 2. Differential Distributions*, arXiv:1201.3084.

[56] R. V. Harlander and W. B. Kilgore, *Next-to-next-to-leading order Higgs production at hadron colliders*, *Phys.Rev.Lett.* **88** (2002) 201801, [hep-ph/0201206].

[57] C. Anastasiou and K. Melnikov, *Higgs boson production at hadron colliders in NNLO QCD*, *Nucl.Phys.* **B646** (2002) 220–256, [hep-ph/0207004].

[58] D. de Florian, M. Grazzini, and Z. Kunszt, *Higgs production with large transverse momentum in hadronic collisions at next-to-leading order*, *Phys.Rev.Lett.* **82** (1999) 5209–5212, [hep-ph/9902483].

[59] V. Ravindran, J. Smith, and W. Van Neerven, *Next-to-leading order QCD corrections to differential distributions of Higgs boson production in hadron hadron collisions*, *Nucl.Phys.* **B634** (2002) 247–290, [hep-ph/0201114].

[60] C. J. Glosser and C. R. Schmidt, *Next-to-leading corrections to the Higgs boson transverse momentum spectrum in gluon fusion*, *JHEP* **0212** (2002) 016, [hep-ph/0209248].

[61] J. M. Campbell, R. K. Ellis, and C. Williams, *Hadronic production of a Higgs boson and two jets at next-to-leading order*, *Phys.Rev.* **D81** (2010) 074023, [arXiv:1001.4495].

[62] T. Figy, C. Oleari, and D. Zeppenfeld, *Next-to-leading order jet distributions for Higgs boson production via weak boson fusion*, *Phys.Rev.* **D68** (2003) 073005, [hep-ph/0306109].

[63] E. L. Berger and J. M. Campbell, *Higgs boson production in weak boson fusion at next-to-leading order*, *Phys.Rev.* **D70** (2004) 073011, [hep-ph/0403194].

[64] J. M. Campbell and R. K. Ellis, *An Update on vector boson pair production at hadron colliders*, *Phys.Rev.* **D60** (1999) 113006, [hep-ph/9905386].

[65] J. M. Campbell, R. K. Ellis, and C. Williams, *Gluon-Gluon Contributions to W+ W- Production and Higgs Interference Effects*, *JHEP* **1110** (2011) 005, [arXiv:1107.5569].

[66] **ATLAS Collaboration** Collaboration, G. Aad *et. al.*, *Search for the Standard Model Higgs boson in the $H \to WW(*) \to l\ nu\ l\ nu$ decay mode with 4.7 /fb of ATLAS data at sqrt(s) = 7 TeV*, *Phys. Lett.* **B716** (2012) 62–81, [arXiv:1206.0756].

[67] M. Dittmar and H. K. Dreiner, *How to find a Higgs boson with a mass between 155-GeV - 180-GeV at the LHC*, *Phys.Rev.* **D55** (1997) 167–172, [`hep-ph/9608317`].

[68] N. Greiner, G. Heinrich, P. Mastrolia, G. Ossola, T. Reiter, *et. al.*, *NLO QCD corrections to the production of W+ W- plus two jets at the LHC*, *Phys.Lett.* **B713** (2012) 277–283, [`arXiv:1202.6004`].

[69] G. Bevilacqua, M. Czakon, A. van Hameren, C. G. Papadopoulos, and M. Worek, *Complete off-shell effects in top quark pair hadroproduction with leptonic decay at next-to-leading order*, *JHEP* **1102** (2011) 083, [`arXiv:1012.4230`].

[70] A. Denner, S. Dittmaier, S. Kallweit, and S. Pozzorini, *NLO QCD corrections to WWbb production at hadron colliders*, *Phys.Rev.Lett.* **106** (2011) 052001, [`arXiv:1012.3975`].

[71] K. Melnikov and M. Schulze, *Top quark spin correlations at the Tevatron and the LHC*, *Phys.Lett.* **B700** (2011) 17–20, [`arXiv:1103.2122`].

[72] B. Jager, C. Oleari, and D. Zeppenfeld, *Next-to-leading order QCD corrections to W+W- production via vector-boson fusion*, *JHEP* **0607** (2006) 015, [`hep-ph/0603177`].

[73] **ALEPH Collaboration, DELPHI Collaboration, L3 Collaboration, OPAL Collaboration, LEP Electroweak Working Group** Collaboration, J. Alcaraz *et. al.*, *A Combination of preliminary electroweak measurements and constraints on the standard model*, `hep-ex/0612034`.

[74] **CDF Collaboration** Collaboration, T. Aaltonen *et. al.*, *Measurement of the W+ W- Production Cross Section and Search for Anomalous WW gamma and WWZ Couplings in p p-bar Collisions at s**(1/2) = 1.96-TeV*, *Phys.Rev.Lett.* **104** (2010) 201801, [`arXiv:0912.4500`].

[75] **D0 Collaboration** Collaboration, V. Abazov *et. al.*, *Measurement of the WW production cross section with dilepton final states in p anti-p collisions at s**(1/2) = 1.96-TeV and limits on anomalous trilinear gauge couplings*, *Phys.Rev.Lett.* **103** (2009) 191801, [`arXiv:0904.0673`].

[76] **D0 Collaboration** Collaboration, V. Abazov *et. al.*, *Measurement of trilinear gauge boson couplings from WW + WZ → l nu j j events in p anti-p collisions at s**(1/2) = 1.96 TeV*, *Phys.Rev.* **D80** (2009) 053012, [`arXiv:0907.4398`].

[77] C. Degrande, N. Greiner, W. Kilian, O. Mattelaer, H. Mebane, *et. al.*, *Effective Field Theory: A Modern Approach to Anomalous Couplings*, `arXiv:1205.4231`.

[78] K. Hagiwara, R. Peccei, D. Zeppenfeld, and K. Hikasa, *Probing the Weak Boson Sector in e+ e- → W+ W-*, *Nucl.Phys.* **B282** (1987) 253.

[79] K. Hagiwara, S. Ishihara, R. Szalapski, and D. Zeppenfeld, *Low-energy effects of new interactions in the electroweak boson sector*, *Phys.Rev.* **D48** (1993) 2182–2203.

[80] P. Nason, *A New method for combining NLO QCD with shower Monte Carlo algorithms*, *JHEP* **0411** (2004) 040, [hep-ph/0409146].

[81] S. Frixione, P. Nason, and C. Oleari, *Matching NLO QCD computations with Parton Shower simulations: the POWHEG method*, *JHEP* **0711** (2007) 070, [arXiv:0709.2092].

[82] S. Frixione and B. R. Webber, *Matching NLO QCD computations and parton shower simulations*, *JHEP* **0206** (2002) 029, [hep-ph/0204244].

[83] P. Nason and B. Webber, *Next-to-Leading-Order Event Generators*, arXiv:1202.1251.

[84] http://powhegbox.mib.infn.it/.

[85] **ATLAS Collaboration** Collaboration, G. Aad *et. al.*, *Measurement of the WW cross section in sqrt(s) = 7 TeV pp collisions with the ATLAS detector and limits on anomalous gauge couplings*, *Phys.Lett.* **B712** (2012) 289–308, [arXiv:1203.6232].

[86] **ATLAS Collaboration** Collaboration, G. Aad *et. al.*, *Measurement of the WZ production cross section and limits on anomalous triple gauge couplings in proton-proton collisions at sqrt(s) = 7 TeV with the ATLAS detector*, *Phys.Lett.* **B709** (2012) 341–357, [arXiv:1111.5570].

[87] **ATLAS Collaboration** Collaboration, G. Aad *et. al.*, *Measurement of the ZZ production cross section and limits on anomalous neutral triple gauge couplings in proton-proton collisions at sqrt(s) = 7 TeV with the ATLAS detector*, *Phys.Rev.Lett.* **108** (2012) 041804, [arXiv:1110.5016].

[88] **ATLAS Collaboration** Collaboration, G. Aad *et. al.*, *Measurement of W gamma and Z gamma production cross sections in pp collisions at sqrt(s) = 7 TeV and limits on anomalous triple gauge couplings with the ATLAS detector*, arXiv:1205.2531.

[89] H. Dreiner, S. Grab, M. Kramer, and M. Trenkel, *Supersymmetric NLO QCD corrections to resonant slepton production and signals at the Tevatron and the CERN LHC*, *Phys.Rev.* **D75** (2007) 035003, [hep-ph/0611195].

[90] J. Maalampi and N. Romanenko, *Single production of doubly charged Higgs bosons at hadron colliders*, *Phys.Lett.* **B532** (2002) 202–208, [hep-ph/0201196].

[91] T. Han, I. Lewis, and T. McElmurry, *QCD Corrections to Scalar Diquark Production at Hadron Colliders*, *JHEP* **1001** (2010) 123, [arXiv:0909.2666].

[92] **ATLAS Collaboration** Collaboration, G. Aad *et. al.*, *Search for gluinos in events with two same-sign leptons, jets and missing transverse momentum with the ATLAS detector in pp collisions at sqrt(s) = 7 TeV*, *Phys.Rev.Lett.* **108** (2012) 241802, [arXiv:1203.5763].

[93] **CMS Collaboration** Collaboration, S. Chatrchyan *et. al.*, *Search for new physics with same-sign isolated dilepton events with jets and missing transverse energy*, *Phys.Rev.Lett.* **109** (2012) 071803, [arXiv:1205.6615].

[94] A. Kulesza and W. J. Stirling, *Like sign W boson production at the LHC as a probe of double parton scattering*, *Phys.Lett.* **B475** (2000) 168–175, [hep-ph/9912232].

[95] E. Maina, *Multiple Parton Interactions in Z+4j, W+- W+- + 0/2j and W+ W- + 2j production at the LHC*, *JHEP* **0909** (2009) 081, [arXiv:0909.1586].

[96] J. R. Gaunt, C.-H. Kom, A. Kulesza, and W. J. Stirling, *Same-sign W pair production as a probe of double parton scattering at the LHC*, *Eur.Phys.J.* **C69** (2010) 53–65, [arXiv:1003.3953].

[97] B. Jager, C. Oleari, and D. Zeppenfeld, *Next-to-leading order QCD corrections to W+ W+ jj and W- W- jj production via weak-boson fusion*, *Phys.Rev.* **D80** (2009) 034022, [arXiv:0907.0580].

[98] A. J. Barr, *Measuring slepton spin at the LHC*, *JHEP* **02** (2006) 042, [hep-ph/0511115].

[99] A. J. Barr and C. G. Lester, *A Review of the Mass Measurement Techniques proposed for the Large Hadron Collider*, *J.Phys.G* **G37** (2010) 123001, [arXiv:1004.2732].

[100] P. Konar, K. Kong, K. T. Matchev, and M. Park, *Superpartner Mass Measurement Technique using 1D Orthogonal Decompositions of the Cambridge Transverse Mass Variable M_{T2}*, *Phys. Rev. Lett.* **105** (2010) 051802, [arXiv:0910.3679].

[101] C. Lester and D. Summers, *Measuring masses of semiinvisibly decaying particles pair produced at hadron colliders*, *Phys.Lett.* **B463** (1999) 99–103, [hep-ph/9906349].

[102] A. Barr, C. Lester, and P. Stephens, *m(T2): The Truth behind the glamour*, *J.Phys.G* **G29** (2003) 2343–2363, [hep-ph/0304226].

[103] W. S. Cho, K. Choi, Y. G. Kim, and C. B. Park, *Gluino Stransverse Mass*, *Phys.Rev.Lett.* **100** (2008) 171801, [arXiv:0709.0288].

[104] A. Datta, G. L. Kane, and M. Toharia, *Is it SUSY?*, hep-ph/0510204.

[105] W. S. Cho, K. Choi, Y. G. Kim, and C. B. Park, *M(T2)-assisted on-shell reconstruction of missing momenta and its application to spin measurement at the LHC*, *Phys.Rev.* **D79** (2009) 031701, [arXiv:0810.4853].

[106] H.-C. Cheng, Z. Han, I.-W. Kim, and L.-T. Wang, *Missing Momentum Reconstruction and Spin Measurements at Hadron Colliders*, *JHEP* **1011** (2010) 122, [arXiv:1008.0405].

[107] D. Horton, *Reconstructing events with missing transverse momentum at the LHC and its application to spin measurement*, arXiv:1006.0148.

[108] C.-Y. Chen and A. Freitas, *General analysis of signals with two leptons and missing energy at the Large Hadron Collider*, *JHEP* **1102** (2011) 002, [arXiv:1011.5276].

[109] G. Moortgat-Pick, K. Rolbiecki, and J. Tattersall, *Early spin determination at the LHC?*, *Phys.Lett.* **B699** (2011) 158–163, [arXiv:1102.0293].

[110] M. R. Buckley, S. Y. Choi, K. Mawatari, and H. Murayama, *Determining Spin through Quantum Azimuthal-Angle Correlations*, *Phys.Lett.* **B672** (2009) 275–279, [arXiv:0811.3030].

[111] M. Battaglia, A. Datta, A. De Roeck, K. Kong, and K. T. Matchev, *Contrasting supersymmetry and universal extra dimensions at the clic multi-TeV e+ e- collider*, *JHEP* **0507** (2005) 033, [hep-ph/0502041].

[112] A. J. Barr, G. G. Ross, and M. Serna, *The Precision Determination of Invisible-Particle Masses at the LHC*, *Phys.Rev.* **D78** (2008) 056006, [arXiv:0806.3224].

[113] C. G. Lester, M. A. Parker, and . White, Martin J., *Determining SUSY model parameters and masses at the LHC using cross-sections, kinematic edges and other observables*, *JHEP* **0601** (2006) 080, [hep-ph/0508143].

[114] S. Kullback and R. A. Leibler, *On information and sufficiency*, *Annals of Mathematical Statistics* **22(1)** (1951) 79–86.